MICROCOPY RESOLUTION TEST CHART

NATIONAL BUREAU OF STANDARDS - 1963 - A

CSL COORDINATED SCIENCE LABORATORY

AD-A142 408

THEORETICAL STUDIES OF HIGH FIELD, HIGH ENERGY TRANSPORT IN GALLIUM ARSENIDE, SILICON AND HETEROSTRUCTURES

REPORT DOCUMENTATION PAGE	READ INSTRUCTIONS BEFORE COMPLETING FORM

1. REPORT NUMBER	2. GOVT ACCESSION NO.	3. RECIPIENT'S CATALOG NUMBER
	AD-A142408	

4. TITLE (and Subtitle)	5. TYPE OF REPORT & PERIOD COVERED
THEORETICAL STUDIES OF HIGH FIELD, HIGH ENERGY TRANSPORT IN GALLIUM ARSENIDE, SILICON AND HETEROSTRUCTURES	
	R-987; UILU-ENG 83-2208
	6. PERFORMING ORG. REPORT NUMBER

7. AUTHOR(s)	8. CONTRACT OR GRANT NUMBER(s)
JEFFREY YUH-FONG TANG	DAAG 29-80-K-0069 N00014-76-C-0806

9. PERFORMING ORGANIZATION NAME AND ADDRESS	10. PROGRAM ELEMENT, PROJECT, TASK AREA & WORK UNIT NUMBERS
University of Illinois at Urbana-Champaign Coordinated Science Laboratory 1101 W. Springfield Ave. Urbana, IL 61801	

11. CONTROLLING OFFICE NAME AND ADDRESS	12. REPORT DATE
	January 1983
	13. NUMBER OF PAGES
	163

14. MONITORING AGENCY NAME & ADDRESS(if different from Controlling Office)	15. SECURITY CLASS. (of this report)
	Unclassified
	15a. DECLASSIFICATION/DOWNGRADING SCHEDULE

16. DISTRIBUTION STATEMENT (of this Report)

Distribution unlimited.

17. DISTRIBUTION STATEMENT (of the abstract entered in Block 20, if different from Report)

18. SUPPLEMENTARY NOTES

19. KEY WORDS (Continue on reverse side if necessary and identify by block number)

Gallium Arsenide   High Field
Silicon   High Energy Transport
Heterostructures

20. ABSTRACT (Continue on reverse side if necessary and identify by block number)

The study of high field transport has been instrumental to the theory of many semiconductor devices based on, e.g., the Hilsum-Ridley-Watkins mechanism, impact ionization phenomena, and recently real space transfer. A Monte Carlo simulation, including a pseudopotential band structure, is chosen for this study. It is shown in this study that this method can be applied to both the steady state and the transient state transport problems.

DD FORM 1473
1 JAN 73

THEORETICAL STUDIES OF
HIGH FIELD, HIGH ENERGY TRANSPORT
IN GALLIUM ARSENIDE, SILICON AND HETEROSTRUCTURES

BY

JEFFREY YUH-FONG TANG

B.S., National Taiwan University, 1977
M.S., University of Illinois, 1981

THESIS

Submitted in partial fulfillment of the requirements
for the degree of Doctor of Philosophy in Electrical Engineering
in the Graduate College of the
University of Illinois at Urbana-Champaign, 1983

Urbana, Illinois
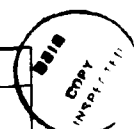
THEORETICAL STUDIES OF
HIGH FIELD, HIGH ENERGY TRANSPORT
IN GALLIUM ARSENIDE, SILICON AND HETEROSTRUCTURES

Jeffrey Yuh-Fong Tang, Ph.D.
Department of Electrical Engineering
University of Illinois at Urbana-Champaign, 1983

The study of high field transport has been instrumental to the theory of many semiconductor devices based on, e.g., the Hilsum-Ridley-Watkins mechanism, impact ionization phenomena, and recently real space transfer. It will become even more important as device sizes approach submicron dimensions. Current interest in small devices concerns not only scaling down and VLSI (very large scale integration) but also phenomena such as size quantization, real space transfer, and velocity overshoot, which was recently termed ballistic transport.

A Monte Carlo simulation, including a pseudopotential band structure, is chosen for this study. It is shown in this study that this method can be applied to both the steady state and the transient state transport problems.

The speed enhancement of injecting electrons over the $Al_xGa_{1-x}As$-GaAs hetero-barrier is studied. The results show that a narrow "collision free window" exists with respect to parameters such as the electric field, the injection energy, the external voltage, and the semiconductor dimension. It is found that only emitter(source)- and base-like structures are eligible for collision-free transport; collectors(drains) are not because of unavoidable high voltage drops.

The emission of hot electrons from the silicon substrate to the silicon dioxide is studied. By a detailed investigation of the steady state transport phenomena in silicon, three sets of transport parameters are found. A Monte Carlo simulation which includes two realistic con-

duction bands and the spatial variation of the electric field is then performed to study the high energy tail of the distribution function.

Recently, the validity of the semiclassical Boltzmann transport equation has been reexamined and quantum corrections for the transport equation have been suggested. The quantum aspects of the transport problem are discussed. A quantum Monte Carlo method is proposed and various quantum effects are examined. The study indicates that the most important quantum correction is the self-energy effect which amounts to a quasi-particle Boltzmann transport equation. The intra-collisional field effect is shown not to be important in a steady state situation.

TABLE OF CONTENTS

CHAPTER 1

INTRODUCTION

The study of high field transport has been instrumental to the
theory of many semiconductor devices based on, e.g., the Hilsum-Ridley-
Watkins mechanism, impact ionization phenomena, and recently real space
transfer [1,2]. It will become even more important as device sizes
approach submicron dimensions. For example, electron devices with
lengths of 0.1-1 μm and supply voltages of 1 volt will operate at elec-
tric fields of 10-100 kV/cm and corresponding equivalent electron temper-
atures [3] of about 5000 K. Besides drift, hot electron diffusion and
related noise phenomena will be important under such conditions. Cur-
rent interest in small devices concerns not only scaling down and VLSI
(very large scale integration) but also phenomena such as size quantiza-
tion, real space transfer, and velocity overshoot, which was recently
termed ballistic transport.

This thesis addresses real space transfer, the emission of hot
electrons over heterojunction barriers as defined by Hess [3], in a
generalized sense. In the past, real space transfer was mainly considered
in connection with the proposed real space transfer oscillator [1]. Here
it will be shown that the effect of hot electrons crossing heterointer-
faces has many applications in the theory of semiconductor devices. The
following effects are related to the above concept:

(1)   the emission of hot electrons from silicon into silicon dioxide

(2)   the enhancement of impact ionization for hot electrons crossing

      heterointerfaces [4]

(3)   injection of electrons over a hetero-barrier to achieve high

      speed enhancements and

(4)   effects such as real space transfer noise and hot electron emis-

      sion out of buried channels [5].

The emission of hot electrons from the silicon substrate into the

silicon dioxide [6] has been known for some while and is based on the

same physical concept as real space transfer. Because of device re-

liability questions, this latter problem has received much attention in

the past. The emission of electrons into SiO_2 is, of course, detrimental

to device performance. Thus, real space transfer can be used to con-

struct devices but also appears as a "nuisance" in device operation.

The same is, of course, true for impact ionization.

Impact ionization phenomena are, on the one hand, a limiting factor

in the reduction of the device size, but on the other hand represent an

essential mechanism in the operation of semiconductor devices such as

avalanche photodiodes. Of special interest to us is the ratio of the

electron (α) and hole (β) ionization rates. To minimize the noise [7,8],

a large α/β (or β/α) ratio is highly desirable. Unfortunately, most III-V

semiconductors, including alloys for long wavelength detectors, exhibit

values of α nearly equal to that of β. In order to create an artificially

large α/β (or β/α) ratio, use can be made of the difference in the band-

edge discontinuities for electrons and holes in a multilayered

heterostructure. This is really a concept of high energy injection of the carriers inherent to a heterojunction structure. This enhancement effect was first predicted by theoretical considerations [4] and then verified experimentally [9].

This large variety of effects could not be covered within one thesis if they could not all be understood and quantitatively calculated by the same approach: <u>A Monte Carlo simulation inclu g a pseudopotential band structure</u>. The Monte Carlo simulation, b d on the semiclassical Boltzmann transport equation, has been chosen .ᛉ .his study. In Chapter 2, we discuss the Monte Carlo methods for the steady state and the transient state simulation. In Chapter 3, we report the results of transport studies of GaAs and related heterostructures. In Chapter 4, the band-structure dependent high field transport results for silicon are discussed.

In Chapter 5, the emission of electrons into the SiO_2 from a silicon substrate is studied. In this study, the high energy tail of the hot electron distribution function is examined. A better set of high field transport parameters is obtained in this study, which is a big step forward toward a better understanding of high field transport in semiconductors.

Recently, the validity of the semiclassical Boltzmann transport equation has been reexamined and quantum corrections for the transport equation have been suggested [10,11]. In Chapter 6, we discuss the quantum aspects of the transport problem. A quantum Monte Carlo method is proposed and various quantum effects are examined.

CHAPTER 2

MONTE CARLO SIMULATION

2.1 Introduction

The theoretical basis of high field transport studies has been
mainly the semiclassical Boltzmann transport equation. Depending on
the nature of the transport problem, different numerical approaches
have been developed in solving this complicated nonlinear integro-
differential equation. Among the many approaches, a Monte Carlo simu-
lation has been the most successful. It easily includes all the scat-
tering mechanisms, allows the inclusion of more than one realistic
energy band [12,13], can study both transient and steady state phenomena,
and has the power to extend beyond the basis of the classical Boltzmann
transport equation to include quantum corrections such as self-energy
corrections, collision broadening and the intracollisional field effect.
Due to these advantages, the Monte Carlo method was chosen for this
thesis study. This chapter is devoted to the discussion of the Monte
Carlo method. As for the validity of the semiclassical transport equa-
tion, detailed discussions can be found in Chapter 6.

The Monte Carlo method is a method of computer simulation of a phy-
sical system. It gets its name from the use of random numbers to simu-
late statistical processes in order to numerically generate the underlying
probability distribution of a system. The application of simulation
techniques in theoretical physics and engineering serve two main purposes:

To bypass the mathematical difficulties in solving complicated system governing equations and to attain deeper insight into the microscopic physical mechanisms that the governing equations describe. This method has found wide application in the field of statistical physics [14] and was first introduced to the field of semiconductor transport by Kurosawa [15] in 1966. The pioneering work of Fawcett, Boardman and Swain in 1970 [16], which successfully reproduced the Gunn effect in GaAs in their Monte Carlo simulation, was encouraging, although some details of the band structure were still unknown to them. Many advances have been made in the work of Monte Carlo simulation since then, for example, by the Italian group [17-20], the French group [21-23], etc. The most recent advance of the Monte Carlo method has been developed by Schichijo and Hess who included a realistic band structure [12].

In Section 2.2, we discuss the basic scheme of the Monte Carlo simulation. In Sections 2.3 and 2.4, the steady state Monte Carlo method and the transient ensemble Monte Carlo method are discussed respectively.

2.2 Basic Monte Carlo Scheme

There are two main ingredients in a Monte Carlo simulation, the band structure and the scattering rates. The standard Monte Carlo method that has been used by most researchers incorporates in it an analytic band structure, i.e., a parabolic $E(\vec{k})$ relation including at most a nonparabolicity factor which accounts partly for the nonparabolic nature of the band structure, and scattering rates which are calculated by the Golden rule, the effective mass and the Born approximation [24]. It was Shichijo and Hess [25] who first included the realistic band structure calculated

by the empirical pseudopotential method in the Monte Carlo simulation. Based on their pioneering work, I have refined and improved the method to include two conduction bands.

As for the scattering rates, we follow the conventional approach but modify the effective mass density of states to behave like the true density of states in high energies. One important point to make is that although scattering rates are calculated by the conventional method to fit to the experimental results, the incorrect nature of the Golden rule, i.e., the energy conservation δ-function, in the strong scattering regime, is improved in the simulation by always selecting the scattering final states in a possible energy range which smears out the sharp δ-function structure. We discuss in Chapter 6 the quantum transport in semiconductors and a field theoretic approach to calculate the high energy scattering rates.

The basic Monte Carlo scheme is shown in Figure 2.1. An electron is started in a state $\vec{k}_a(i)$ whose energy is calculated via the band structure subroutine. Through the energy dependent scattering rates, the free flight time $T(i)$ of the electron is determined by solving

$$r = \exp\left[-\int_0^{T(i)} \frac{dt}{\tau(E(\vec{k}(t)))} \right] \tag{2.1}$$

where r is a random number uniformly distributed between 0 and 1. The details of how the free flight time should be determined are discussed in Appendix 1. From the equation of motion of a Bloch state under an
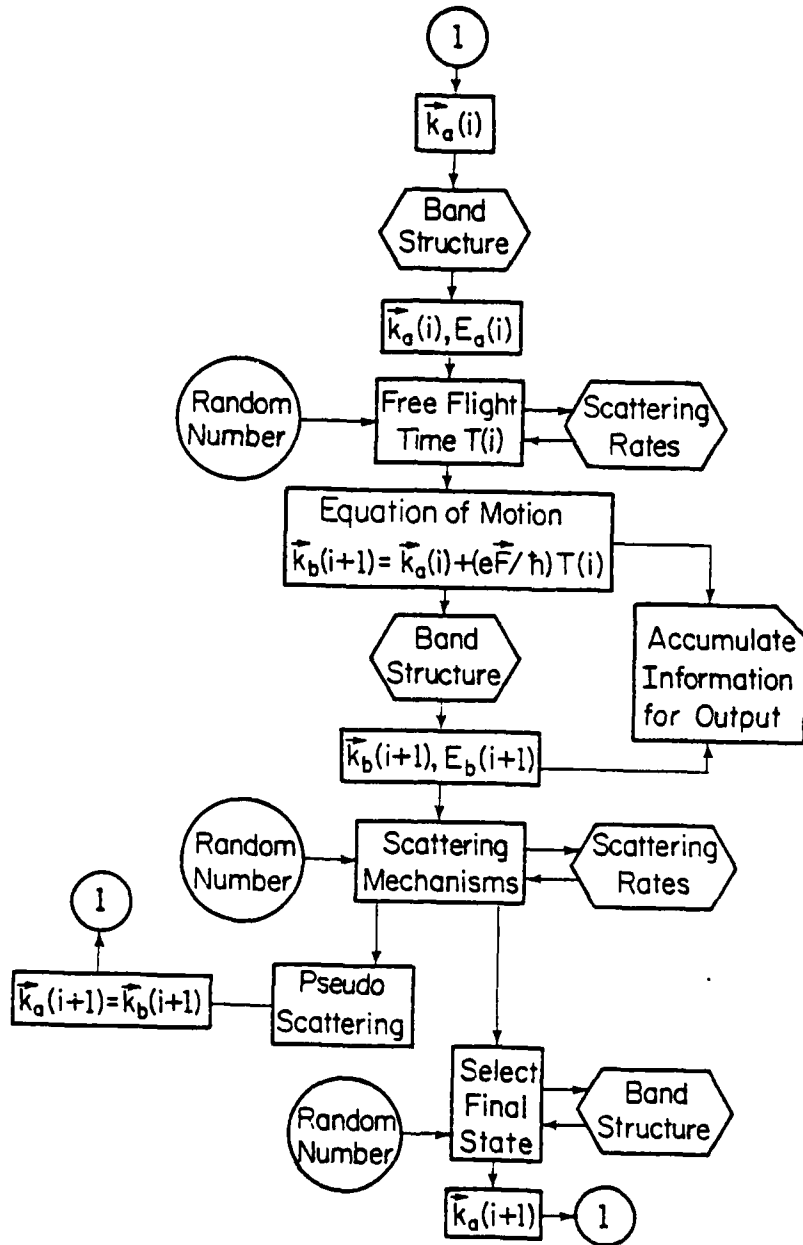
Figure 2.1: Flow chart of a Monte Carlo simulation.

applied external field, the final state of the free flight is calculated as

$$\vec{k}_b(i+1) = \vec{k}_a(i) + \frac{e\vec{F}}{\hbar} T(i). \tag{2.2}$$

Again from the band structure, the energy of the state $\vec{k}_b(i+1)$ is obtained. A random number is then generated to determine what scattering is to take place. If it were a pseudo scattering, the electron starts with $\vec{k}_a(i+1) = \vec{k}_b(i+1)$ again from the beginning of the loop. If it were not a pseudo scattering, a final state according to the nature of the particular scattering mechanism is determined through random numbers and, of course, the band structure. Starting with this selected new state, the electron enters the beginning of the loop. This is the basic procedure of the Monte Carlo simulation.

The essential idea of the simulation described above is to follow the trajectory of the electron according to the electronic band structure and the scattering mechanisms, and accumulate in its paths the relevant information of physical quantities like the drift velocity, the average energy, the scattering mean free path, the scattering mean free time, the distribution function, etc. It has been proven that the distribution function obtained from the Monte Carlo simulation solves the Boltzmann equation [16,20] over a long simulation path. The criteria which ensure that the observables obtained from the simulation converge to the true values after a "long" simulation path (or time) are essential to the Monte Carlo simulation and are discussed in Section 2.3 and Section 2.4 for the steady state and the transient state cases respectively.

2.3 Steady State Monte Carlo

In the steady state simulation, the semiconductor is assumed to be homogeneous, infinitely large and under a uniform applied field such that the real space structure of the material is of no concern. The trajectory of the electron is traced in momentum space only and a distribution function $f(\vec{k})$ depending only on the crystal momenta is obtained. For device lengths greater than several microns and a moderate spatial variation of the electric field in the device, the steady state Monte Carlo simulation can be applied.

In principle, all observables of interest can be calculated once $f(\vec{k})$, the distribution function, is obtained. But because of numerical problems, it is very costly to calculate the distribution function to a satisfactory degree of accuracy such that all relevant quantities can be obtained through easy numerical integration or differentiation of the distribution function. To bypass such numerical difficulties, estimators are devised to accumulate relevant information of various relevant observables [26,27].

The field dependence of the drift velocity of a semiconductor is the most important information for the design of a semiconductor device. The velocity estimator is also one of the most important concerns in a steady state Monte Carlo simulation. By properly choosing a complementary pair of velocity estimators, the reach of the steady state condition and the convergence of the estimators can be easily tested. The two kinds of velocity estimators described below are based respectively on (1) the energy gained from the external field during free flights and (2) the energy lost through phonon emission during the scatterings.

The first velocity estimator has been used by many authors and is given as

$$v_j = \frac{1}{K_j} \sum \int_{k_{zi}}^{k_{zf}} \frac{1}{\hbar} \frac{\partial E}{\partial k_z} dk_z = \frac{1}{\hbar K_j} \sum (E_f - E_i), \tag{2.3}$$

where the subscript j refers to the jth valley, k_{zi} and k_{zf} are the initial and final states in the field direction, z, of the free flight, K_j is the total length of the $\vec{k}$-space trajectory and the summation is over all the free flights. K_j, the $\vec{k}$-space trajectory, is simply related to the total free flight time T_j in the valley by

$$K_j = \frac{eF}{\hbar} T_j, \tag{2.4}$$

according to the equation of motion. Thus Equation 2.3 simplifies to

$$v_j = \frac{\sum (E_f - E_i)}{eFT_j} = \frac{\sum \Delta x}{T_j}, \tag{2.5}$$

where Δx is the distance traveled in real space during the free flight and is related directly to the energy gained from the field as

$$E_f - E_i = \Delta E = eF\Delta x. \tag{2.6}$$

So the first drift velocity estimator is based on the energy gained from the field during the free flight, which is directly related to the free flight length in real space.

The second velocity estimator is based on the idea of power balance in a steady state condition, i.e., the power input has to balance the power output. The power balance equation for one electron is given as

$$< - \frac{\partial E}{\partial t} > = e\vec{F} \cdot \vec{v} \, , \qquad (2.7)$$

where the quantity on the left hand side is the energy dissipation rate due to the phonon scattering events. This energy dissipation rate can be directly accumulated in the Monte Carlo simulation and hence the drift velocity can be calculated as

$$v_d = \frac{< - \frac{\partial E}{\partial t} >}{eF} \, . \qquad (2.8)$$

The second velocity estimator, which was developed in this work, is complementary to the first drift velocity estimator and has served as the best convergence test for the steady state Monte Carlo simulation for our purposes.

Depending on the interests in the transport problems, estimators for different observables can be set up according to their physical meanings. For example, the energy relaxation time can be obtained as

$$\tau_E(<E>) = \frac{<E> - \frac{3}{2} kT}{< - \frac{\partial E}{\partial t} >} \, , \qquad (2.9)$$

where $<E>$ is the average energy of the electron and is of course a function of the electric field. The carrier temperature can be defined and then obtained as

$$T_c = \frac{<E>}{\frac{3}{2} k} \, . \qquad (2.10)$$

The word "defined" means that the electron temperature might not imply a Maxwellian distribution.

One last important high field quantity of interest to be discussed is the impact ionization coefficient. This estimator is given as

$$\alpha \equiv \frac{n_{imp}}{d} , \tag{2.11}$$

where α is the ionization coefficient defined as the reciprocal of the average distance during which an impact ionization event occurs, n_{imp} is the total number of impact ionization events and d is the total distance traveled by the carrier in the field direction during the simulation. In a steady state condition, d, the total distance in the field direction can also be expressed as

$$d = <l_f> n_{sc}, \tag{2.12}$$

where $<l_f>$ is the mean free path in the field direction between scatterings and n_{sc} is the total number of scatterings. A simple substitution for d in α gives

$$\alpha = \frac{n_{imp}}{<l_f> n_{sc}} , \tag{2.13}$$

and hence

$$n_{imp} = \alpha <l_f> n_{sc} . \tag{2.14}$$

Since $<l_f>$ can be accurately obtained for a few hundred scatterings in the simulation, a better way to obtain α is to plot the number of impact ionization events as a function of the number of phonon scattering events and get from the slope of the curve the impact ionization coefficient α. The standard deviation can also be estimated from the plot.

2.4 Transient Ensemble Monte Carlo

As technology advances, device sizes are getting smaller. FETs with gate lengths less than 1000 Å are being made and peculiar hot electron effects have been observed [28]. The conventional current equations and continuity equation no longer serve the purpose in solving the transport problem of such small devices. One expects that transient transport behavior like the velocity overshoot phenomenon [29] emerges in such small devices. To approach the submicron transport problems with a Monte Carlo technique, one sees immediately that the real space structure, namely the geometry of the device, is of importance. It is just like solving differential equations: initial conditions and boundary conditions play the most important role. What we like to discuss in this section is not the initial or boundary conditions for the specific problems, but the general Monte Carlo techniques for solving the transient transport problems once the initial and boundary conditions are specified.

In the uniform spatial field case, the basic Monte Carlo scheme for the transient simulation is essentially the same as that described in Section 2.2 except that one also has to trace the trajectory of the carrier in real space. The electrons are released one by one from the source (cathode) and their trajectories are stored in histograms respectively. The distribution of quantities of interest in real space can be obtained by averaging the ensemble histograms of the carriers. The mesh sizes in real space are of the order of 100 Å depending on the observables of interest. The problem with too small a mesh size is that the convergences of some observables are hard to achieve. Let us cite

an analogy to explain why this is so. If one has the grades of a hundred students and one wants to plot the distribution of the grades (say from 0 to 100), a similar problem occurs if one chooses too small an interval (say 2).

In testing the convergence of the estimators, the best way to our knowledge is to plot the ensemble average of the estimators as a function of the number of ensemble carriers and observe the convergence from the curve. Depending on the observables of interest, the convergence curves can be very different. For example, it takes about 500 electrons to get a reasonable convergence of the ensemble average of the velocity estimator, but it takes more than a thousand electrons to get a good estimate of the satellite valley populations in GaAs under fast transient response conditions.

In the nonuniform spatial field condition, the transient Monte Carlo method needs to be modified. The general form of the equations of motion for a one dimensional real space is as follows:

$$\Delta \vec{k} = \frac{e}{\hbar} \int_{t_0}^{t_1} \vec{F}(t) dt \tag{2.15}$$

and

$$\Delta E = e \int_{x_0}^{x_1} F(x) dx, \tag{2.16}$$

where $\Delta \vec{k}$ is the momentum gained in the free flight time from t_0 to t_1, and ΔE is the energy gain during the acceleration. We see that Equation 2.15 is our big problem in that the field at time $t_0 < t < t_1$ depends on

the position $x(t)$, the velocity $v(x(t))$ and hence the band structure $E(\vec{k})$ in a complicated way. But if $\Delta t = t_1 - t_0$ is short enough, which is the case in one special way of Monte Carlo simulation (as described in Appendix 1), we can proceed as follows. Mathematically, Equations 2.15 and 2.16 can be written as

$$\frac{e}{\hbar} \int_{t_0}^{t_1} \vec{F}(t) dt = \frac{e}{\hbar} \vec{F}_m \Delta t = \frac{e}{\hbar} \vec{F}(x_0) \left(\frac{F_m}{F(x_0)} \Delta t \right) = \frac{e}{\hbar} \vec{F}(x_0) \Delta t' \qquad (2.17)$$

and

$$e \int_{x_0}^{x_1} F(x) dx = e[\phi(x_0) - \phi(x_1)] \simeq e F_m \Delta x = E(\vec{k}_1) - E(\vec{k}_o) , \qquad (2.18)$$

where F_m is some unknown mean field strength, the last equality in Equation 2.17 defines $\Delta t'$, $\phi(x)$ is the potential profile, and the relation established by the "almost equal to" sign is under the assumption of a small Δt. To understand the situation better, let us examine what the unknowns and the knowns are in Equations 2.17 and 2.18. The carrier is now located at the "point" specified by $(t_0, \vec{k}_0, x_0)$, and is about to drift to the point $(t_1, \vec{k}_1, x_1)$ in the interval $\Delta t = t_1 - t_0$. All quantities related to the initial point are known but none related to the final point. In light of the last equality in Equation 2.17, one sees that the result of a carrier drifting in a time interval $\Delta t'$ under a uniform electric field $\vec{F}(x_0)$ is the same as the result of a carrier drifting in a time interval Δt under nonuniform fields provided that $\Delta t'$ is related to Δt as

$$\Delta t = \frac{F(x_0)}{F_m} \Delta t' \quad . \tag{2.19}$$

F_m, which is not a quantity directly related to the initial point,

must be known. We see that if we manipulate Equations 2.17 and 2.18,

F_m can be obtained as

$$F_m = \frac{\Delta E}{e \Delta x} \quad , \tag{2.20}$$

where

$$\Delta E = E(\vec{k}_0 + \frac{e}{\hbar} \vec{F}(x_0)\Delta t') - E(\vec{k}_0) \tag{2.21}$$

and

$$\Delta x = \phi^{-1}\left[\frac{\Delta E}{e} - \phi(x_0)\right] - x_0 \quad . \tag{2.22}$$

The primary difficulty is that $\Delta t'$ must be known to solve for F_m.

As described in Appendix 1, Δt is chosen to be about 1/10 of

the scattering time $\tau(E(\vec{k}_0))$. As long as the choice of $\Delta t'$ does not

result in a Δt not satisfying the usual requirement (about 1/10 of

the scattering time), we can proceed in the simulation to scatter

the carrier if the generated random number r is such that

$$r \leq \frac{\Delta t}{\tau(E(\vec{k}_1))} \quad . \tag{2.23}$$

The reader is referred to Appendix 1 for details. In the simulation

procedure, the extra step added to account for the nonuniform field

effect is simply to "renormalize" the drift time Δt according to Equation 2.19 before determining the occurrences of the scattering events. For a small spatial variation of the electric field, i.e., the gradient of the field is small, Δt is not very different from $\Delta t'$. But for a large spatial variation of the electric field, one has to go through this process.

What has been described was a single carrier ensemble Monte Carlo technique. There might be cases that multicarrier simulation is necessary and the inclusion of the electron-electron scattering is of importance. In principle, these can all be carried out provided that enough money is invested. It seems that the only limitations of the Monte Carlo technique in this respect are just the memory and the speed of the computer.

In Chapter 6, we will discuss the methods of extending the standard classical Monte Carlo technique to include the quantum effects.

CHAPTER 3

TRANSIENT TRANSPORT IN GaAs FOLLOWING HIGH ENERGY INJECTION

3.1 Introduction

Since the first calculation of transient electron transport in short channel FETs by Ruch [29], overshoot phenomena of the electron velocity on very short time and length scales have attracted considerable attention [39-33]. Shur [31] and Shur and Eastman [32] added features of space charge limited conditions to the velocity overshoot. They investigated the initial transient and called it the "near ballistic" regime. The term "ballistic" is difficult to define and is currently applied to a wide range of device parameters and dimensions. Investigations in References 31 and 33 indicate that "near ballistic" transport over larger distances (> 1000 Å), if achievable, necessitates injection of electrons at higher energy. High energy injection was also discussed by Hess [34] for low temperature transport free of scattering events over extremely large distances $L > 10^{-4}$ cm (for electron energies below 0.036 eV).

The criteria for designing devices and choosing materials such that high transient speeds can be advantageously achieved using high energy injection are the key issues of this study. We approach the problem using a transient ensemble Monte Carlo simulation as discussed in Chapter 2, which includes the details of the band structure as calculated by the empirical pseudopotential method. The electron is started at higher

energy values (not at the bottom of the band as done by Ruch) to simulate

injection over a hetero-barrier. The electric field is chosen so as to

be constant over the whole distance of the simulation, in contrast to

the choice of the self-consistent field by Shur [31]. The reason for

this is the following: Within the "collision free window (CFW)", the

electron velocity does not vary strongly over the device length because

the electrons are already injected at high velocities (in contrast to the

cases considered by Shur). Therefore, the carrier concentration is

rather constant and the electric field induced by the carriers is of minor

importance. We do not include the intracollisional field effect [11,35]

because it would greatly complicate the computations. In the CFW, it

would make only minor contributions since the electric fields in this

window are small.

With respect to device applications, the result of the calculations

can be summarized as follows: On a length scale of 1000 $\overset{\circ}{A}$, emitter

(source)- and base-like structures may show effects typical for collision

free transport (if carefully designed); collector (drain)-like structures

will not.

3.2 Physical Model and Method of Computation

As discussed above, we consider high energy electrons injected into

GaAs (e.g., from $Al_xGa_{1-x}As$ or δ-like electric fields created by space

charge layers). The transition is assumed to be abrupt, i.e., the elec-

tron gains kinetic energy ΔE and forward momentum Δk when transferring

to the GaAs without any energy loss.

As illustrated below, the calculation of the self-consistent field resulting from external voltages and an electron redistribution in the GaAs is a difficult problem and depends on many details, most importantly:

(1) the boundary conditions of the injection,

(2) the statistics of electrons and impurities in the GaAs,

(3) the level of injection,

(4) the velocity distribution and the injection energy.

Let us assume that our device is short in the x-direction but rather wide in the y-direction. We then can still define average quantities such as the density of electrons in a meaningful way and use a continuum picture as follows: If the distribution function is denoted by f, we define the electron density

$$n(x) = \frac{2}{(2\pi)^3 L} \int_0^L dy \int_{-\infty}^{\infty} d\vec{k} \ f \tag{3.1}$$

or the current density as

$$j = \frac{e}{L} \int_0^L dy \int_{-\infty}^{\infty} d\vec{k} \ \vec{v}_k \ f \tag{3.2}$$

and use the current- and the continuity-equation as usual. The calculation of the self-consistent field, however, does not proceed as simply because the statistics of electrons and impurities (donors, acceptors) and their time dependent motion, play a role in the solution of the Poisson equation. As a consequence, we can only obtain the average electric field

$$F(x) = \frac{1}{L} \int_0^L dy\, F(x,y) \tag{3.3}$$

in a straightforward manner. The field which enters the Monte Carlo calculations, however, (in a nonlinear way) is $F(x,y)$. The use of $F(x)$ is only appropriate under heavy injection conditions (i.e., large currents). The x-dependence of $F(x)$ is a function of the boundary conditions and the average electron velocity. It can be obtained for various limiting cases from:

$$-\frac{\partial F(x)}{\partial x} = \frac{e}{\varepsilon \varepsilon_o} \left(\frac{j}{e\mu F} - N_D \right) , \tag{3.4}$$

where N_D represents the fixed charge (doping). Thus for low injection and low doping density:

$$F(x) \simeq \frac{V}{d} , \tag{3.5}$$

where V is the applied voltage. For heavy injection and μ = const

$$F(x) \propto \sqrt{x} , \tag{3.6}$$

and for F = const

$$F(x) \propto x . \tag{3.7}$$

An analysis including the statistics of the electron and impurity distribution (which appears to be vital) is extremely difficult. Fortunately, the average electron velocity does not sensitively depend on this electric field if the electrons are injected at high energies and

if we restrict ourselves to the CFW, as will be seen from the numerical results. We therefore assumed in our computation the constant electric field of Equation 3.5. Outside the CFW and for high injection this approximation is weak and gives only an estimate of the approximate average velocity. The error can be estimated from Equations 3.5 to 3.7 and the field dependent results as given in the next section.

The Monte Carlo program used for the computations is a revised version of that described in the thesis work of Shichijo [25]. The scattering rates used in our Monte Carlo model are identical to those used by Littlejohn et al. [36] for energies below $\simeq$ 1 eV. For higher energies, we assume a proportionality to the density of states and, consequently, a decreasing scattering rate above 1.5 eV [25]. However, for most results, energies above 1 eV are not important. But even for this lower energy range (< 1 eV), the inclusion of a realistic band structure is important. We chose the band structure as calculated by the empirical pseudopotential method as described in [25,37]. The energy of the L-minima was fixed to 0.33 eV and the energy of the X-minima to 0.522 eV. We use $\sim$ 7000 mesh points of the $E(\vec{k})$ relation calculated by the empirical pseudopotential method and interpolate between these points. The bandstructure is not well simulated by this model at very low energies (few points only) and the results at low energies and low fields are therefore estimated to be in error by 20%. In the electric field range of interest here, the average electron energy approaches $\sim$ 1 eV, where the total scattering rate is about 10^{14} sec^{-1}. Our formalism, which is equivalent to the semiclassical Boltzmann formalism, is valid in this range of energies and scattering rates even if very strict criteria are applied.

To be specific, we assume that the electrons are injected from $Al_xGa_{1-x}As$ into GaAs. In this case, one needs to have a direct band gap in the $Al_xGa_{1-x}As$, i.e., x < 0.45, with most of the electrons residing in the Γ valley. The reason is that the electrons transmitted into the GaAs will most likely end up in the corresponding valleys in GaAs (because of conservation of crystal momentum) and the heavy masses of the satellite valleys in GaAs are undesirable for achieving high velocity. An indirect $Al_xGa_{1-x}As$ is thus undesirable to start with. Electrons starting at Γ in $Al_xGa_{1-x}As$ will have (with high probability) a wave vector $\vec{k}_0 = (k_x,0,0)$ in the GaAs where $E_{GaAs}(\vec{k}_0) = \Delta E_c$ and ΔE_c is the band edge discontinuity. This concludes our model assumptions. The numerical results are given below.

3.3 Results and Discussions

We present results for the average drift velocity, the energy distribution, the average number of scattering events, and the transit time of electrons as a function of several parameters.

To demonstrate the significant effect of the initial injection energy, the average drift velocity versus distance is plotted in Figures 3.1a and b for various injection energies. The increase of the injection energies is accompanied by a substantial increase of the average drift velocity of the electrons as long as the injection energy stays below the minima of the X and L valleys. Figure 3.1 clearly demonstrates that there exists a CFW with respect to the injection energy. Too high of an injection energy works against the speed of the device, as is seen from curve h in Figure 3.1a and curve e in Figure 3.1b. At low injection energies, on the other hand, high velocities are not achieved.
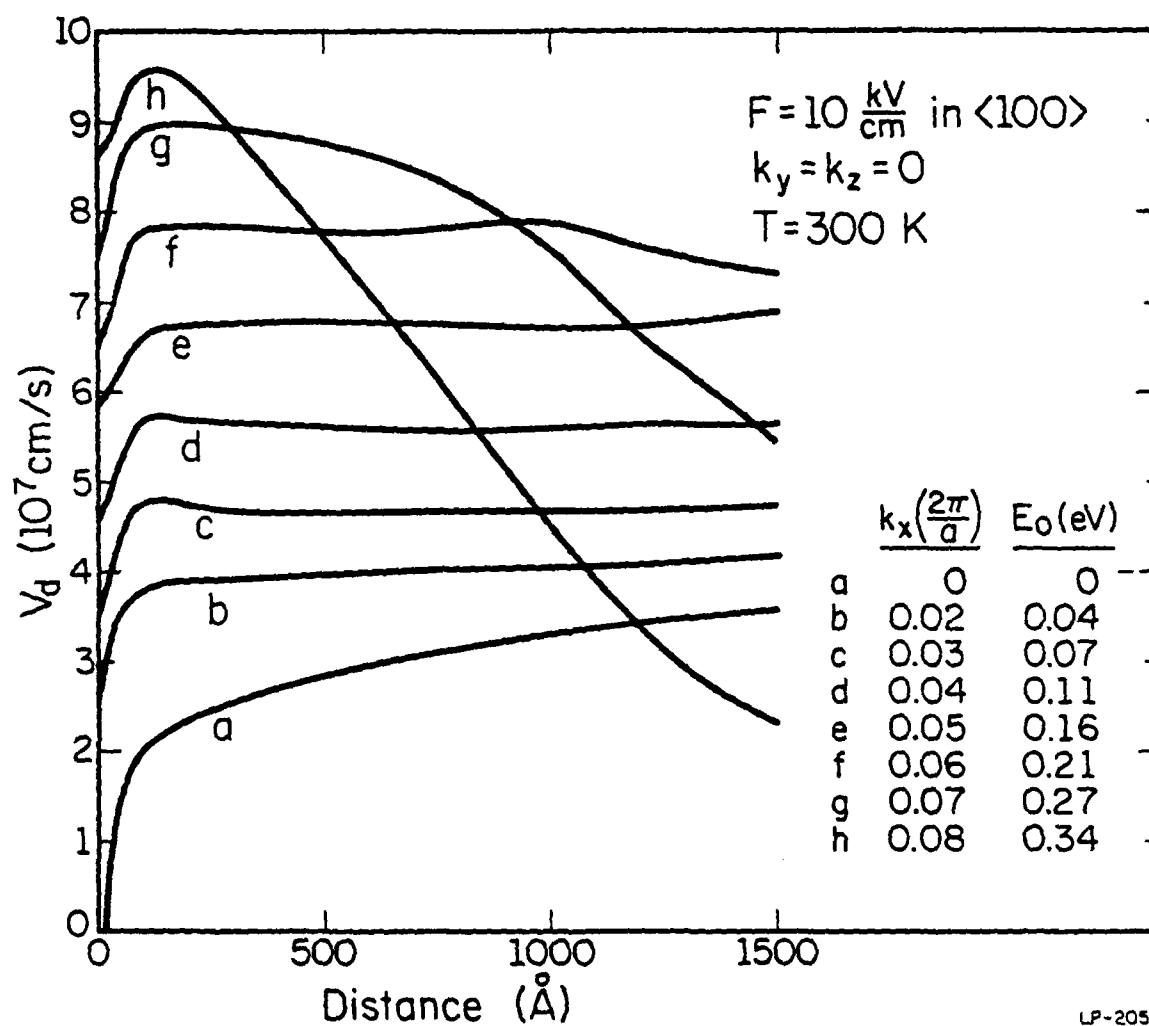
Figure 3.1(a): Average drift velocity versus the device length with
injection energy as a parameter at T = 300 K. The
electric field is applied in the <100> direction.
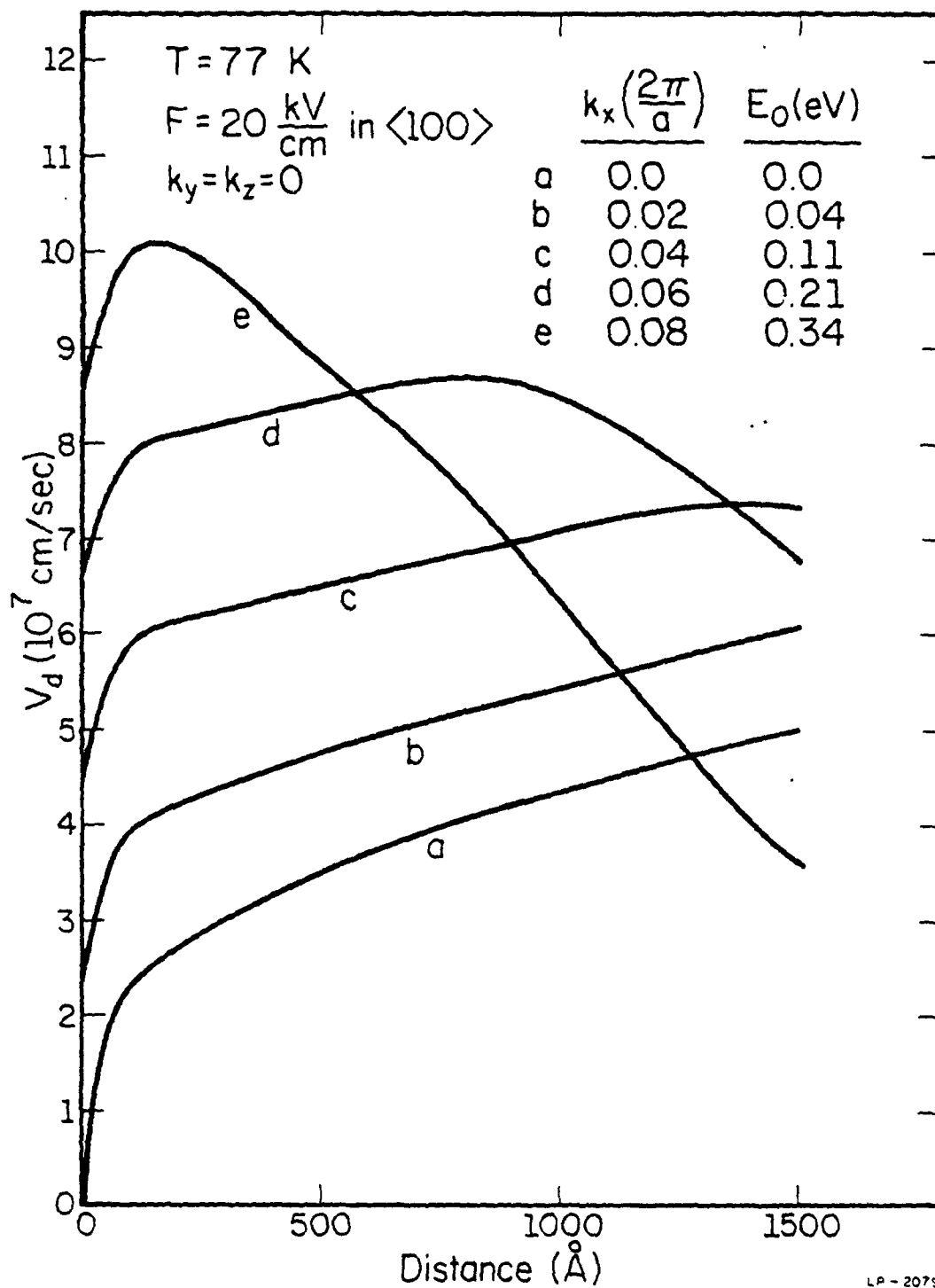
Figure 3.1(b): Average drift velocity versus the device length
with injection energy as a parameter at T = 77 K.
The electric field is applied in the <100>
direction.

Figures 3.2a and b show the dependence of the average drift velocity on the strength of the external electric field, again for 77 K and 300 K, with a fixed initial energy E_0 = 0.24 eV (i.e., k_x = 0.065 $2\pi/a$). By examining Figures 3.2a and b, we notice that the peak transient velocity increases with increasing electric field. However, the velocity decreases faster at higher electric fields as the length increases. For a device length of 1000 Å, operation in the CFW regime requires that the electric field does not exceed ~ 35 kV/cm, which means that the applied voltage must not exceed 0.35 V. This is the reason for our statement that ballistic transport does not seem to be feasible for collector (drain)-like structures but may be important for emitter (source)- and base-like device regions.

The physical explanation of these phenomena is simple. The electrons start with high velocities when injected into the central Γ valley (small effective masses) of GaAs and are accelerated by the electric field in the forward direction. Those electrons which survive the intervalley scattering processes move up in energy with little polar optical scattering and raise the ensemble average of the electron drift velocity. Note that the importance of polar optical scattering decreases with increasing energy. Since we investigated electron injection at high energies, our results differ from the situations investigated previously [34,38]. The electrons which are scattered to the L and X minima have a very low mobility and do not contribute much to the average velocity. Higher electric fields accelerate the electrons to the energy of the X and L minima and therefore reduce the velocity after some distance. In Figure 3.3, the
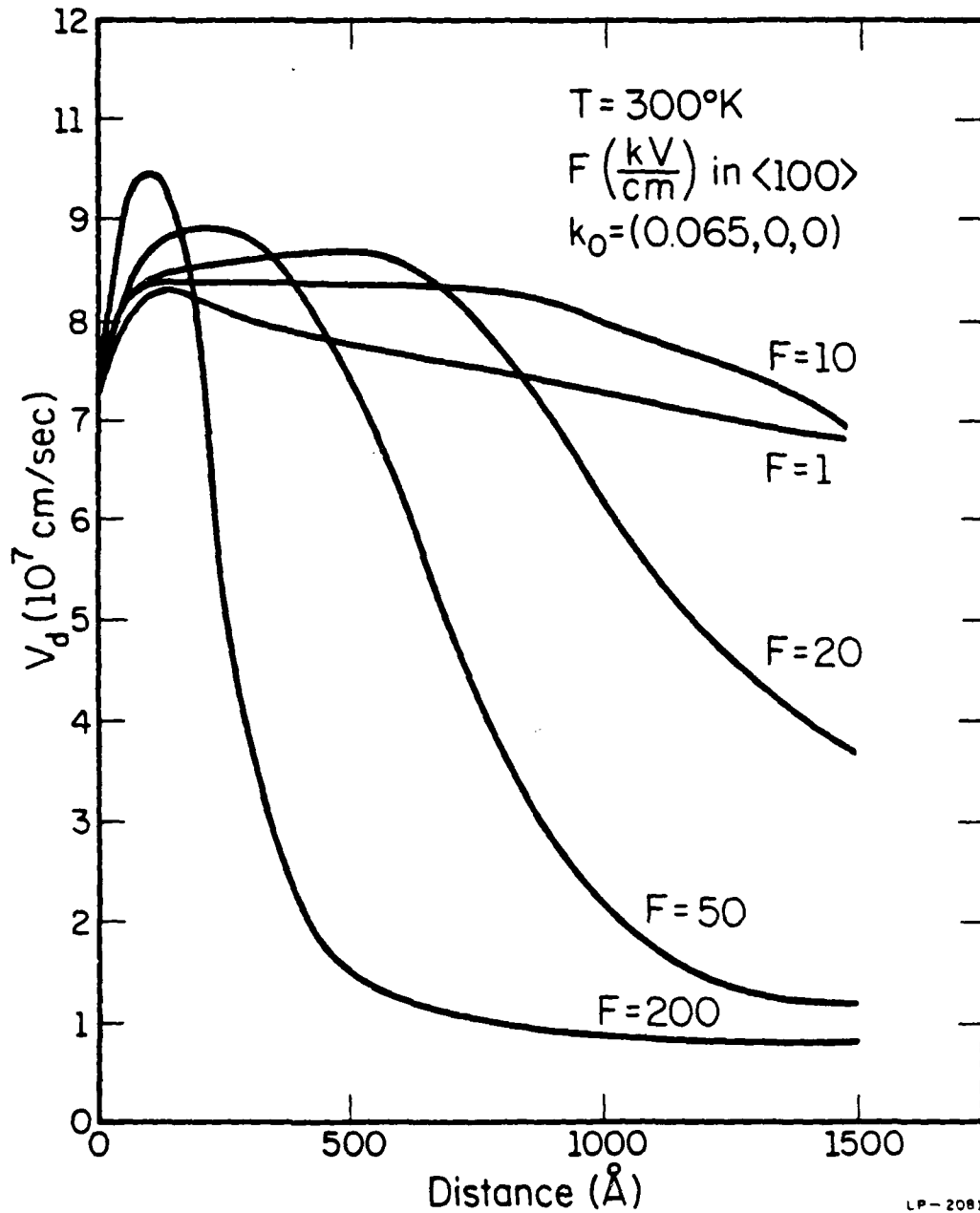
Figure 3.2(a): Average drift velocity versus the device length with
the electric field as a parameter at T = 300 K. The
initial k_o is given in units of $2\pi/a$, where "a" is the
lattice constant. The injection energy corresponding
to k_o is E_o = 0.24 eV.
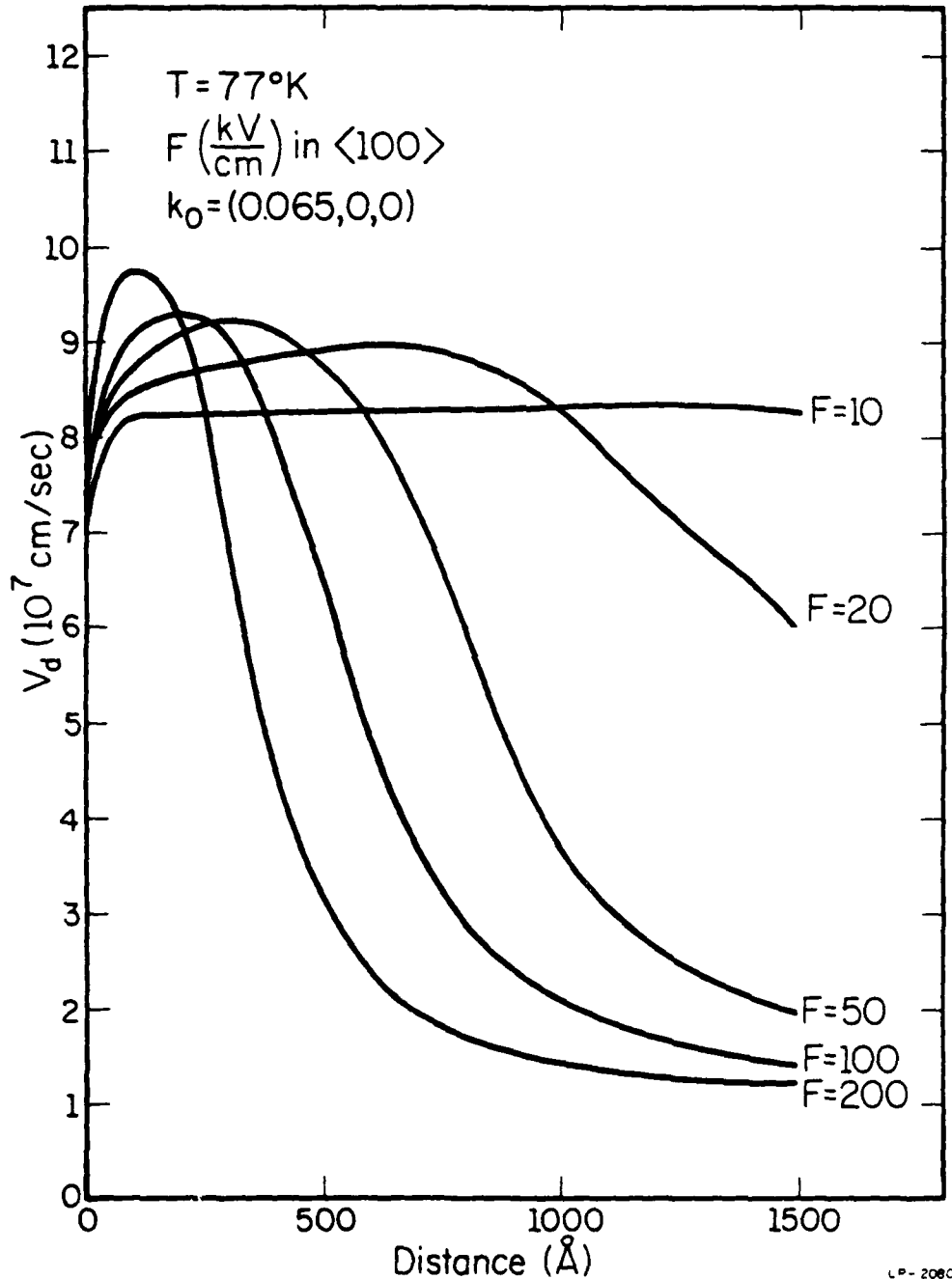
Figure 3.2(b): Average drift velocity versus the device length with the electric field as a parameter at T = 77 K. The initial k_o given in units of $2\pi/a$, where "a" is the lattice constant. The injection energy corresponding to k_o is $E_o = 0.24$ eV.

percentage of unscattered electrons is plotted as a function of the transit length for different field strengths at two temperatures with a fixed injection energy. If we compare Figures 3.3a and b with the corresponding Figures 3.2a and b, we see that the high average drift velocity is a direct result of the unscattered electrons, which verifies the above explanations. Figures 3.4a and b show the average number of scattering events as a function of distance. These plots are, of course, related to Figure 3.3. However, a direct comparison is not possible because electrons scattered to lower energies are scattered again with higher probability than the high energy unscattered electrons.

Before discussing the rest of the results, we compare the differences introduced by a temperature variation. The general characteristic is similar for the two temperatures. However, because of the freeze out of optical phonons at 77 K, effects of collision free transport are stronger and higher transient velocities result. In other words, the CFW is somewhat wider for the lower temperature.

One of the concerns with respect to device operation is the noise equivalent temperature, which is intrinsically related to the carrier diffusion process [39]. We show in Figure 3.5 the energy distribution of electrons at two distances, 700 $\overset{\circ}{A}$ and 1500 $\overset{\circ}{A}$, for a field strength of 20 kV/cm and an injection energy of 0.24 eV. The dotted curves are for 300 K and the full curves for 77 K. The broadening of the distribution function is, under certain simplifying assumptions, roughly related to the noise equivalent temperature [39]. Although the noise equivalent temperature is in general different from the average electron energy (divided
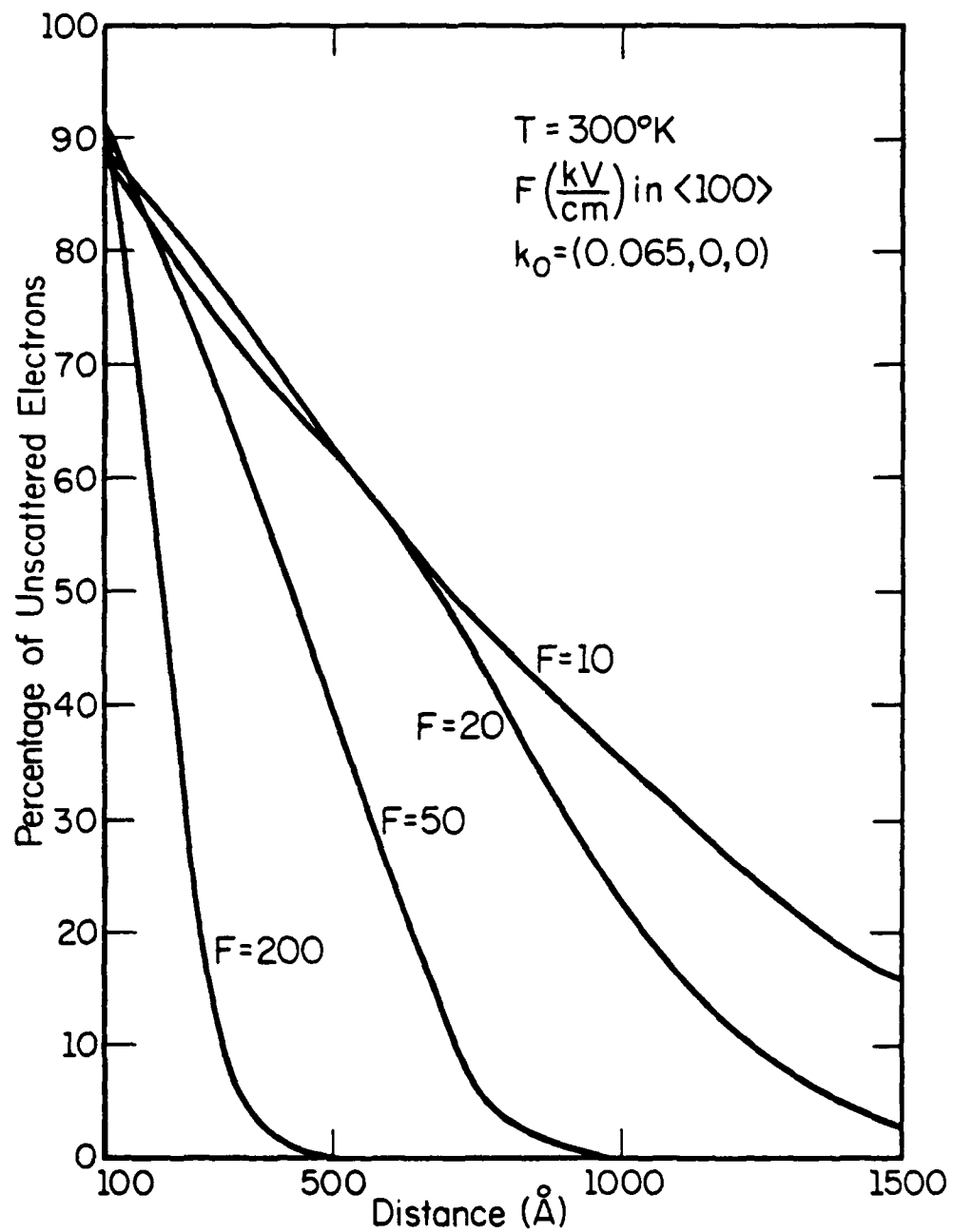
Figure 3.3(a): The percentage of unscattered electrons as a function of device length with the electric field as a parameter at T = 300 K. These curves correspond to those of Figure 3.2a.

The graph shows: Percentage of Unscattered Electrons (y-axis, 0 to 100) versus Distance (Å) (x-axis, 100 to 1500).

Parameters shown on graph:
$$T = 77°K$$
$$F\left(\frac{kV}{cm}\right) \text{ in } \langle 100 \rangle$$
$$k_0 = (0.065, 0, 0)$$

Curves labeled: F=10, F=20, F=50, F=100, F=200

LP-2083
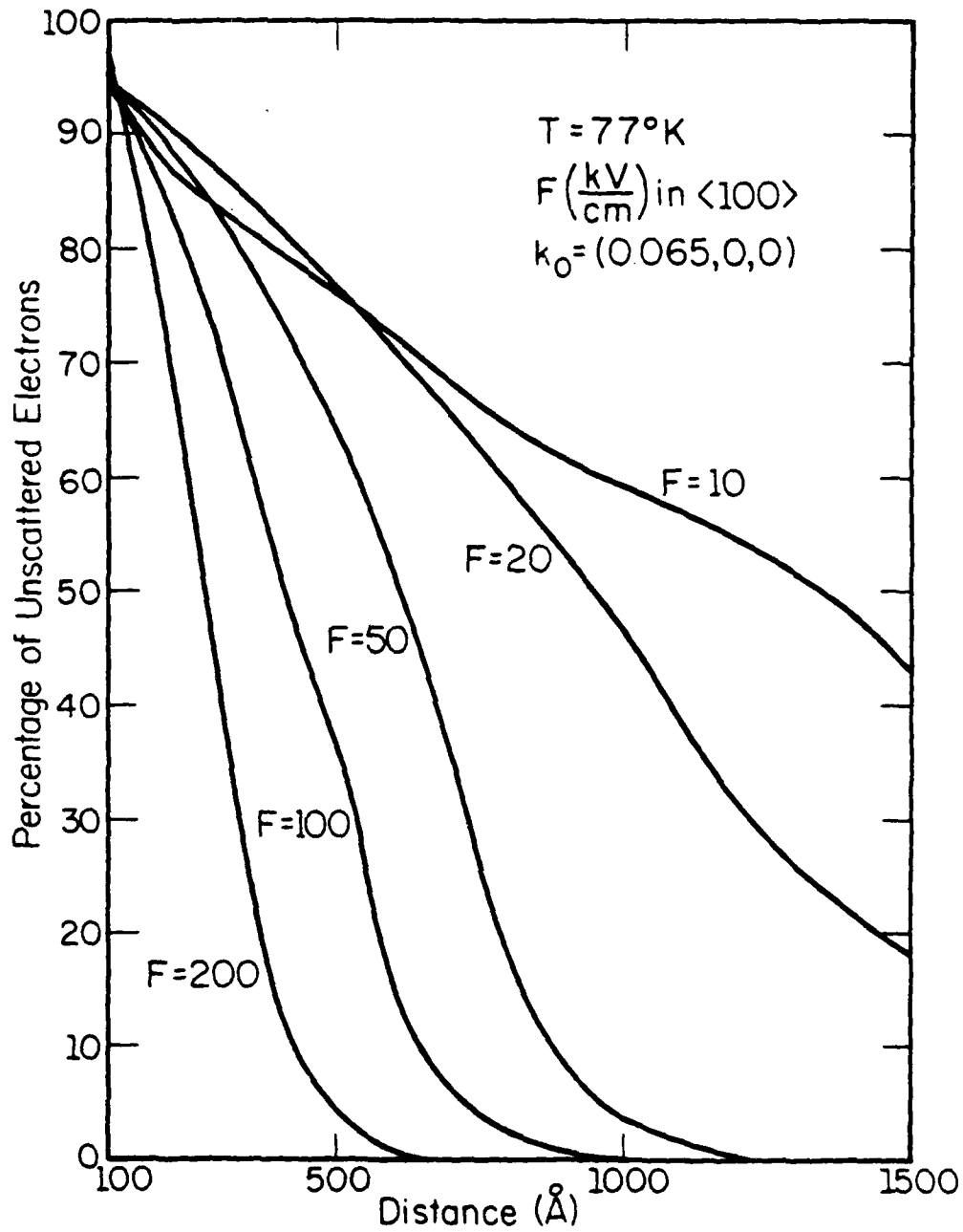
Figure 3.3(b): The percentage of unscattered electrons as a function of device length with the electric field as a parameter at T = 77 K. These curves correspond to those of Figure 3.2b.
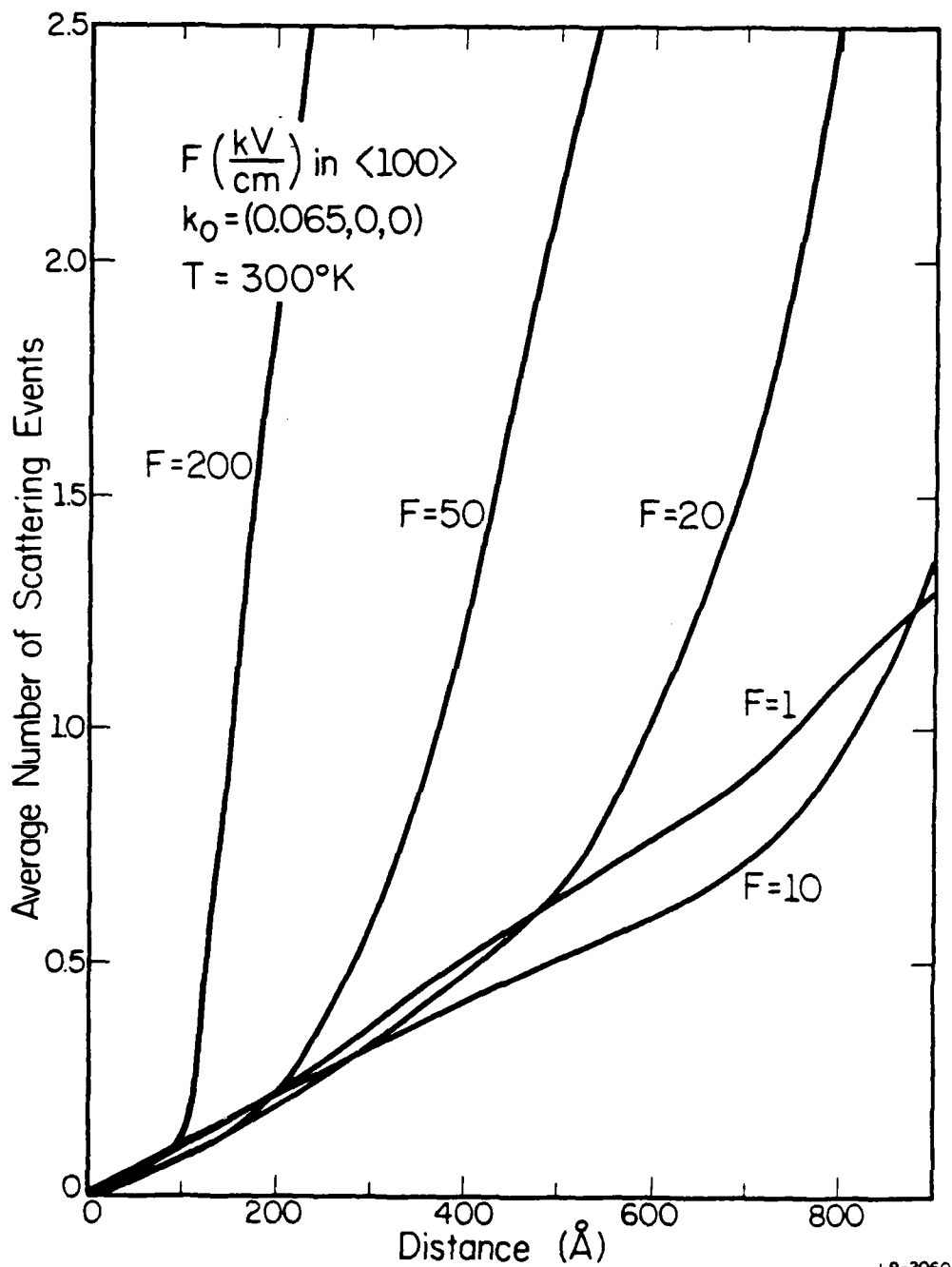
Figure 3.4(a): The average number of scattering events as a function
of device length with the electric field as a parameter
at T = 300 K. The curves here correspond to those of
Figure 3.2a.
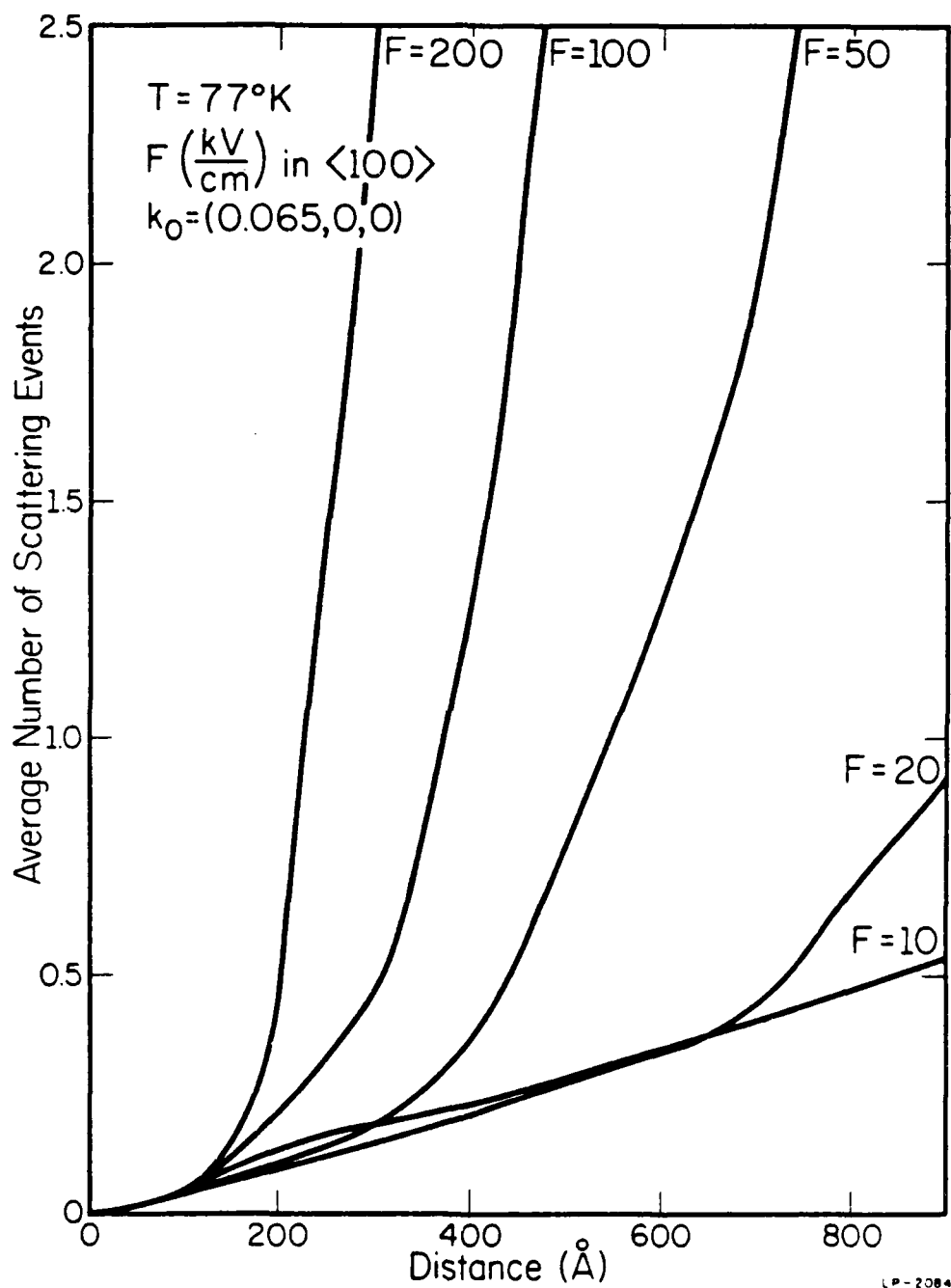
Figure 3.4(b): The average number of scattering events as a function of device length with the electric field as a parameter at T = 77 K. The curves here correspond to those of Figure 3.2b.
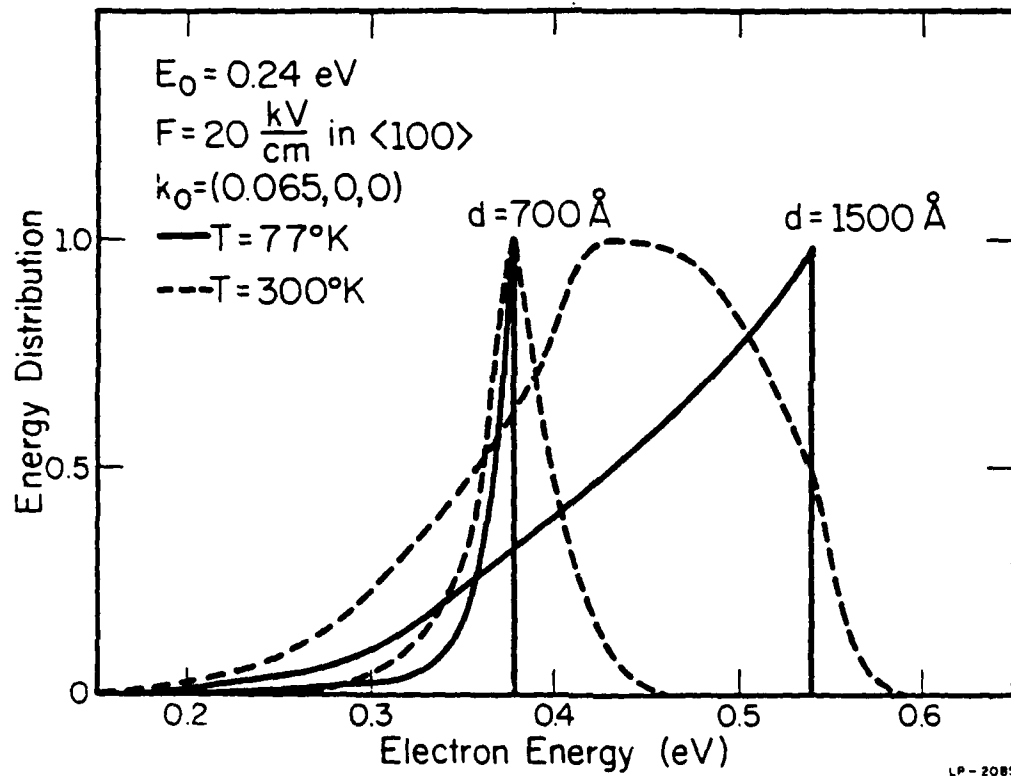
Figure 3.5: Energy distribution at two distances for the two tempera-
tures T = 77 K and T = 300 K. The electric field strength
is 10 kV/cm applied in the <100> direction. The dashed
curves are for T = 300 K and the solid curves are for
T = 77 K.

by the Boltzmann Constant), it is clear from Figure 3.5 that a high
noise equivalent temperature results even for the initial (almost ballis-
tic) regime, especially at room temperature. The sharp edges of the 77 K
energy distributions are due to unscattered electrons. High fields in-
crease the average energy of the electrons and further broaden the
energy distribution, as shown in Figure 3.6. It is interesting to see
that even for a field strength of 100 kV/cm, some unscattered electrons
exist for energies below ~1 eV, which cause the small spike at the high
energy end of the distribution function.

Finally, in Figures 3.7a and b, the ultimate speed (shortest transit
time) of short GaAs structures is plotted. The results show that the
transit times <u>increase</u> with <u>increasing</u> electric field. This paradoxical
result is caused by the high scattering rates to the X and L minima.
Note also that even in the most ideal case, it will be difficult to
achieve a transit time of 1 psec for a transit length of 1000 Å.

3.4 Conclusions

We have demonstrated the existence of high transient velocities for
electrons injected at high energies into GaAs. To achieve high speed,
electrons must be injected at energies close to the energy of the L minima
and must not be accelerated by external fields above this energy (the X
minima are especially detrimental to speed). This limits the injection
energy E_i, electric fields F, and external voltages V to rather narrow
ranges. Assuming a width of 1000 Å for the structure in question, we ob-
tain optimum velocities (speed) for E_o ~ 300 meV, F $\leq$ 35 kV/cm and
V $\leq$ 0.35 volts. An examination of these values immediately suggests that
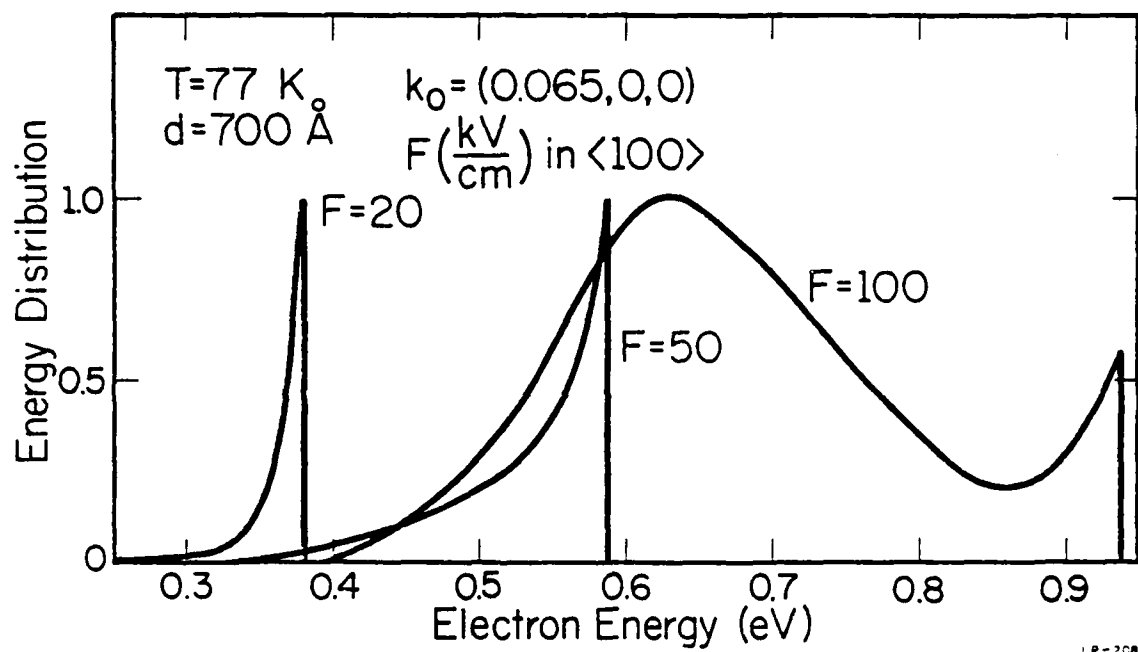
Figure 3.6: Energy distribution at d = 700 Å for T = 77 K. The electric fields are all in the <100> direction and the injection energy is the same as in the previous graphs.
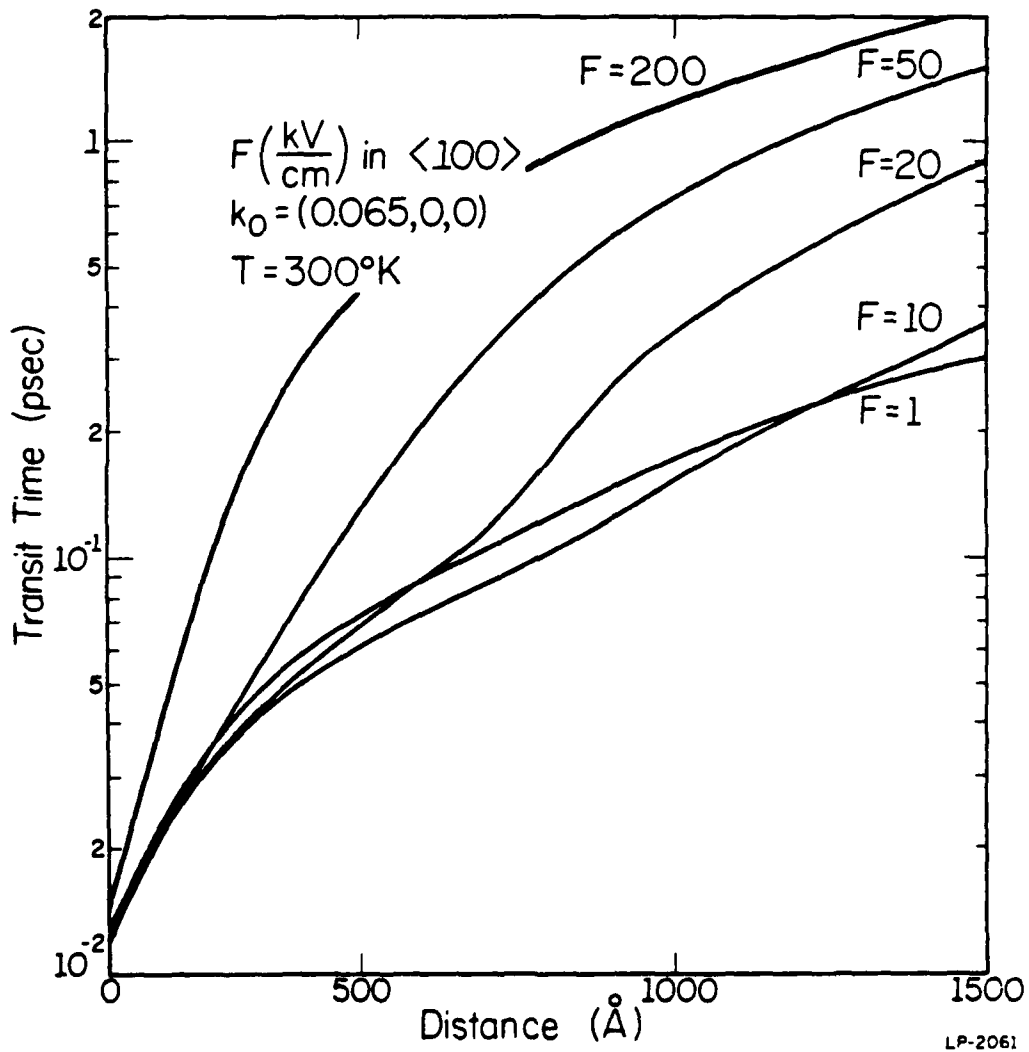
Figure 3.7(a): Transit time of electrons versus the device length with
                the electric field as a parameter at T = 300 K. These
                curves correspond to those of Figure 3.2a.
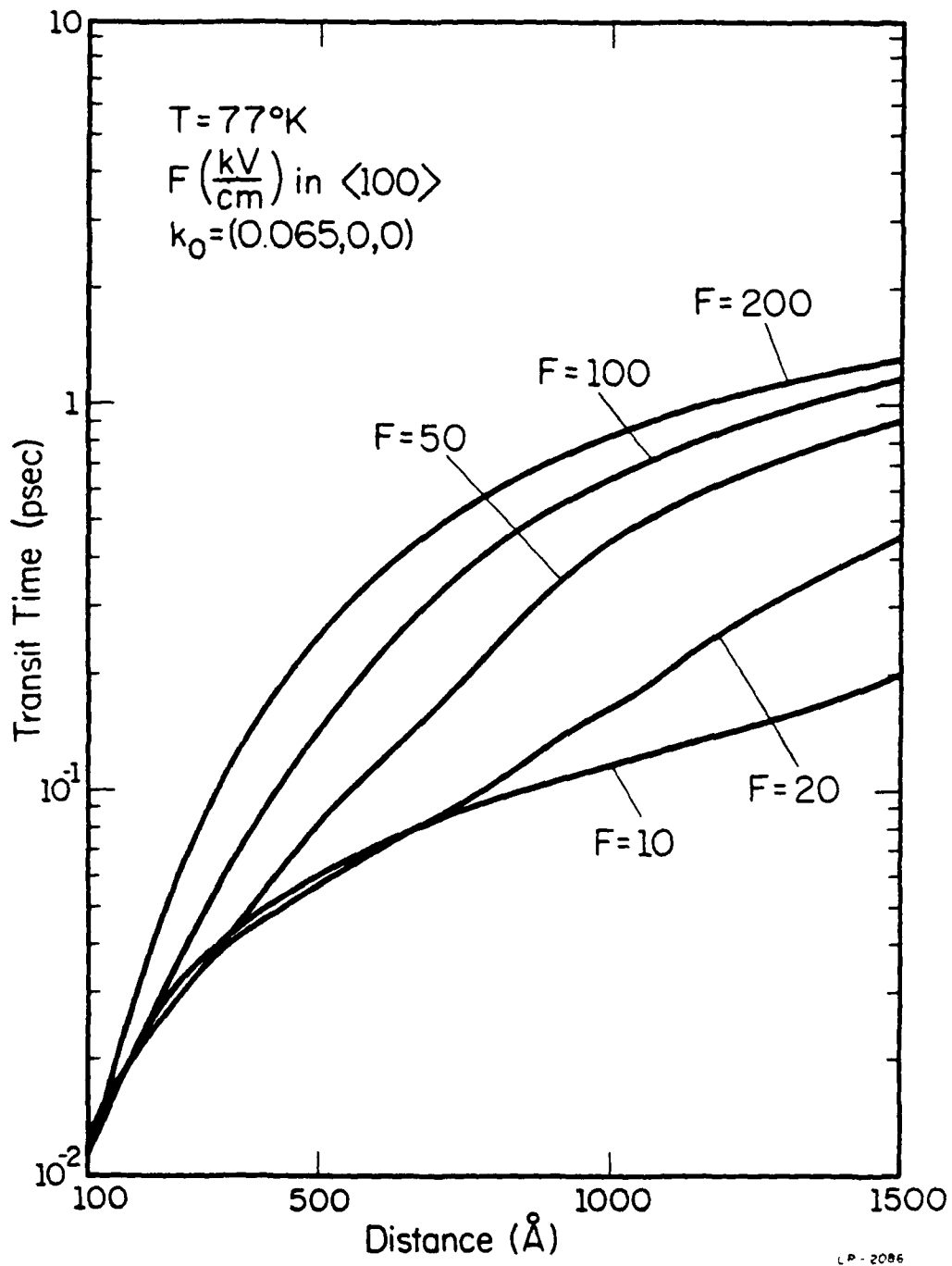
Figure 3.7(b): Transit time of electrons versus the device length with the electric field as a parameter at 77 K. These curves correspond to those of Figure 3.2b.

only emitter (source)- and base-like structures are eligible for ballistic transport; collectors (drains) are not because of unavoidable high voltage drops. The high velocities are caused almost entirely by electrons escaping the intervalley scattering processes which decrease the velocity in an almost step-like manner. Structures substantially longer than 1000 $\overset{\circ}{A}$ will not show ballistic transport except for very low electron energies (just below the optical phonon energy) [34]. It should be noted, however, that even for transit lengths of 1000 $\overset{\circ}{A}$ and below, the noise equivalent temperature can be exceedingly high. Because of the high voltage drops at collectors and drain regions, current devices will hardly show pronounced velocity improvement.

CHAPTER 4

STEADY STATE HIGH FIELD TRANSPORT IN Si

4.1 Introduction

Silicon has been the most extensively studied semiconductor material since the invention of the transistor. Especially the transport properties of the material, which are important in device operations, have been intensively studied both experimentally and theoretically by many authors [40-45]. In the past, theoretical transport studies have been limited to intermediate electric field strengths (<50 kV/cm) largely because of the breakdown of the effective mass approximation at higher field strengths. In practical device operations, electric fields can be well above 50 kV/cm, for example at the drain end of a short channel MOSFET. In order to penetrate further into the band and im- prove the understanding of the high field transport properties of the material, one has to abandon the effective mass approximation and adopt a more realistic band structure. We follow the scheme developed by Shichijo and Hess [12] who first incorporated into the Monte Carlo simu- lation a realistic band structure as calculated by the empirical pseudo- potential method. We have improved the original model and included two conduction bands for the silicon study.

This chapter is devoted to the study of the steady state high field transport properties of silicon. Because of the inclusion of two con- duction bands, we are able to investigate very high field transport

properties (>100 kV/cm), for example, impact ionization. In Section 4.2, we discuss the band structure and the scattering mechanisms in silicon. In Section 4.3, we show the results of the simulation by using the conventional Keldysh formalism for the secondary pair generation rate and compare them to the experimental results. In Section 4.4, we examine the large difference in the secondary pair generation rates calculated by Keldysh's formalism and Kane's direct pseudopotential calculation. It is found that one can adjust the high energy phonon scattering rates and the secondary pair generation rates to both (Keldysh and Kane) models and still find a decent fit of the theoretical results to the experimental data.

4.2 Theoretical Model

The model for Monte Carlo simulation has two main ingredients: the band structure and the scattering rate. We described in the following sections the different features that have been included in our model and the advantages it has over other models.

4.2.1 Band Structure

Figure 4.1 shows the band structure of silicon calculated by the empirical pseudopotential method [37]. Note that the first conduction band and the second conduction band intersect at the X point, where the energy of the state is about 0.1 eV. For a moderately high electric field, the average energy of the electrons easily gets above 0.1 eV and interband transitions occur. Unlike the case for GaAs, where the second conduction band lies significantly higher, one has to include the second
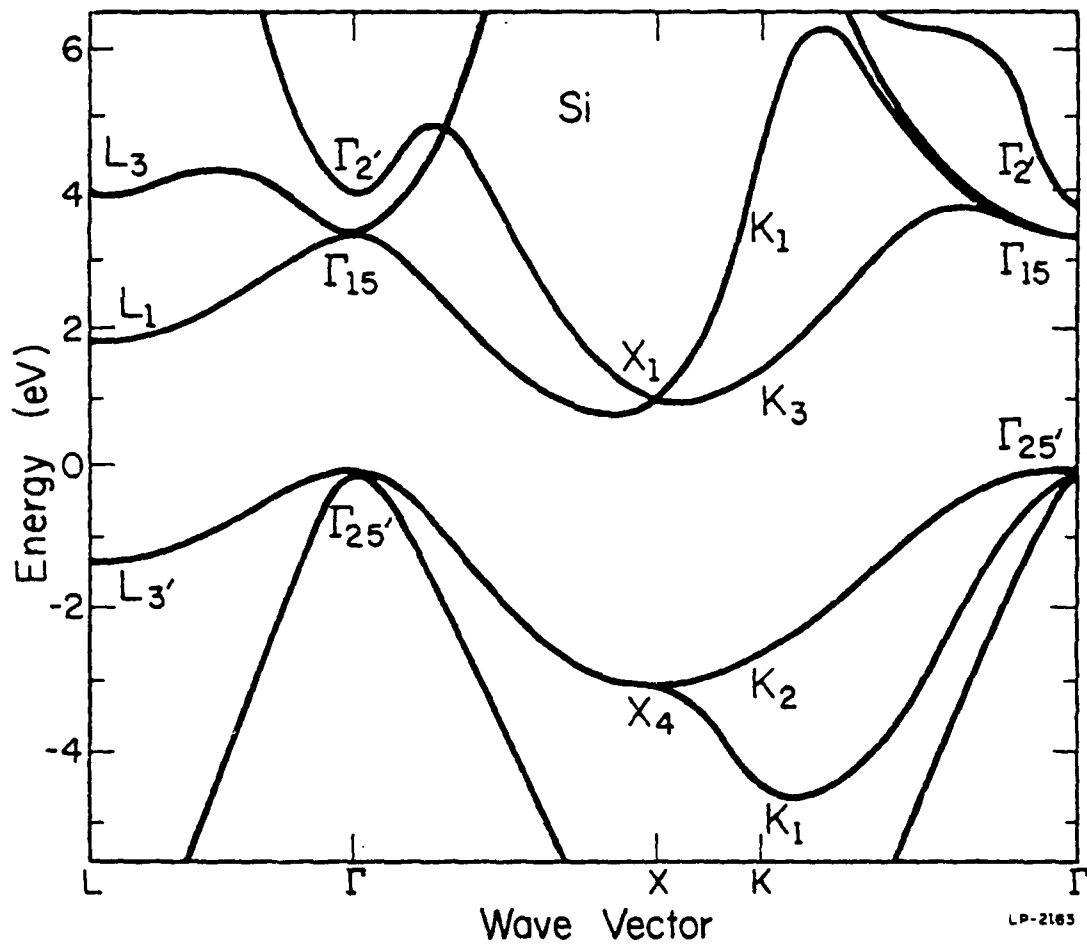
Figure 4.1: The band structure of silicon calculated by the empirical pseudopotential method [37].

band in the case for silicon. Note, also, that the L minimum is only
1 eV above the X minimum. Under very high electric fields (>100 kV/cm)
where impact ionization phenomena are important, one can expect that the
L valleys play an important role.

Another transport process of interest to us, which is discussed
in Chapter 5, is the emission of electrons into silicon dioxide. The
potential barrier at the interface of silicon and silicon dioxide is
about 3.1 eV. It is clearly necessary to look carefully into the band
structure and see where in the Brillouin zone such a process is possible
before investigating transport at such high energies. Figure 4.2 shows
a cross section of the Brillouin zone. The isoenergy lines corresponding
to this cross section are shown in Figures 4.3a and b for the first and
the second conduction bands respectively. We see that the X valleys of
the first conduction band are more elliptic, while for the second con-
duction band, they are more isotropic. Note that there is only a small
region near the W point for the first conduction band that is above 3 eV
on this cross section. Figure 4.4 shows another cross section of the
Brillouin zone, and Figures 4.5a and b illustrate the isoenergy lines cor-
responding to that cross section for the two bands. Note that, on this
cross section, the energies are always below 3 eV for the first conduction
band. Thus, it is essential that one includes the second conduction band
in order to look at high energy processes like the emission of electrons
over the silicon-silicon dioxide barrier.

Because of the symmetry properties, we only need to calculate
points inside the irreducible wedge of the Brillouin zone. By means of
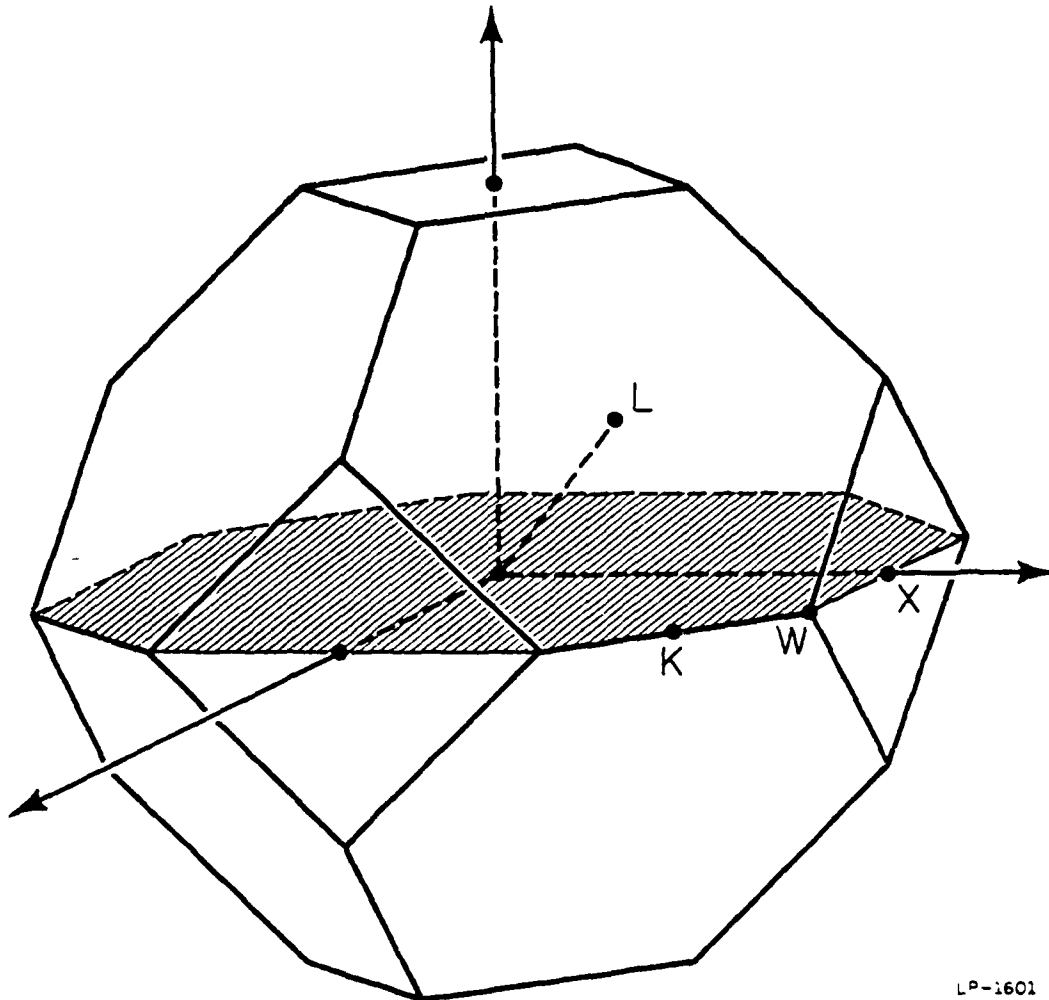
Figure 4.2: A cross section of the Brillouin zone.

LP-2194
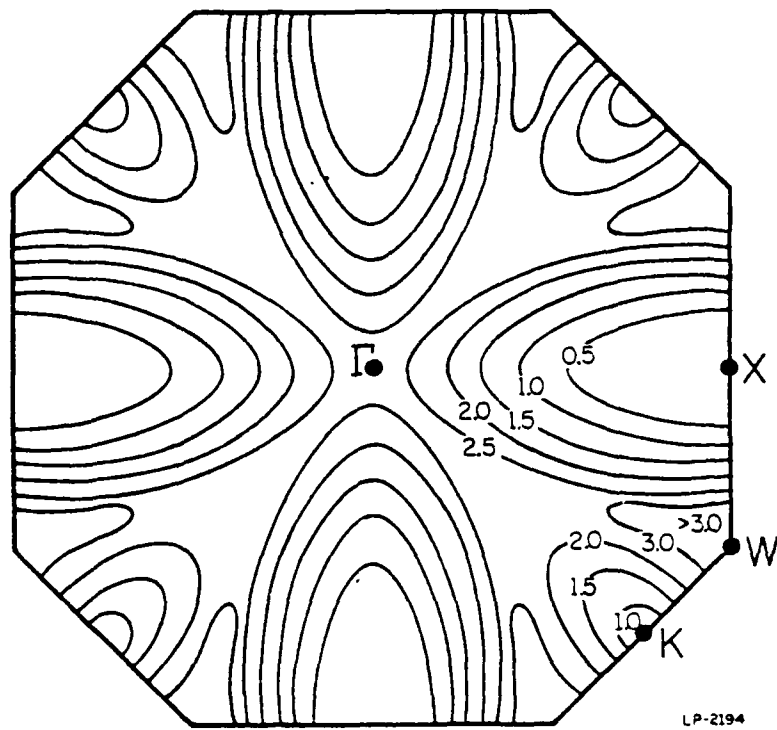
Figure 4.3(a):   Equal energy surfaces for the ... st
conduction band of silicon corresponding
to the cross section of Figure 4.2.

Figure 4.3(b): Equal energy surfaces for the second
conduction band of silicon corresponding
to the cross section of Figure 4.2.
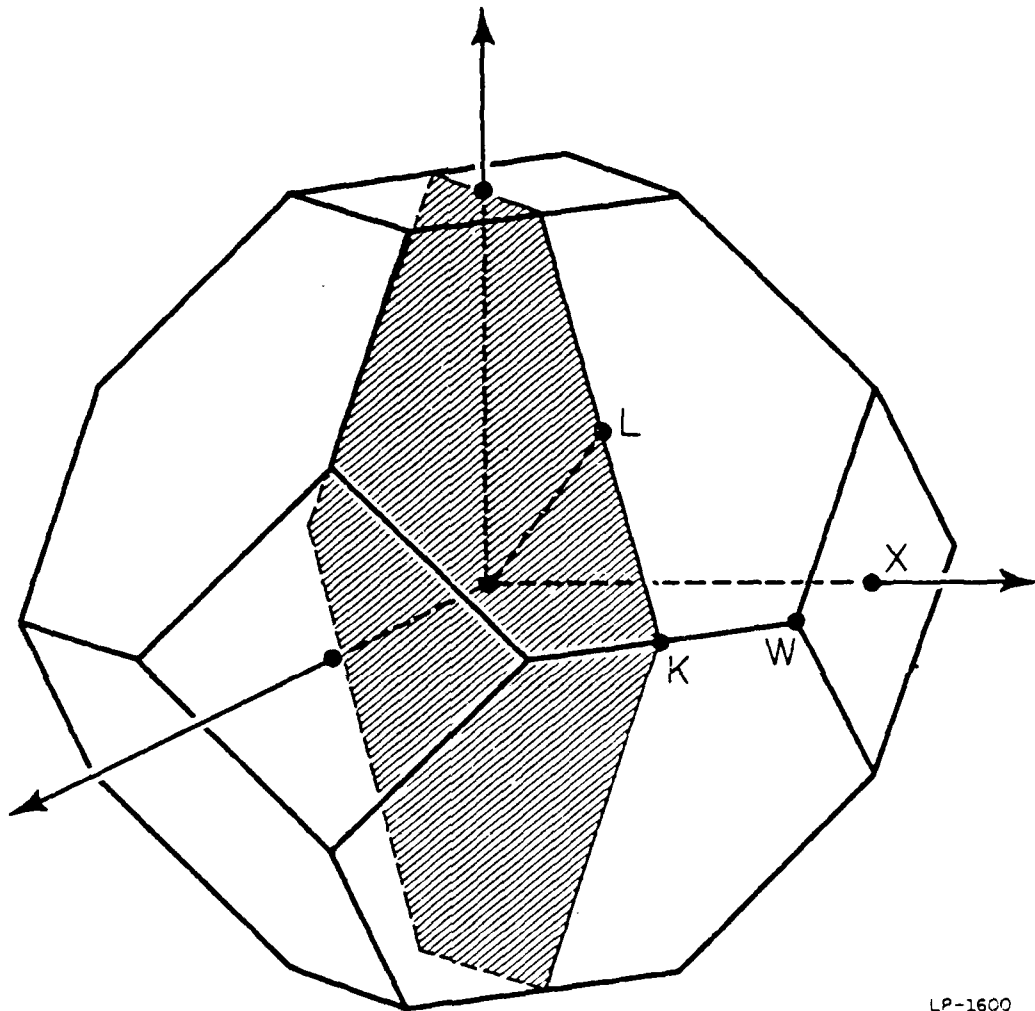
LP-1600

Figure 4.4: A cross section of the Brillouin zone.
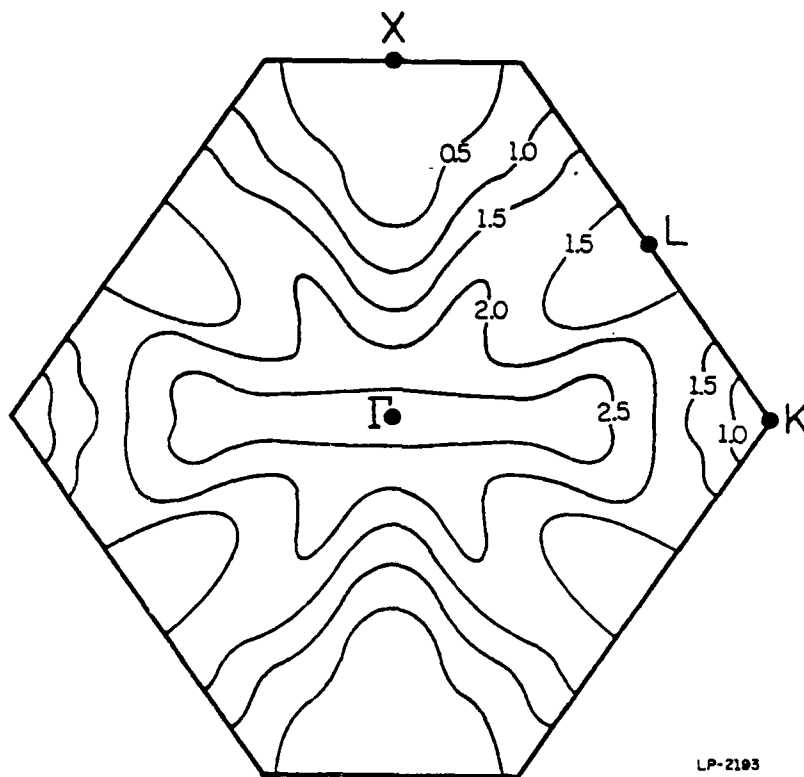
Figure 4.5(a):   Equal energy surfaces for the first
conduction band of silicon corresponding
to the cross section of Figure 4.4.
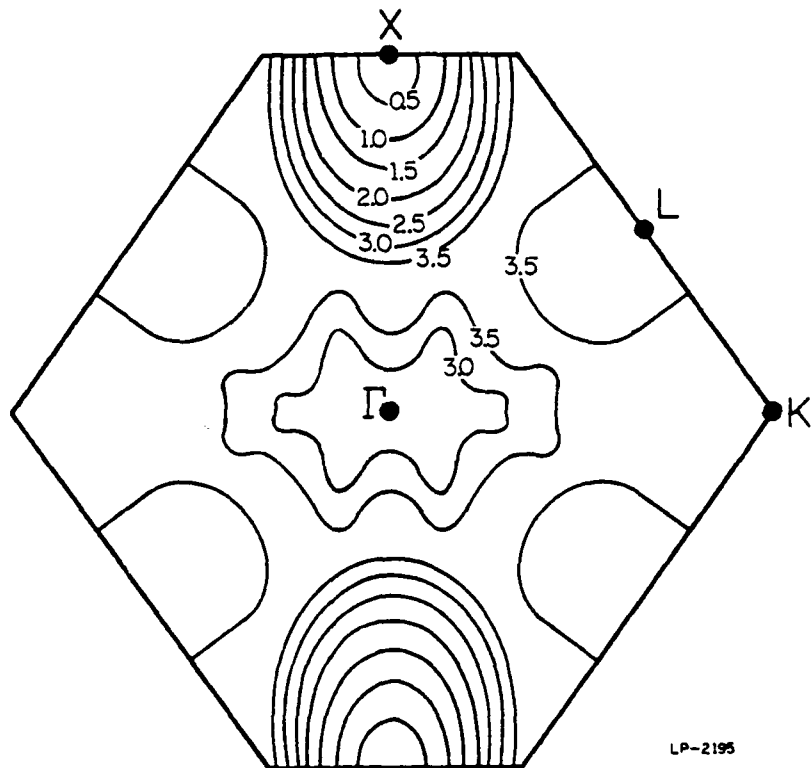
Figure 4.5(b):   Equal energy surfaces for the second
                 conduction band of silicon corresponding
                 to the cross section of Figure 4.4.

the 48-fold symmetry operations, one easily recovers the whole

Brillouin zone.

As described in Reference 25, 152 points inside the irreducible

wedge plus another 97 points around the wedge (necessary for interpo-

lations) were directly calculated by the empirical pseudopotential

method. Table 4.1 lists the calculated $E(\vec{k})$ relation for these 249

points.

4.2.2 Scattering Rate

The scattering mechanisms included in our Monte Carlo simulation

are the following: intravalley acoustic scattering, X to X equivalent

intervalley f-scattering, X to X equivalent intervalley g-scattering,

and X to L nonequivalent intervalley scattering, which has never been

considered in previous works. By definition, f-scattering is the

scattering of electrons to any of the four neighboring X valleys, for

example, from (100) valley to (010) valley, and g-scattering is the

scattering of electrons to the opposite valley, for example, from (100)

valley to (-100) valley. We follow closely the work by Canali et al.

in calculating the low energy scattering rates [18]. For X to X coupling,

we consider several possible phonon types (3f and 3g) [18,42]. The dif-

ference between f and g scatterings is taken into account in the simula-

tion process by properly selecting the scattering final states. For

intravalley acoustic scattering, the energy exchange between electrons

and phonons is taken into account. The X to L coupling constants were

assumed to be the same for all four possible phonons determined from the

Table 4.1a: E($\vec{k}$) relation for the lowest conduction band of Si

(E in eV from conduction band edge; $\vec{k}$ in units of $2\pi/a$)

$k_x \longrightarrow$ $k_y \longrightarrow$ $k_z \longleftarrow$

$k_z = 0.5$

k_x					
0.4	1.7916	1.3711	1.3398	1.7043	2.0763
0.5	1.3398	1.0620	1.3398		
0.6	1.3398				

$k_z = 0.4$

k_x								
0.3	2.0337	1.5916	1.4935	1.7916	1.9863	1.8149	1.5864	1.4353
0.4	1.4935	1.1580	1.3711	1.7504	1.7969	1.6380		
0.5	1.3711	1.3398	1.7043	2.0816				
0.6	1.7043	1.7504						

$k_z = 0.3$

k_x										
0.2	2.3319	1.9664	1.8294	2.0337	2.0421	1.7240	1.3822	1.1166	0.9495	0.8959
0.3	1.8294	1.4431	1.5916	1.8476	1.6973	1.3885	1.1274	0.9594	0.9047	
0.4	1.5916	1.4935	1.7916	1.9863	1.8149	1.5864	1.4353			
0.5	1.7916	1.8317	2.0763	2.4798	2.4268					
0.6	2.0763	1.7969	1.8149							
0.7	1.8149									

$k_z = 0.2$

k_x											
0.1	2.3048	2.3474	2.3151	2.3319	2.0441	1.6503	1.2804	0.9726	0.7379	0.5951	0.5453
0.2	2.3151	1.9196	1.9664	2.0321	1.7291	1.3329	0.9749	0.7015	0.5313	0.4715	
0.3	1.9664	1.8294	2.0337	1.7240	1.3822	1.1166	0.9495	0.8959			
0.4	2.0337	2.0822	2.3141	2.4292	2.1612	1.9140	1.7553	1.7052			
0.5	2.3140	2.0967	2.1061	2.4268	2.8269	2.7771					
0.6	2.1061	1.6380	1.5864	1.9140							
0.7	1.5864	1.1274									

k_y: 0.0 0.1 0.2 0.3 0.4 0.5 0.6 0.7 0.8 0.9 1.0

$k_x \longrightarrow$

Table 4.1b: $E(\vec{k})$ relation for the lowest conduction band of Si

(E in eV from conduction band edge; $\vec{k}$ in units of $2\pi/a$)

$k_z = 0.1$

k_x \ k_y	0.0	0.1	0.2	0.3	0.4	0.5	0.6	0.7	0.8	0.9	1.0
0.0	2.4517	2.6803	2.3048	1.8307	1.3698	0.9668	0.6452	0.4156	0.2856	0.2694	0.3724
0.1	2.6803	2.4506	2.3474	1.9966	1.5594	1.1491	0.8042	0.5351	0.3505	0.2467	0.2122
0.2		2.3474	2.3151	2.3319	2.0441	1.6512	1.2804	0.9726	0.7379	0.5951	0.5453
0.3			2.3319	2.4798	2.5943	2.3927	2.0419	1.7286	1.4958	1.3455	1.2927
0.4				2.5943	2.5573	2.5958	2.9033	2.7125	2.4805	2.3352	2.2895
0.5					2.5958	2.1161	2.0265	2.2952	2.7806	3.2498	3.3423
0.6						2.0265	1.5098	1.4353	1.7553	2.3352	
0.7							1.4353	0.9594	0.9495		
0.8								0.9495			

$k_z = 0.0$

k_x \ k_y	0.0	0.1	0.2	0.3	0.4	0.5	0.6	0.7	0.8	0.9	1.0
0.0	2.6197	2.4517	2.0437	1.5591	1.0944	0.6881	0.3665	0.1344	0.0167	0.0096	0.1248
0.1	2.4517	2.6803	2.3048	1.8307	1.3698	0.9669	0.6452	0.4156	0.2856	0.2694	0.3724
0.2		2.3048	2.9092	2.5095	2.0708	1.6779	1.3576	1.1262	0.9850	0.9555	1.0337
0.3			2.5095	2.9973	3.0108	2.6367	2.3249	2.0938	1.9623	1.9103	1.9667
0.4				3.0108	2.6938	2.6356	2.8819	3.2282	3.0818	3.0218	3.0417
0.5					2.6356	2.1034	1.9886	2.2498	2.7401	3.3423	3.8618
0.6						1.9886	1.4627	1.3872	1.7052	2.2895	3.0417
0.7							1.3871	0.9047	0.8959	0.8959	1.2927
0.8								0.8959	0.4715		

$k_y \longrightarrow$

$k_z \longleftarrow$
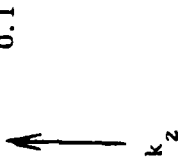
Table 4.1c: E($\vec{k}$) relation for second highest conduction band of Si

(E in eV from conduction band edge; $\vec{k}$ in units of $2\pi/a$)

$k_x \longrightarrow$

$k_z = 0.5$

					k_x
3.0595	3.0924	3.1454	2.9724	2.9639	0.4
	3.1454	3.1729	3.1454		0.5
		3.1454			

$k_z = 0.4$

								k_x
3.2391	3.2282	3.3496	3.0595	3.0725	3.6072	4.3137	5.0329	0.3
	3.3496	3.2811	3.0924	3.0643	3.5580	4.3648		0.4
		3.3496	3.1454	2.9724	2.9645			0.5
			3.0924	2.9724	3.0644			0.6

$k_z = 0.3$

										k_x
3.1676	3.2486	2.4355	3.2391	3.3814	3.9203	4.1634	4.0005	3.8567	3.8125	0.2
	3.4355	3.4976	3.2282	3.1678	3.7027	4.4401	4.8463	4.8671	4.8541	0.3
	3.2281	3.3496	3.0595	3.0725	3.6072	4.3137	5.0329			0.4
		3.0595	3.1823	2.9639	2.7399	3.1766				0.5
			2.9639	3.5580	3.6072					0.6
				3.6072						0.7

$k_z = 0.2$

											k_x
3.1414	2.9221	3.1301	3.1676	3.6762	3.5999	2.9478	2.4436	2.0801	1.8630	1.7928	0.1
	3.1301	3.4527	3.2486	3.3771	4.0245	3.7174	3.2917	2.9904	2.7979	2.7349	0.2
		3.2486	3.4355	3.2391	3.3814	3.9203	4.1634	4.0005	3.8566	3.8125	0.3
			3.2391	3.4900	3.0893	2.9899	3.4828	4.1112	4.6270	4.7685	0.4
				3.0893	3.6050	3.4392	3.1766	3.1084	3.7082		0.5
					3.4392	4.3648	4.3137	4.1111			0.6
						4.3137	4.8463				0.7

| 0.0 | 0.1 | 0.2 | 0.3 | 0.4 | 0.5 | 0.6 | 0.7 | 0.8 | 0.9 | 1.0 |

$k_y \longrightarrow$

$\longleftarrow k_z$

Table 4.1d: E(k⃗) relation for second highest conduction band of S1

(E in eV from conduction band edge; k⃗ in units of $2\pi/a$)

$k_x \longrightarrow$

$k_z = 0.1$

	0.0	0.1	0.2	0.3	0.4	0.5	0.6	0.7	0.8		
	2.8662	2.7226	3.1414	2.7623	3.6538	2.8345	2.0831	1.4559	0.9636	0.5991	0.3725
	2.7226	2.9312	2.9221	3.4398	3.7938	3.0319	2.3191	1.7387	1.3092	1.0387	0.9485
	2.9221	3.1301	3.1676	3.6762	3.6001	2.9278	2.4436	2.0801	1.8630	1.7928	
	3.1676	3.4691	3.2619	3.4833	3.7123	3.3567	3.0647	2.8865	2.8225		
	3.2619	3.7389	3.4041	3.0256	3.3820	3.9169	3.9087				
	3.4041	4.3355	4.1455	3.8846	4.7088	4.7617	4.1089				
	4.1455	5.1978	5.0329	4.6270	3.9169						
	5.0329	4.8671	3.8566								
	3.8566										

$k_z = 0.0$

	0.0	0.1	0.2	0.3	0.4	0.5	0.6	0.7	0.8		
	2.6197	2.8662	3.4764	4.2484	3.5262	2.6759	1.9050	1.2585	0.7480	0.3661	0.1248
	2.8661	2.7226	3.1414	3.7623	3.6538	2.8345	2.0831	1.4559	0.9636	0.5991	0.3724
	3.1414	2.9715	3.2307	3.7550	3.3023	2.5991	2.0168	1.5579	1.2327	1.0337	
	3.2407	3.3543	3.1204	3.5025	3.3402	2.8236	2.4233	2.1348	1.9667		
	3.1204	4.0063	3.7503	3.4551	3.2420	3.3073	3.1566	3.0417			
	3.7503	4.8311	4.6678	4.4399	4.2619	4.1089	3.8619				
	4.6678	5.6637	5.4216	4.7685	3.9087	3.0417					
	5.4216	4.8541	3.8125	2.8225							
	3.8126	2.7348									

0.0	0.1	0.2	0.3	0.4	0.5	0.6	0.7	0.8	0.9	1.0

$k_y \longrightarrow$

k_z

phonon spectrum [46-48] and were found by fitting the calculated results to the experimental results.

The effective mass density of states with the nonparabolicity factor included was used in calculating the low energy scattering rates. It is not appropriate to simply extend these scattering rates to higher energies because the effective mass approximation breaks down at higher energies and the density of states starts decreasing at some critical point. The intervalley scattering rate, which is proportional to the final density of states, should be modified at higher electron energies. Therefore we have calculated the total density of states for the two conduction bands for Si. As discussed in Section 2.2, we modify the high energy scattering rates to behave like the density of states. The details of the mathematics in calculating the scattering rates are summarized in Appendix 2.

For the interband coupling, we consider the interband and intraband scatterings with the same type of phonons and the same coupling strength. In other words, electrons see the same scattering rates both in bands 1 and 2 and get scattered equally likely into possible final states in both bands. This simplifies drastically the problem with interband and intraband scatterings in the simulation. One can assume independent coupling parameters for interband scatterings and adjust them to fit to the experiment. But with interband deformation potentials and interband overlap integrals essentially unknown, one currently does not refine the model by adding in extra parameters.

Impact ionization can be treated as an additional scattering mechanism in the Monte Carlo simulation. In previous works [49-54], this

secondary pair generation rate was always calculated by Keldysh's empirical formula:

$$\frac{1}{\tau_{ii}(E)} = \frac{P}{\tau_{ph}(E_{th})} \left(\frac{E - E_{th}}{E_{th}} \right)^2 , \qquad (4.1)$$

where E_{th} is the threshold energy for impact ionization, $\tau_{ph}(E_{th})$ is the total phonon scattering rate at the ionization threshold energy E_{th}, and P is a constant. It has been shown that the impact ionization coefficient is essentially unchanged as long as P is much greater than one. This amounts to saying that impact ionizations occur almost immediately for electrons with energies above the threshold energy.

Kane has done a direct calculation of the secondary pair generation rate in silicon using the pseudopotential wave function and assuming two particle interaction only [55]. Surprisingly, his calculated rate is much lower than the rate calculated from Keldysh's formula. We have performed a full investigation on the discrepancy. In Section 4.3, we show the results of the simulation following the conventional Keldysh formalism. In Section 4.4, we compare, in detail, the results for three cases: 1. the rate calculated from the conventional Keldysh formalism with P>>1; 2. the rate calculated from Keldysh's formalism but with P<1; 3. the rate from Kane's direct pseudopotential calculation.

4.2.3 Temperature Effects

We assume that the band structure is essentially unaltered by the temperature effect, except that the band gap is modified. We further

assume that the threshold energy of impact ionization can be scaled
according to the formula

$$E_{th}(T) = \frac{E_g(T)}{E_g(300 \text{ K})} \cdot E_{th}(300 \text{ K}) \ . \tag{4.2}$$

The formula for the temperature dependence of the band gap E_g can be
found in [56]. With the above assumptions, the temperature variation
on impact ionization coefficient can be investigated by using Keldysh's
formalism.

4.2.4 Collision Broadening Effect

As the scattering rate goes up to 10^{14} per second, the energy of
the electron is uncertain within $\hbar/\tau$ according to the uncertainty
principle. ΔE is about 100 meV for $1/\tau$ higher than 10^{14}. In determining
the final state after each scattering, we consider the states within a
fixed range ΔE of the true final state energy as possible candidates.
We then randomly choose one of those candidates as the final state, keep-
ing the average energy loss (gain) constant. Part of the collision
broadening effect should be taken into account automatically by so doing.
In Chapter 6, a better method taking into account the Lorentzian shape
of the collision broadening is discussed. For all simulations in Chapters
5 and 6, the collision broadening effect is only partly accounted for as
described above.

4.3. Keldysh's Formalism : P = 100

Using Keldysh's formula with P = 100, we have calculated drift
velocities in the <111> direction for high electric fields and compared

them to the recent high field experimental results by Smith et al. [18, 57]. As is shown in Figure 4.6, our calculated high field results are in good agreement with the experimental results. In Figure 4.7, we show the calculated results of the electron impact ionization rate at two temperatures, 100 K and 300 K. For 300 K our results seem to agree better with Lee and Logan's results than with Overstraeten and De Man's results. We did not find any orientational dependent ionization rate in Si. Since the previous work by Shichijo et al. [12] did not find any orientational dependence of the electron ionization coefficient in GaAs with the same kind of approach, it leads us to believe that the orientational effect is connected with some complicated effects.

As discussed by Hess et al. in a recent paper [61], the answer to the anisotropy may lie in the inhomogeneity of the electric field. In the transient regime, the statistics of impurities most probably is an important factor and it is conceivable that aggregates of, for example, Poisson distributed impurities, led to high local field fluctuations and impact ionization enhancements as described by Shockley [50] and recently for superlattices by Chin et al. [4]. The corresponding enhancement of the electron ionization coefficient as described by Chin et al. is essentially ballistic and may be a source of the anisotropy. As we mentioned in Section 4.2, the first two conduction bands were included in the model. We show some interesting but important results in Figure 4.8 which tell us the important role played by the second conduction band in the transport of electrons in Si. We plotted on the graph both the second band effect and the average energy of electrons as a function of
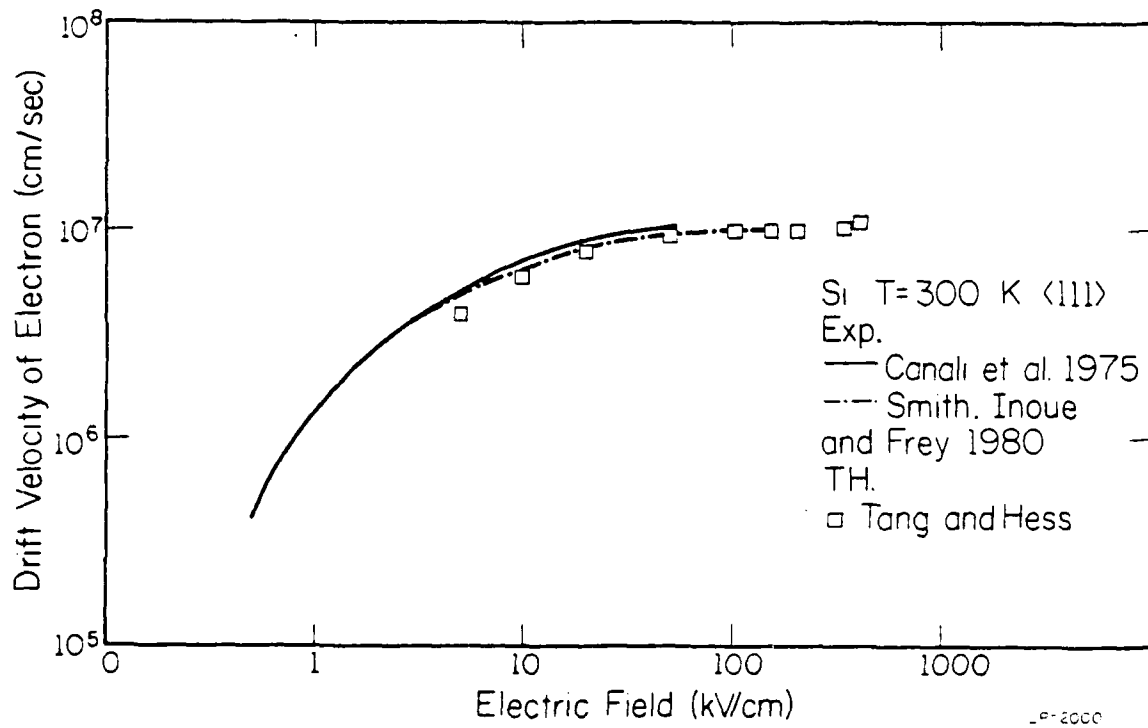
Figure 4.6: Calculated drift velocities for silicon along the <111>
direction. The dashed line and the solid line are the
experimental reults.
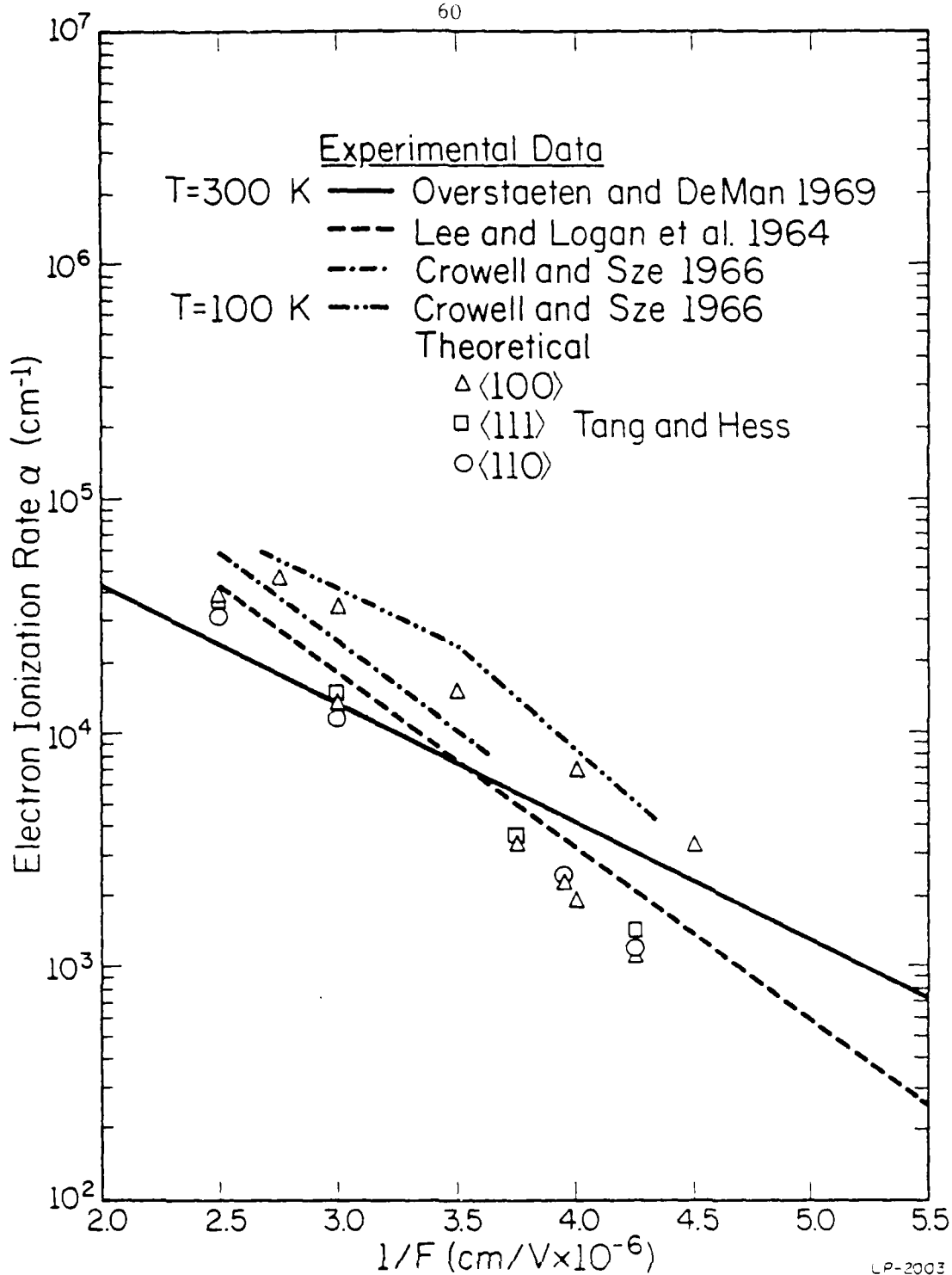
Figure 4.7: Calculated electron ionization coefficient α
plotted as a function of inverse field strength.
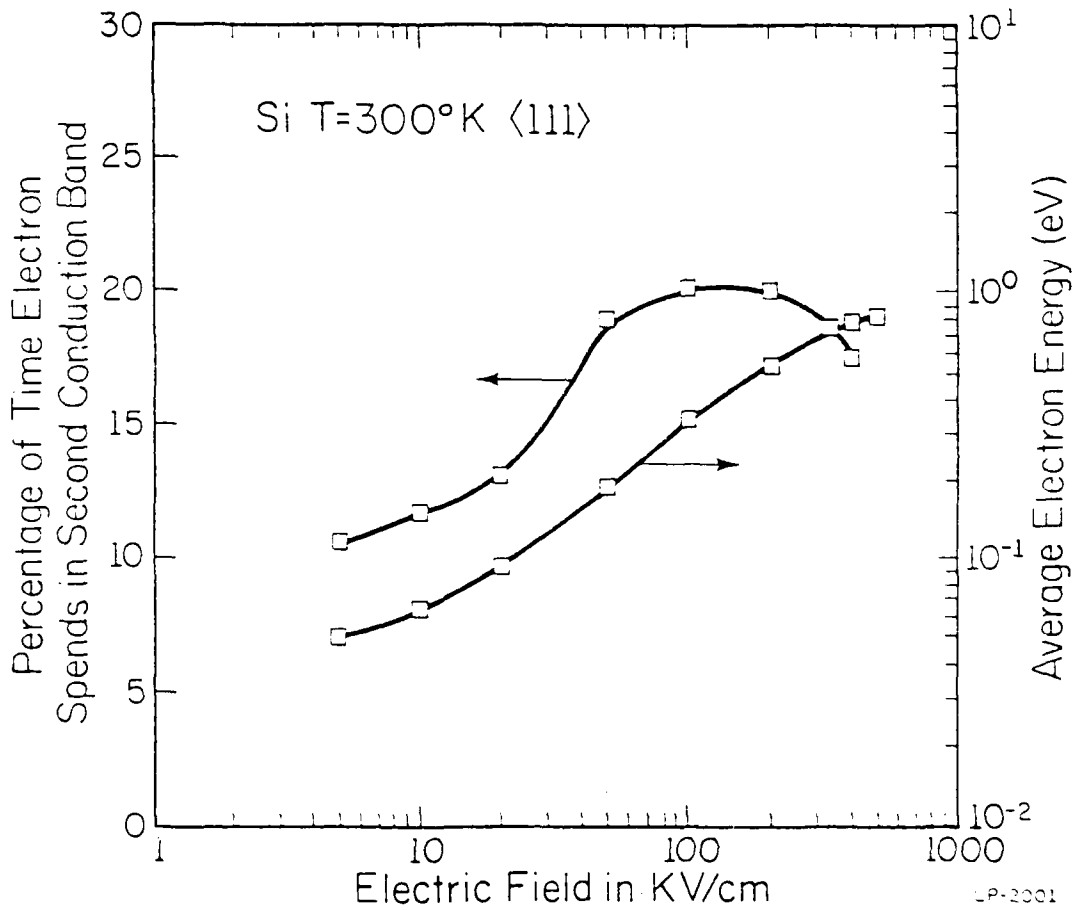
Figure 4.8: The second band effect and the average energy of electrons plotted as a function of the electric field. The left scale corresponds to the upper curve and the right scale corresponds to the lower curve.

electric field. From the pseudopotential band structure, the minima of

the second conduction band are located exactly at X. They are about

0.1 eV above the minima of the first conduction band. The electrons can

be scattered to the second band once their energies get above 0.1 eV.

The correlation between the second band effect and the average electron

energy shows clearly in Figure 4.8. The decrease of the effect of the

second band after 100 kV/cm is probably because of the slower relative

increase of the density of states of the second band compared to the

first band. Previous Monte Carlo calculations by the Italian group [18,

62] produced a drift velocity consistently higher than the experimental

values. We believe the reason for this lies in the neglect of the second

band, which enhances the scattering rate of electrons for energies above

0.1 eV. The scattering percentage due to X to L scattering, as seen from

our simulation, is significant only when the electric field is above 100

kV/cm. The drift velocity for electric fields under 100 kV/cm is basically

not influenced by adjusting the X to L coupling constant. The impact

ionization rate is very sensitive to this coupling constant because the

X to L scattering is significant when the electric field is above 200 kV/cm.

For an assumed isotropic threshold energy in Si of 1.8 eV [60], a coupling

constant of 3×10^{5} eV cm is obtained by fitting the experimental data

at 333 kV/cm.

This seems to suggest that one can adjust the X to L coupling con-

stant and the scattering probability of impact ionization to fit to the

experimental results. Indeed, this is the case. We show in the next

section that three sets of parameters have been found for a good fit to

the experimental results.

4.4 Comparison and Discussion of High Field Transport Parameters

As mentioned in the last section, one can adjust the X to L coupling constant and the impact ionization scattering rate to fit the experimental data. In Figure 4.9, we show the scattering rates as a function of energy for three different sets of parameters which all fit the experimental results within the error of the calculations. The scattering rate below 1 eV, which is important in determining the low field drift velocity (<100 kV/cm), stays the same for the three cases. In other words, the low field transport behavior for the three sets of parameters are the same. The parameters of Set 1 are those used in Section 4.3 with $D_{XL} = 3 \times 10^8$ eV/cm, P = 100, and $E_{th} = 1.8$ eV. The parameters of Set 3 are based on $D_{XL} = 1 \times 10^8$ eV/cm and Kane's impact ionization scattering rate [55]. The parameters of Set 2 lie somewhat in between the two sets of parameters and are $D_{XL} = 2 \times 10^8$ eV/cm, P = 0.01 and $E_{th} = 1.1$ eV for Keldysh's formula. Figure 4.10 shows the impact ionization scattering rate for the three cases. Note that for P = 100, the ionization scattering rate shoots up almost abruptly to very high values and dominates over the phonon scattering rate. For Sets 2 and 3, the ionization scattering rates are more moderate and phonon scatterings remain dominant up to very high energies (about 2.5 eV). In Figure 4.11, we show the electron ionization coefficient plotted against the inverse field strength for the three sets of parameters. Within the standard deviation of the calculations, they all lie in the range of the experimental results. It is surprising that all three sets of parameters fit to the experimental results in spite of the fact that the behavior of

64
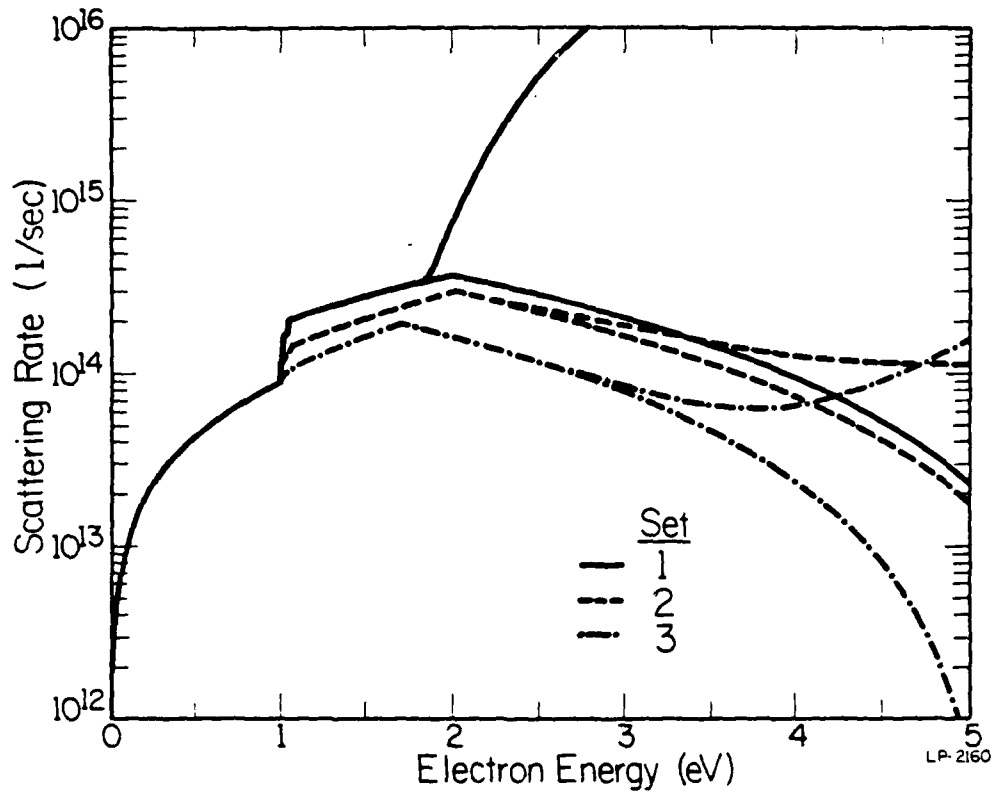
Figure 4.9: The total scattering rates corresponding to the three sets of transport parameters described in the text plotted as a function of energy. The upper curve for each set at high energies corresponds to the impact ionization scattering rate.
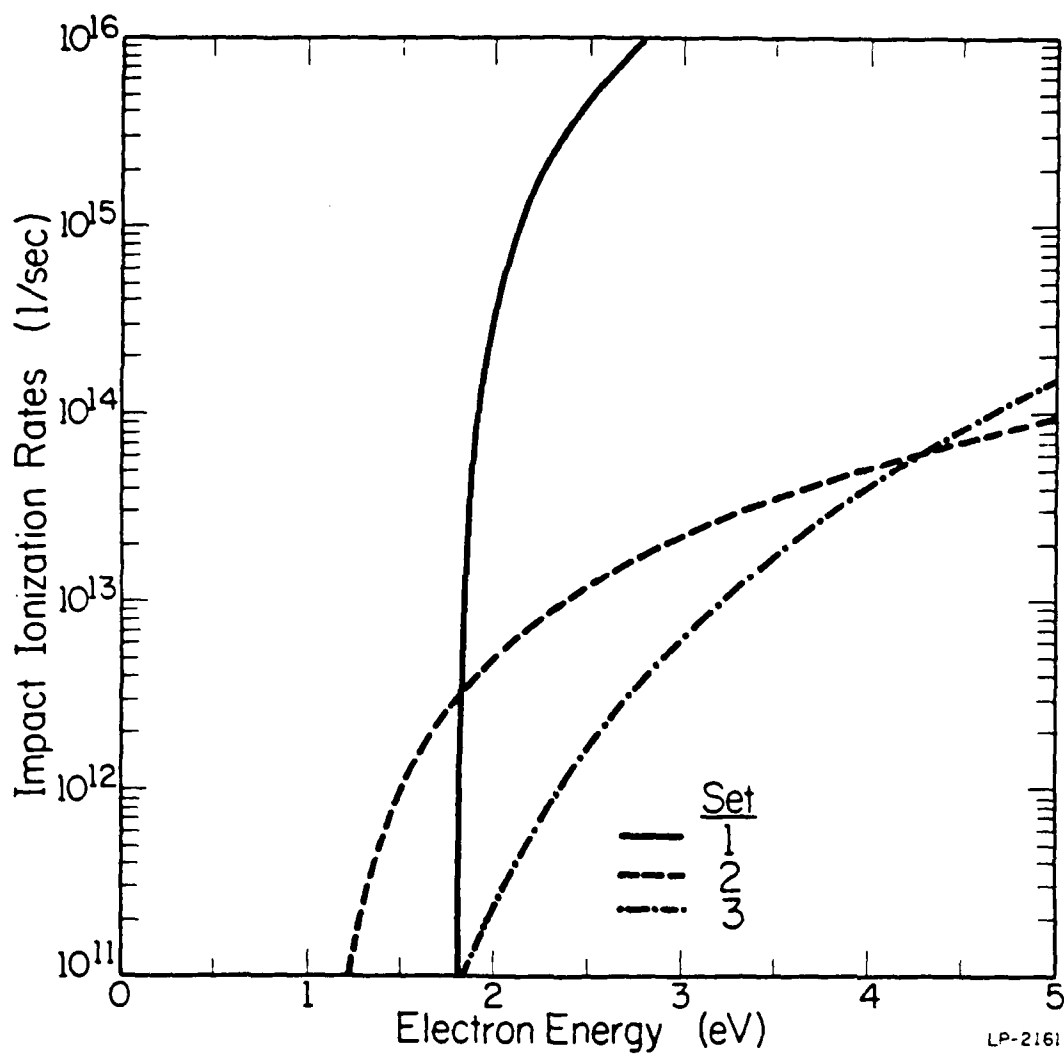
Figure 4.10: Impact ionization scattering rates for the three sets of transport parameters plotted as a function of energy.
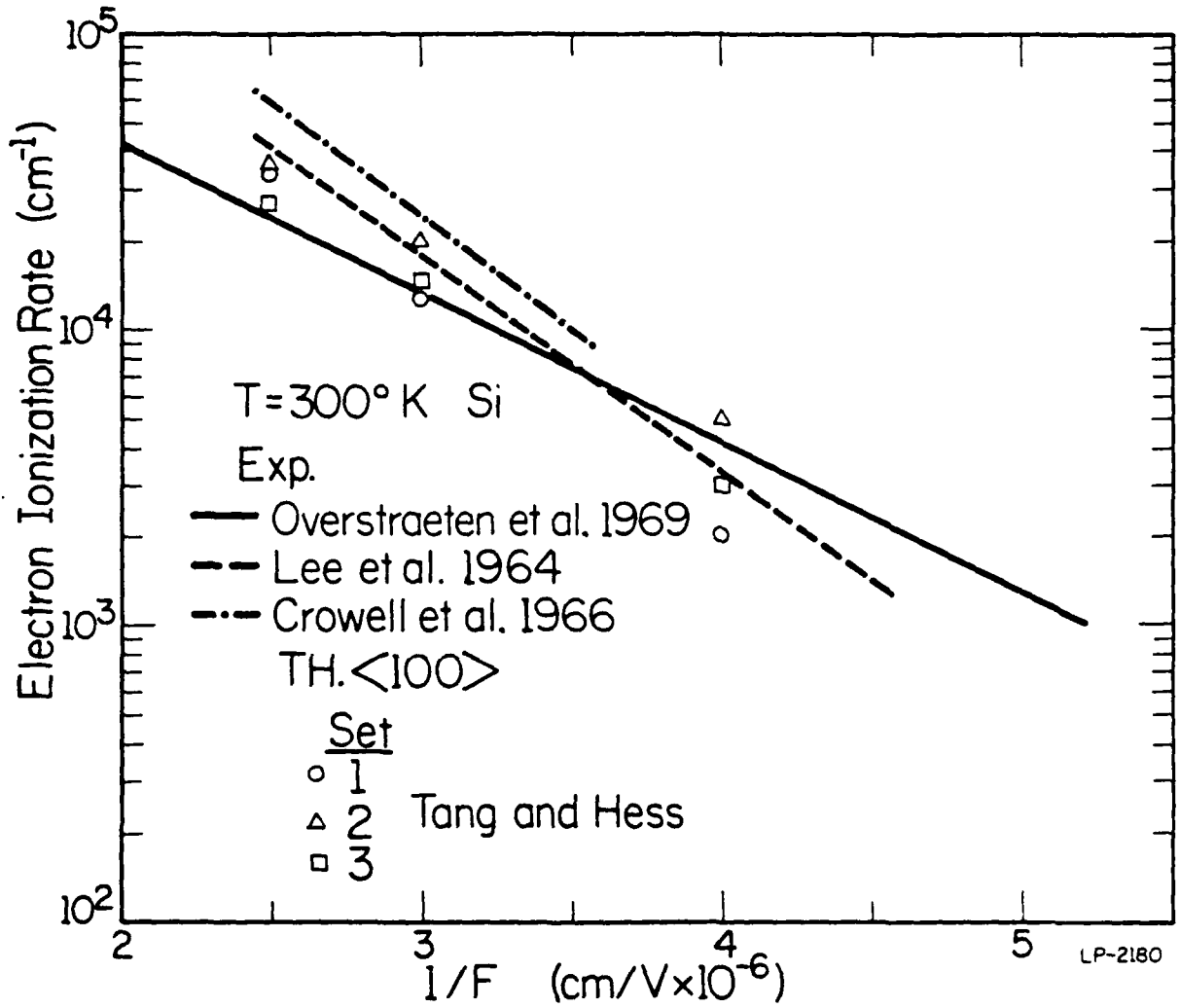
Figure 4.11: Electron ionization rate plotted against the inverse field strength for the three sets of transport parameters.

the electrons is quite different. In the situation for Set 1 parameters, which is the one that has been used for all previous impact ionization theories, the electrons that gain energy above the ionization threshold impact ionize almost immediately. The effective threshold energy is only a little higher than the threshold energy. For the other two sets with threshold energy equaling the band gap of 1.1 eV, the electron does not impact ionize immediately after its energy exceeds the threshold. The phonon scatterings and impact ionization are then competing and the effective threshold becomes a strong function of the electric field as shown in Figure 4.12. In the case of Kane's ionization rate, the effective threshold can be as high as 3.3 eV for a field strength of 400 kV/cm.

The calculated drift velocities corresponding to Figure 4.11 are shown in Figure 4.13. Notice that the lower the high energy scattering rate, the higher the high field drift velocities. The reason for this trend can be explained as follows. Intervalley scatterings are randomizing and, hence, randomize the forward momenta of the electrons. The magnitude of the average forward momentum in the field direction is directly proportional to the drift velocity. Therefore, the less the randomizing scattering, the higher the drift velocities. However, this argument is only partially true because the mass of the electron is a strong function of energy. But the subtleties are seen when reexamining Figure 4.11.

There is no obvious trend for the three sets of results shown in Figure 4.11. In fact, there is a subtle balance between the phonon
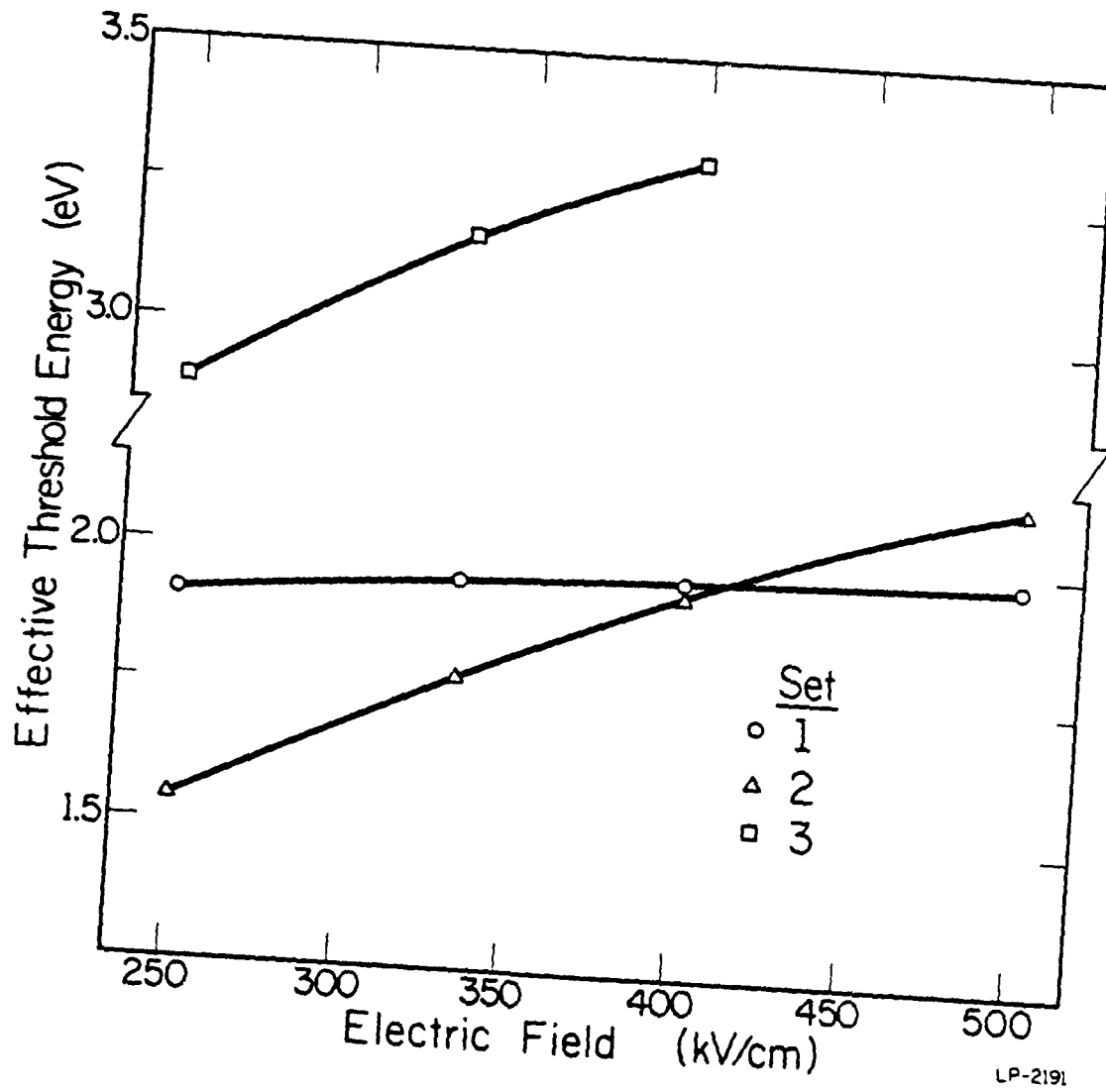
Figure 4.12: The effective threshold energy of impact ionization plotted against the electric field for the three sets of transport parameters.
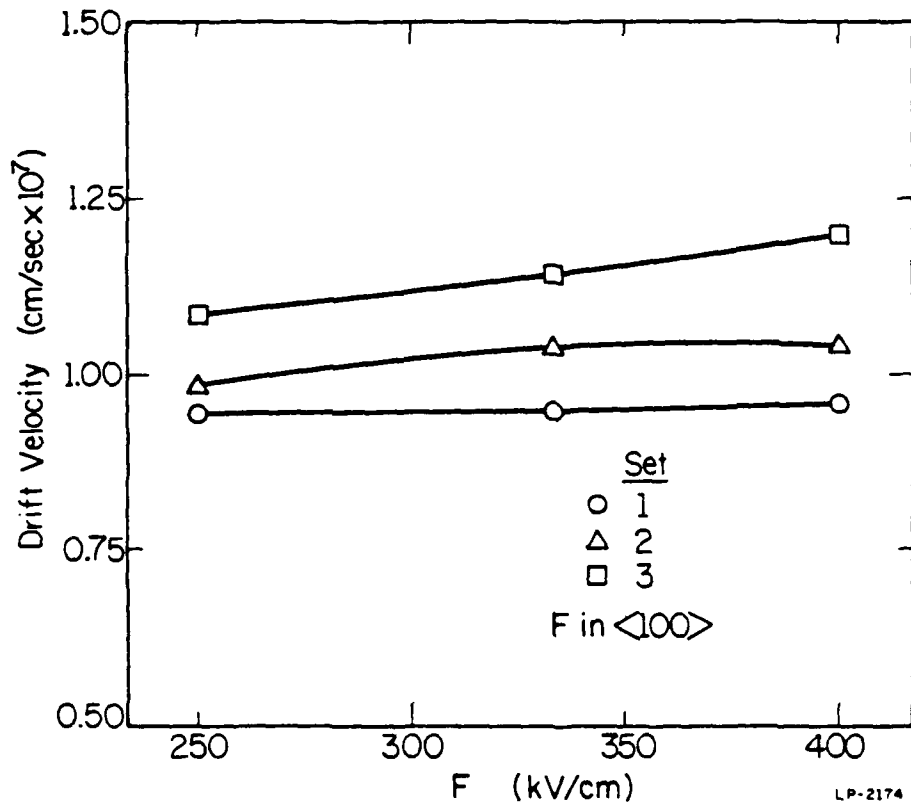
Figure 4.13: High field drift velocities for the three sets of transport parameters plotted against the electric field.

scattering process and the impact ionization process. In order to
really understand the details, one has to resort to the distribution
function.

The strength of the total scattering rate (including the phonon
scattering process and the impact ionization process) determines how much
the distribution function is "heated up". As shown in Figure 4.14, the
lower the total scattering rate, the higher the electron temperature as
defined by Equation 2.10. In other words, there are more electrons with
high energies if the total scattering rate is lower. But the larger num-
ber of electrons in the high energy tail of the distribution function does
not imply a larger ionization coefficient because there are two scattering
processes, i.e., phonon scattering and impact ionization scattering, compet-
ing with each other.

Figure 4.15 shows the total energy dissipation rates and the impact
ionization dissipation rates for the three cases. One might expect that
the high ionization rate results in a high impact ionization dissipation
rate. It would seem that the faster (in time) the electrons impact ionize,
the higher the dissipation rate. But Figure 4.15 shows just the opposite.
It is simply because the total rate of an event happening is given by the
product of the number of particles available for the event and the in-
dividual rate for the given event. From Figure 4.14, we see that Set 3
gives the highest electron temperature, which implies a larger number of
electrons in the high energy tail, and hence the highest dissipation rate
as shown in Figure 4.14, although its total scattering rate is the lowest.

How can we distinguish among the three sets of high field trans-
port parameters, which all agree well enough with the experiments? As
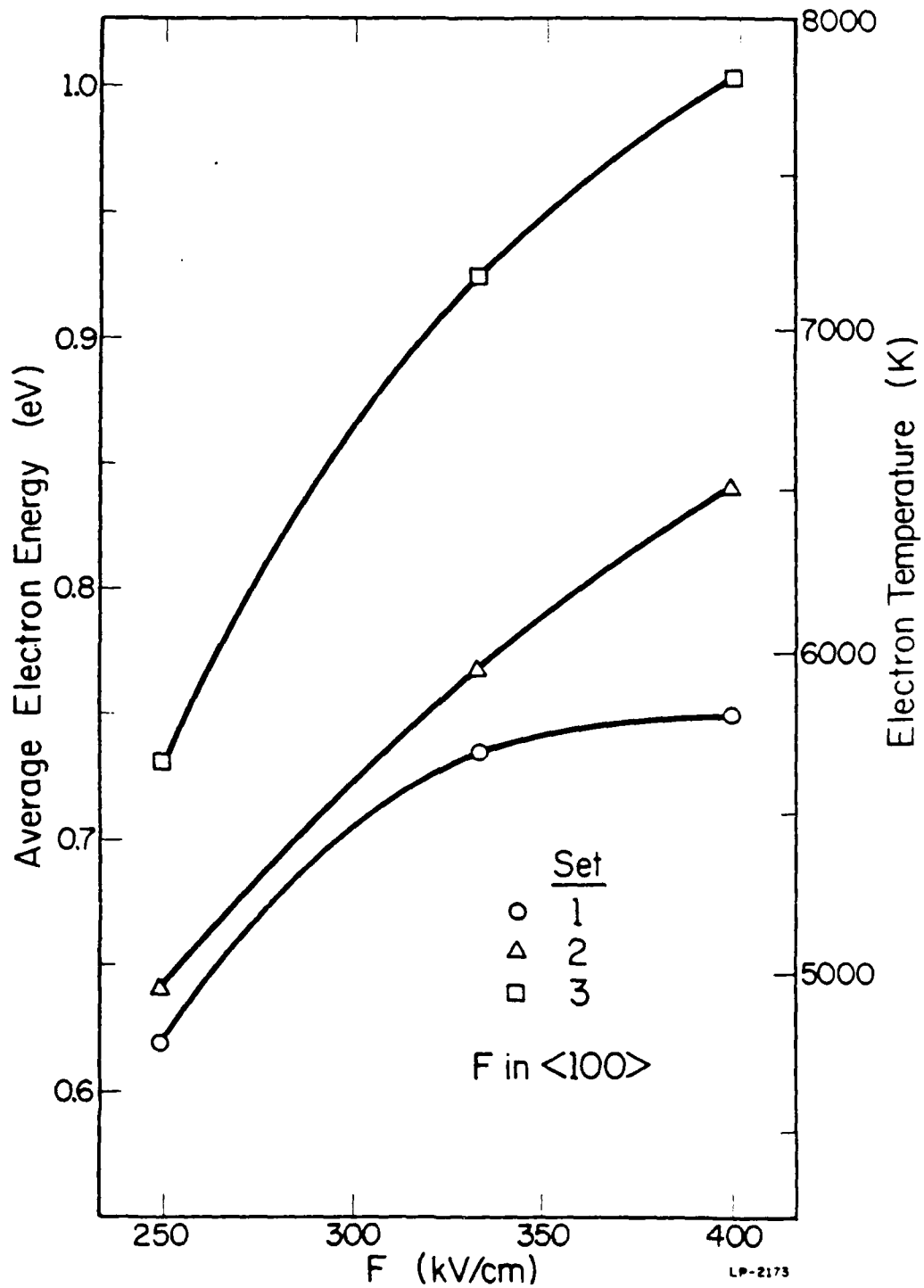
Figure 4.14: The average electron energy as a function of the electric field. The right scale is the corresponding electron temperatu. .
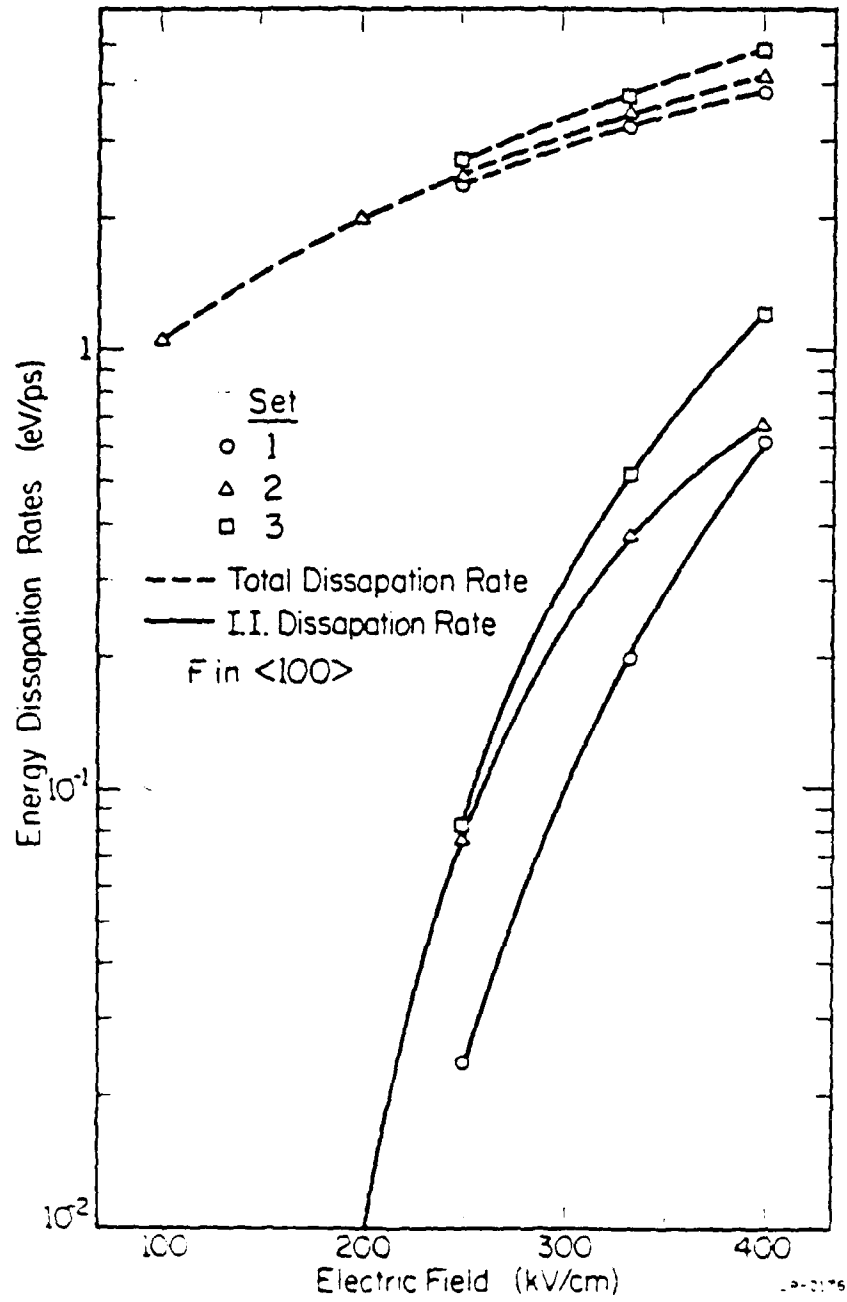
Figure 4.15: The total energy dissipation rate and the impact ionization dissipation rate plotted against the electric field for the three sets of transport parameters.

shown in Figure 4.14, the electron temperature, which is a measure of the energy distribution (although it does not necessarily imply a Maxwellian form), is very different for the three cases. Therefore, if one can measure the distribution function at high energies by some experimental means, one should be able to determine the right set of parameters.

In previous theories of impact ionization [49, 54], the ionization cross sections were all assumed to be abruptly rising above the threshold energy. As clearly shown in Figure 4.9, this is not necessarily the case. We describe in the next chapter how Ning's experiment measures the high energy tail of the distribution function and how we simulate the experiment by a Monte Carlo method. It turns out that Set 2 of the parameters describes the high energy tail of the distribution function correctly and the previous assessments of impact ionization increasing rapidly above a threshold of $1.5E_g$ [56] seems to be in error.

CHAPTER 5

STUDY OF ELECTRON EMISSION INTO SILICON DIOXIDE

5.1 Introduction

The Si/SiO$_2$ system has been studied extensively because of its important role in silicon device technology. One of the most intriguing hot carrier transport phenomena in this structure has been the emission of hot electrons or holes into the SiO$_2$ layer. This phenomenon is, on the one hand, an unwelcome effect causing threshold shifts, breakdown walkout and hence device instability [63-65]; but on the other hand, it has found application in electrically programmable memory devices [66]. In order to understand the emission process, various experiments have been constructed to study this problem [67-75]. Among the many attempts, Ning's experimental setup has been the most interesting one. He was able to measure the absolute emission probability of optically induced injection electrons coming from the substrate toward the Si-SiO$_2$ interface. In another sense, he was able to probe the high energy tail of the distribution function, which is extremely important in determining the high field transport parameters.

Past models explaining the emission process involved simplifying assumptions, for example, an energy independent scattering mean free path and a parabolic band structure. As discussed in Section 4.2, the band structure is highly nonparabolic at high energies. Such high energy transport has to consider different valley types (X,L) and more than one

conduction band. Moreover, impact ionization definitely plays an important role. Since Ning's experiments involved low current injection, they are best suited for a band structure dependent Monte Carlo study.

This chapter is devoted to the theoretical explaining of Ning's experiment with two purposes in mind: To understand the physics behind the emission process and to determine the right set of high field transport parameters to probe farther up into the band. In Section 5.2, a summary of Ning's experimental procedure is given. In Section 5.3, we discuss the Monte Carlo method for the simulation. In Section 5.4, the results and discussion are given. In Section 5.5, we present our conclusion.

5.2 Summary of Ning's Experiments

The devices used in Ning's experiment were n-channel polysilicon-SiO_2-Si field-effect transistors. Use has been made of the optically induced hot-electron injection [69] as illustrated in Figures 5.1a and b. In this method, source and drain were grounded, a negative bias was applied to the substrate, and a positive bias was applied to the gate. The advantage of this setup is that the gate voltage and the substrate voltage can be independently adjusted and are not affected by each other since the interface is pinned to the ground potential. Electron-hold pairs were generated in the substrate by incident photons. Electrons which diffused into the depletion region are accelerated toward the $Si-SiO_2$ interface. The majority of carriers that do not overcome the interface barrier are collected as the source and the drain currents. The carriers that overcome the barrier are collected as the gate current assuming that they have not

Light

I_G

I_D

I_S

V_{SUB}

(a)

Light

eV_{SUB}

eV_G

SiO_2

P-Substrate

Polysilicon
Gate

(b)
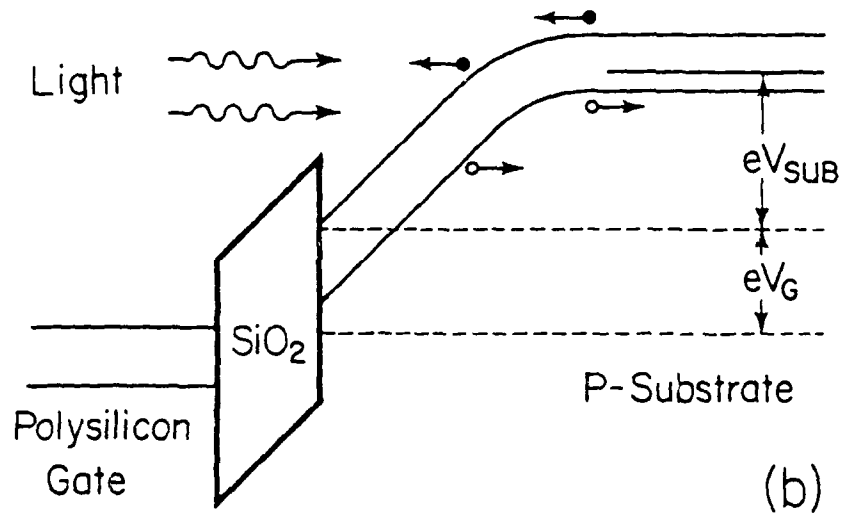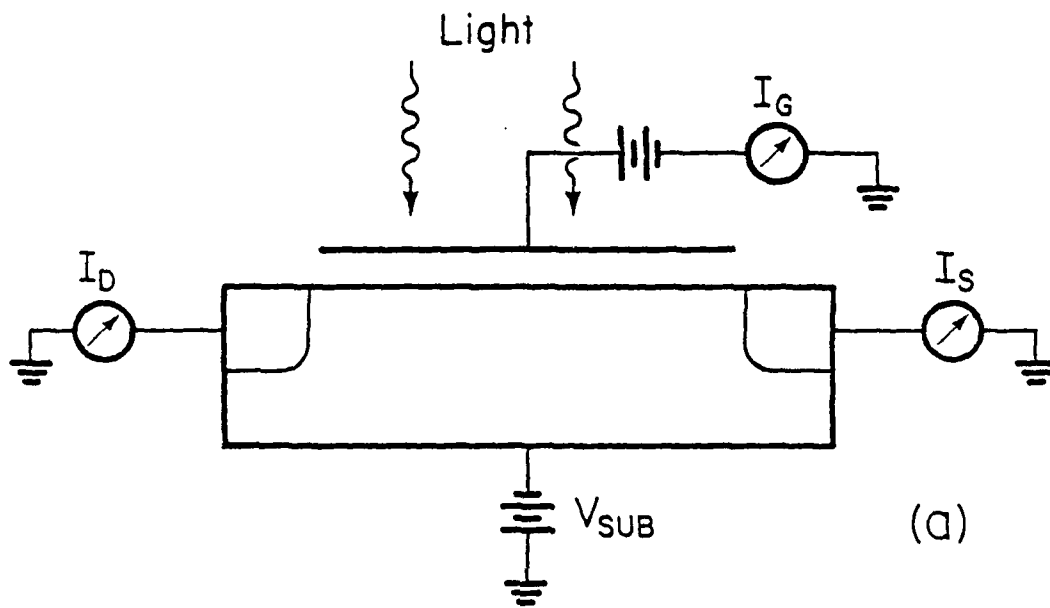
LP-2186

Figure 5.1: Experimental setup measuring the emission
probability.

been trapped in the silicon dioxide layer. By measuring the gate, source and drain currents, the absolute emission probability could be determined by

$$P = \frac{I_G}{I_{total}} \approx \frac{I_G}{2I_D} \ , \tag{5.1}$$

where I_{total} was the total current coming from the substrate and was approximately twice the drain current, since the gate current is orders of magnitude smaller than the drain current, and the source and the drain currents were equal by the symmetry of the device.

The doping profile in the silicon substrate can be represented by a Gaussian of the form

$$N_A(x) = N_B + C_0 \exp(-\frac{x^2}{2\sigma^2}) \ , \tag{5.2}$$

where x is the distance from the Si-SiO$_2$ interface, N_B is the background doping concentration, C_0 is the surface concentration due to boron implantation, and σ is the characteristic of the penetration of C_0. The solution to the Poisson equation for this doping profile is derived in detail in the appendix of Reference 73.

Figures 5.2a and b show the potential profiles and the electric field profiles in the depletion region for two substrate voltages with $N_B = 7.5 \times 10^{15}$ cm^{-3}, $C_0 = 1.13 \times 10^{16}$ cm^{-3}, and $\sigma = 3.36 \times 10^{-5}$ cm (device 15-2-9 in Ning's experiment). Notice that the potential profiles are strong functions of the spatial coordinates and hence the electric fields are highly nonuniform. This has made it too difficult to approach the problem by solving the Boltzmann equation directly [68, 75].
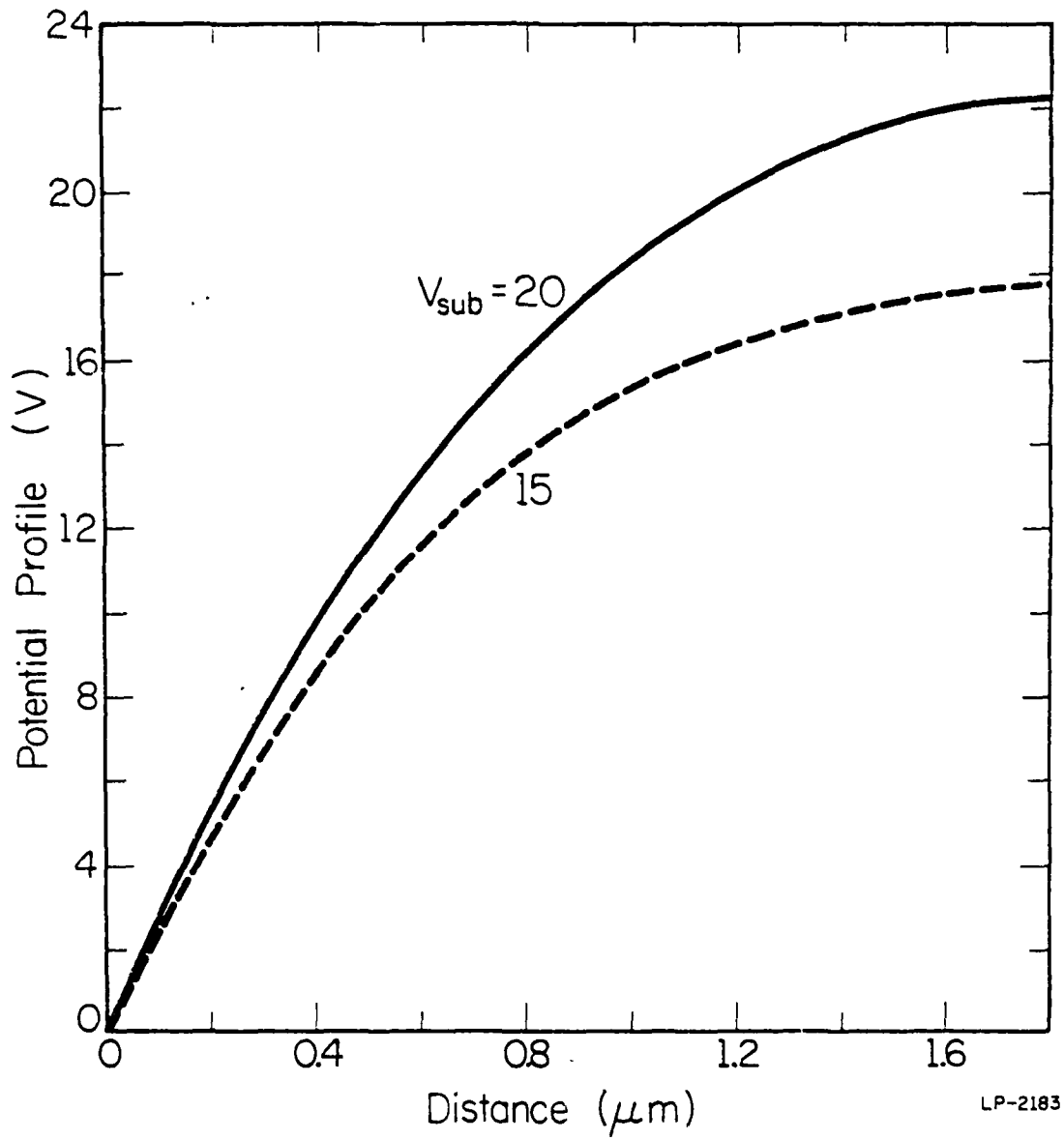
Figure 5.2(a):   Potential profiles in the depletion region
   for device 15-2-9.
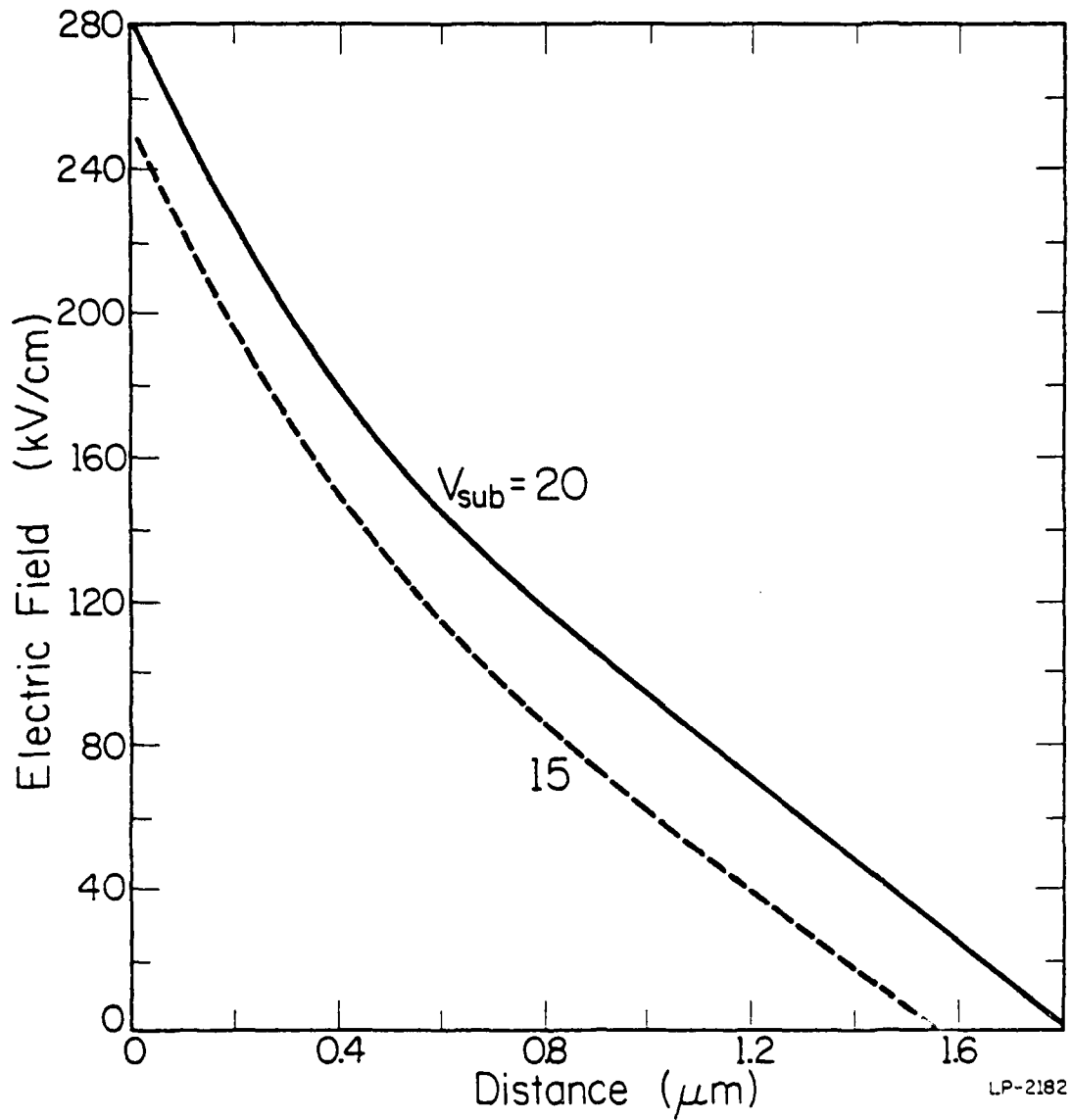
Figure 5.2(b): Electric field profiles in the depletion
region for device 15-2-9.

The luck, electron model proposed by Ning et al. to explain the
emission process is depicted in Figure 5.3. The concept of a "lucky
electron" was conceived by Shockley in treating the impact ionization
problem [50]. Electrons located a distance d away from the interface
having a potential energy equal to the emission barrier will overcome the
barrier and go into the silicon dioxide layer if they encounter no
scatterings at all. For an assumed constant scattering mean free path λ,
the probability for lucky electrons can be expressed as

$$P = A \exp(-\frac{d}{\lambda}), \tag{5.3}$$

where A is a normalization constant. This expression can be derived
the same way as we derived the time of free flight in the Monte Carlo
simulation (Appendix 1).

The barrier lowering effect, which is also shown in Figure 5.3,
is due to Schottky lowering and effective tunneling lowering. According
to Ning, the barrier height can be written in the form

$$\phi_B = 3.1 \text{ eV} - b \ F_{ox}^{1/2} - a \ F_{ox}^{2/3}, \tag{5.4}$$

where 3.1 eV is the $Si-SiO_2$ interface barrier [76], F_{ox} is the oxide
field. The second term is responsible for Schottky lowering. The third
term is responsible for tunneling. A and b have been determined by com-
parison with the experimental results. From fits to the experimental
data, a and b were found to be $1 \times 10^{-5} \ e(cm^2 \ V)^{1/3}$ and 2.59×10^{-4}
$e(cm \ V)^{1/2}$ respectively. We plot in Figure 5.4 the barrier heights against
the oxide fields for two cases: tunneling lowering effect included and
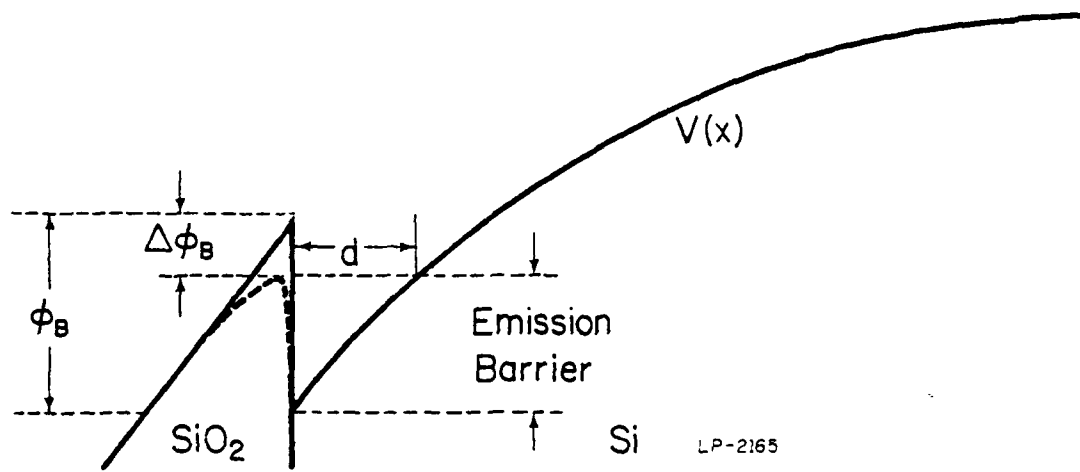
Figure 5.3: The band diagram for the Si-SiO$_2$ structure.
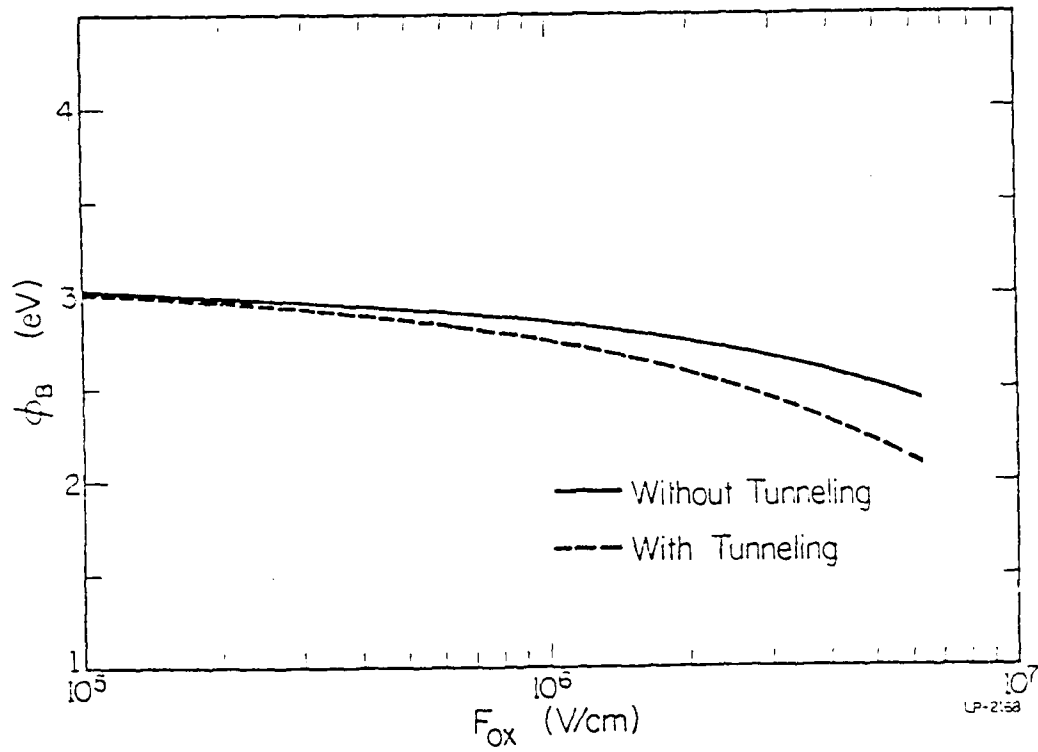
Figure 5.4: Effective barrier height plotted against the oxide
field strength. The solid line is without
tunneling and the dashed line is with tunneling.

tunneling lowering effect not included. As the oxide field increases, the barrier height gets lowered by substantial amounts as shown in the figure.

Surprisingly, with the simple lucky electron model, Ning was able to fit his experimental results well for all the different devices with a consistent set of parameters. For temperatures at 300 K and 77 K, the parameters are A = 2.9, λ = 91 Å, and A = 4.3, λ = 108 Å respectively. We discuss in the following sections our method of approach and look at this complicated problem in more detail.

5.3 Method of Approach

As discussed in the last section, this is a transport problem involving highly nonuniform spatial electric fields. The electric field is not only determined by the static space charge but also from the current density. In order to take both factors into account, a complicated self-consistent calculation, as discussed in Chapter 3, is required. Fortunately, under the low level current condition, which was the case for the experiments, the contribution of the current is negligible. For a typical source current of about 5×10^{-5} amperes and a gate area of 5×10^{-4} cm^2 taken from the experiments, one finds a carrier concentration of about 6×10^{10} cm^{-3} if a saturation drift velocity of 1×10^{7} cm/sec is assumed. We see that the carrier concentration is orders of magnitude below the doping concentration and hence its contribution is totally unimportant. Therefore, we need only to include the spatial variation of the electric field due to the static charge. The Monte Carlo approach, including the nonuniform electric field, has been discussed in detail in Section 2.4.

The total current coming from the substrate has two components: the drift component due to carriers generated in the depletion region, and the diffusion component due to the carriers generated in the bulk neutral region and diffusing into the depletion region. Notice that this is a situation similar to that of a p-i-n photodiode, as derived in Sze's book [77]. The drift and diffusion component are expressed as

$$J_{drift} = -e\phi_0[1-\exp(-\alpha x_m)] \tag{5.5}$$

and

$$J_{diff} = e\phi_0 \alpha L_n \exp(-\alpha x_m)/(1+\alpha L_n) \tag{5.6}$$

where ϕ_0 is the incident photon flux, x_m is the depletion layer width, L_n is the electron diffusion length and α is the absorption coefficient. As argued by Ning, for typical values of L_n between 0.02 and 0.2 cm (which corresponds to minority-carrier lifetimes of between 10^{-5} and 10^{-3} sec), depletion layer widths x_m less than 10^{-4} cm for devices used, and values of α between 10^2 and 10^3 cm^{-1} for photons of energy near the band-gap, one finds that $L_n > 1$ and $x_m \ll 1$. From Equations 5.4 and 5.5, the optically generated current was completely dominated by the diffusion component and should be approximately independent of the depletion-layer width. This means that we can start electrons from near the depletion layer edge to simulate the diffusing-in component coming from the bulk neutral region without considering the optically generated carriers inside the depletion region. Following the trajectories of these diffusing-in electrons with a Monte Carlo simulation, one should be able to determine

the emission probability by examining the percentage of electrons with energies greater than the barrier height reaching the interface. Unfortunately, this straightforward idea is too CPU time intensive because of the extremely low emission probabilities (10^{-5} to 10^{-10}). For an emission probability of 10^{-5}, one has to simulate a number much greater than 10^5 in order to get a reasonable probability within an acceptable statistical fluctuation.

To avoid such difficulties, we separate our simulation into two parts, as illustrated in Figure 5.5. In the first simulation, as specified by "1" in the figure, we start electrons with a distribution in quasi equilibrium with the local field at a position where the potential energy is about twice the barrier height. This initial distribution is automatically generated by letting the electrons scatter a few times under the local field strength before launching them. Actually, the electrons get scattered very often along the path and lose their memories of the past after a few scatterings. Consequently, if we start the electrons far enough from the interface, it does not matter too much how we start the initial distribution. Following the trajectories of the electrons one by one, the energy distribution of the ensemble is collected at position "2" specified in Figure 5.5. We then start a second simulation for the electrons in the high energy tail of distribution "2" only. and collect the energy distribution of these electrons at the interface. Notice that impact ionizations occur alon the way, especially in the region close to the interface where the electric fields are high. By calculating the percentage of electrons in the high energy tails as
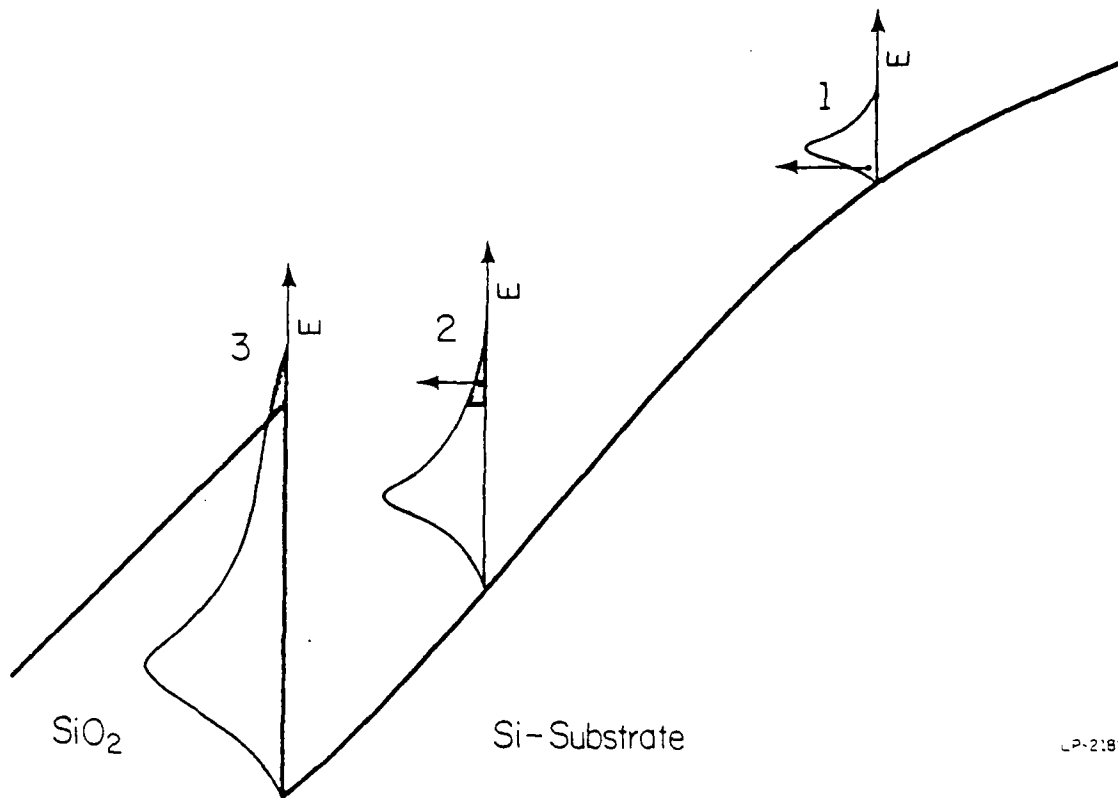
Figure 5.5:   Schematic diagram for the Monte Carlo simulation.

illustrated by the shaded regions in "2" and "3" of Figure 5.5, one is then able to calculate the emission probability as follows.

If we start a total number of N_1 electrons in the first simulation, with n_1 electrons arriving in the high energy tail of "2" and m_1 impact ionization events along the way, the probability of finding an electron in the high energy tail of "2" can be written as

$$P_1 = \frac{n_1}{m_1 + N_1} \; . \tag{5.7}$$

The m_1 in the denominator is crucial because impact ionization also contributes to the experimentally measured total current. The same argument applies to the second simulation, and the probability of finding electrons in the high energy tail of "3" can be written as

$$P_2 = \frac{n_2}{m_2 + N_2} \; , \tag{5.8}$$

where N_2 is the total number of electrons used in the starting high energy tail of "2", m_2 is the number of impact ionization events, and n_2 is the number of electrons resulting in the high energy tail of "3". Assuming that these n_2 electrons with energies greater than the effective barrier height (Schottky lowering and tunneling effect included) all overcome the barrier, the total emission probability can be expressed as

$$P = P_1 \cdot P_2 \; . \tag{5.9}$$

A large number of electrons have to be considered in both stages of the simulation in order to minimize the standard deviation. Depending

on the emission probability, an ensemble of 2000 to 4000 electrons for the first simulation and 4000 to 8000 for the second simulation is required to get an acceptable result. Mathematically, the percentage error can be expressed as

$$\frac{\Delta P}{P} = \frac{\Delta P_1}{P_1} + \frac{\Delta P_2}{P_2} = \frac{\Delta n_1}{n_1} + \frac{\Delta n_2}{n_2} = \frac{1}{n_1} + \frac{1}{n_2} \; , \tag{5.10}$$

where the number fluctuations n_1 and n_2 are taken as 1. On a Dec-20 machine, one electron takes about 15 to 30 CPU seconds in the first simulation and 5 to 10 CPU seconds in the second simulation. This results in about 14 to 28 CPU hours for one point!

The "partitioning" of the real space is not unique in our method. Care has to be exercised in choosing the boundary conditions for the two simulations. In the first simulation, one has to simulate the electrons all the way to the interface in order to get a physically correct distribution at position "2", since some electrons crossing plane "2" might come back again because of scatterings. In the second simulation, the electrons which get scattered and travel to the right side of the second plane should be properly relaunched according to their ener simulations, electrons hitting the interface with ener barrier height are traced a few more scatterings sidered to be collected by either the brass that as long as the boundary condition "partitioning" does not affect the simulation. The affect the highly ener

END

DATE
FILMED

8-84

DTIC
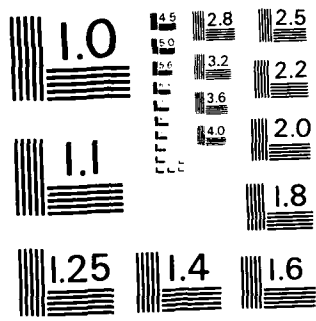
MICROCOPY RESOLUTION TEST CHART
NATIONAL BUREAU OF STANDARDS – 1963 – A

As mentioned in the introduction section of this chapter, the purpose for modeling the emission problem is twofold: to understand the physical details behind the emission process and to determine a correct set of high field transport parameters to penetrate farther up in the band. Thus, in the next section, we concentrate on studying one device in Ning's experiment which gave the highest emission probability. This was the device numbered as 15-2-9 and the potential and electric field profiles of which are plotted in Figures 5.2a and b. It is still too costly and not feasible to use the two simulation scheme to study emission processes of very low probability.

5.4 Results and Discussions

The three sets of parameters discussed in the last chapter give a very different distribution function in the high energy tail. With the emission probabilities measuring essentially the characteristics of the high energy tail of the distribution function, the first and the third sets are readily eliminated. With too high a total scattering rate, the high energy tail is totally suppressed, using the first set of parameters, and rendered the emission process impossible. With too low a total scattering rate, the third set of parameters allows too high an emission probability which is totally incompatible with the experiments. In all of the results presented in this chapter, Set 2 parameters, which are in between the two extremes (Keldysh's formalism with $P \gg 1$ and Kane's low direct calculated result), were used in the simulations.

In Figure 5.6, we show the trajectory of a typical electron coming from the substrate toward the interface. It travels along the band edge
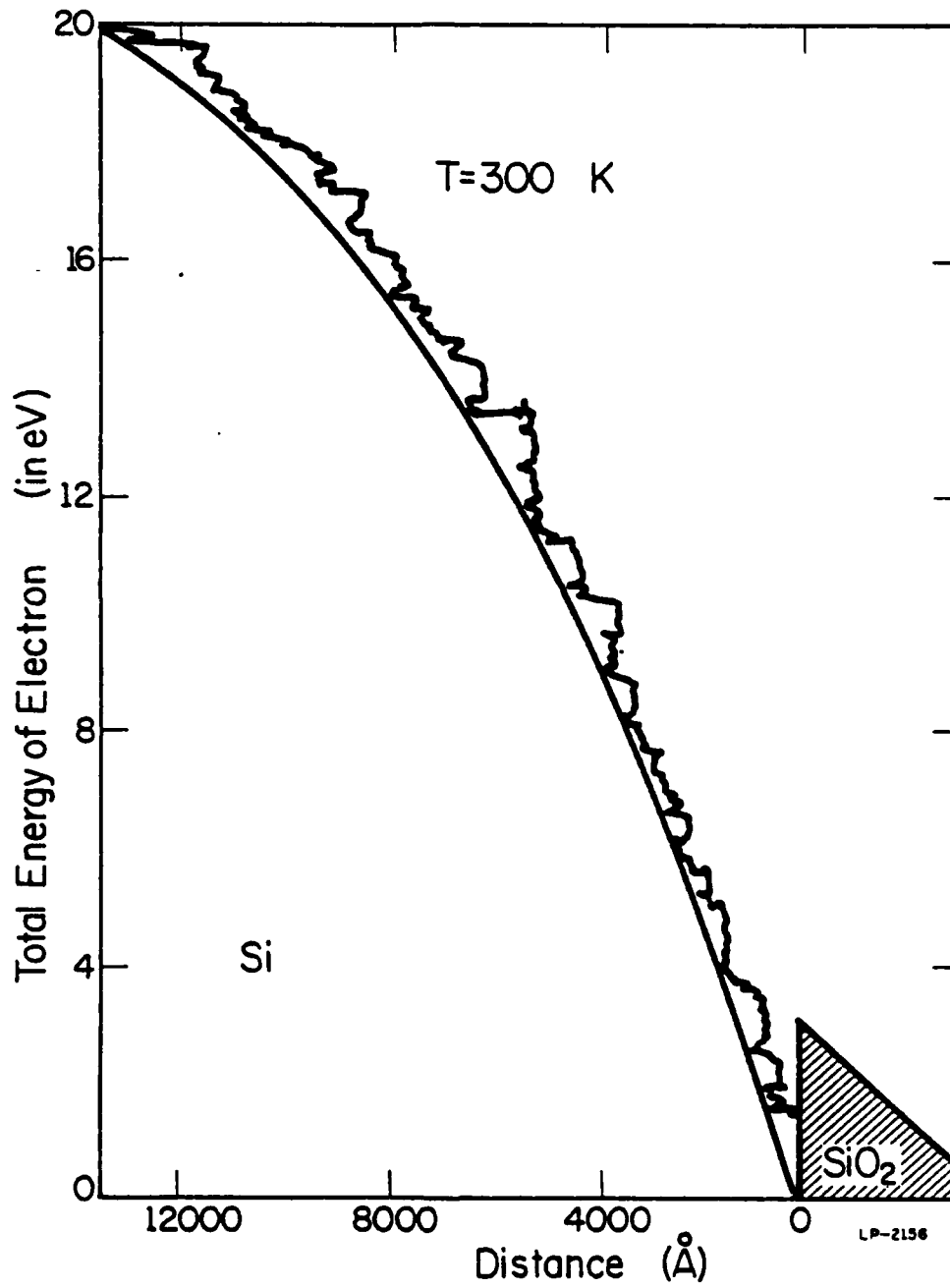
Figure 5.6:   Energy   histogram of an electron.

and encounters numerous scatterings along the way. Notice that it some-
times gets back scattered and travels against the field. Clearly, this
electron did not make it to the silicon dioxide layer. The kinetic
energy of the same electron is plotted in Figure 5.7. The slopes of the
almost vertical lines are proportional to the electric field at that
position as can be seen from the equation

$$\Delta E = e \, F \, \Delta x \, , \qquad\qquad (5.11)$$

where F is the local electric field. The electron sometimes luckily
escapes the scatterings and gains significant kinetic energy. It loses
energy from emissions of phonons, traveling against the field because of
back scatterings or suffering impact ionizations.

The calculated emission probability for device 15-2-9 is plotted
in Figure 5.8 as a function of the substrate voltage. The solid line
gives the experimental results from Ning et al. The open circles repre-
sent the emission probability of a lowered barrier height of 2.57 eV
corresponding to an oxide field of 2×10^6 V/cm as plotted in Figure 5.4.
They are lower than the experimental data. In order to fit the data,
either the barrier height must be lowered to allow more electrons to pass
through, or the total scattering rate must be suppressed to heat up the
distribution a bit more. The parameter for lowering due to the tunneling
effect has been obtained from fits to the experimental data using the
lucky electron model. However, the accuracy of such a parameter depends
entirely on how closely the model resembles the physical situation. Also,
as will be discussed in the next chapter, the collision broadening effect
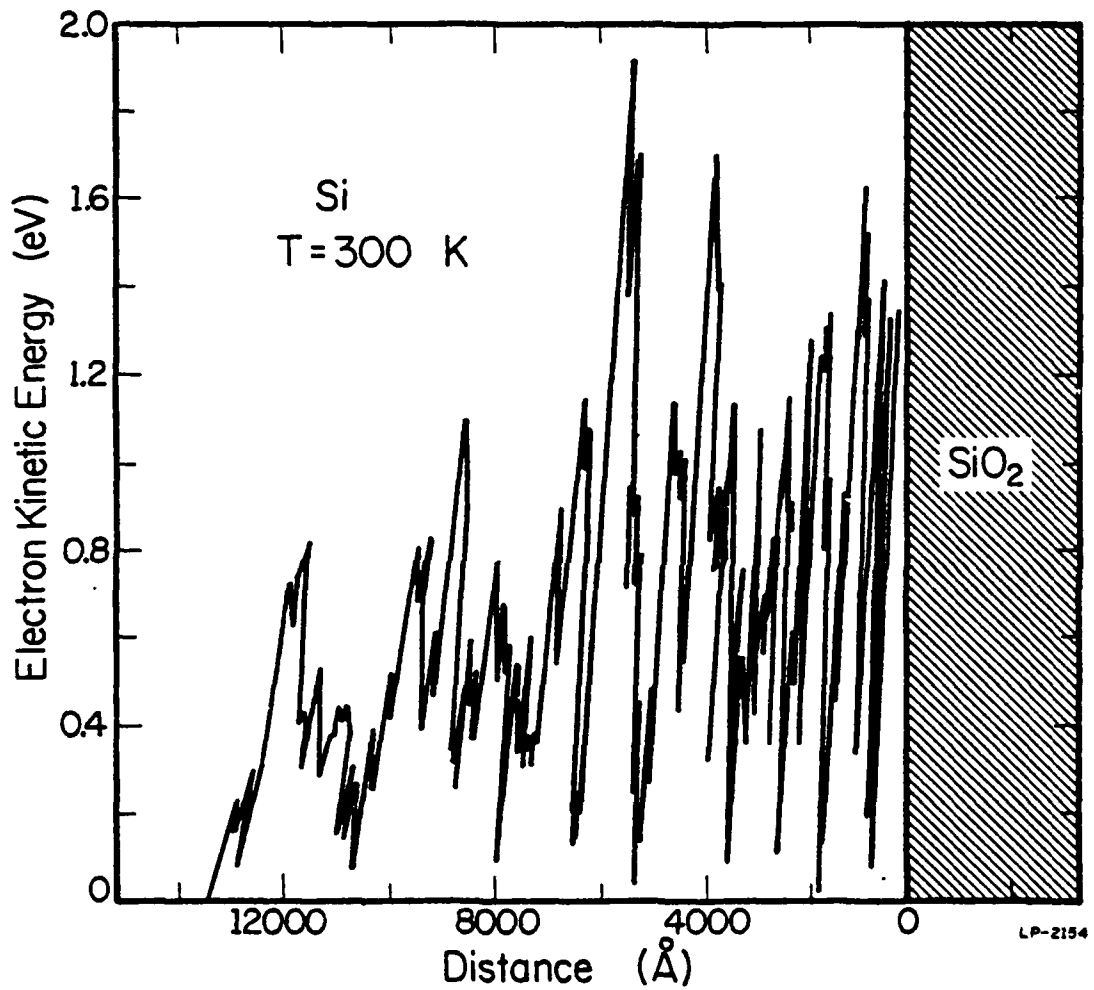
Figure 5.7: The histogram of the kinetic energy of the
same electron as in Figure 5.6.
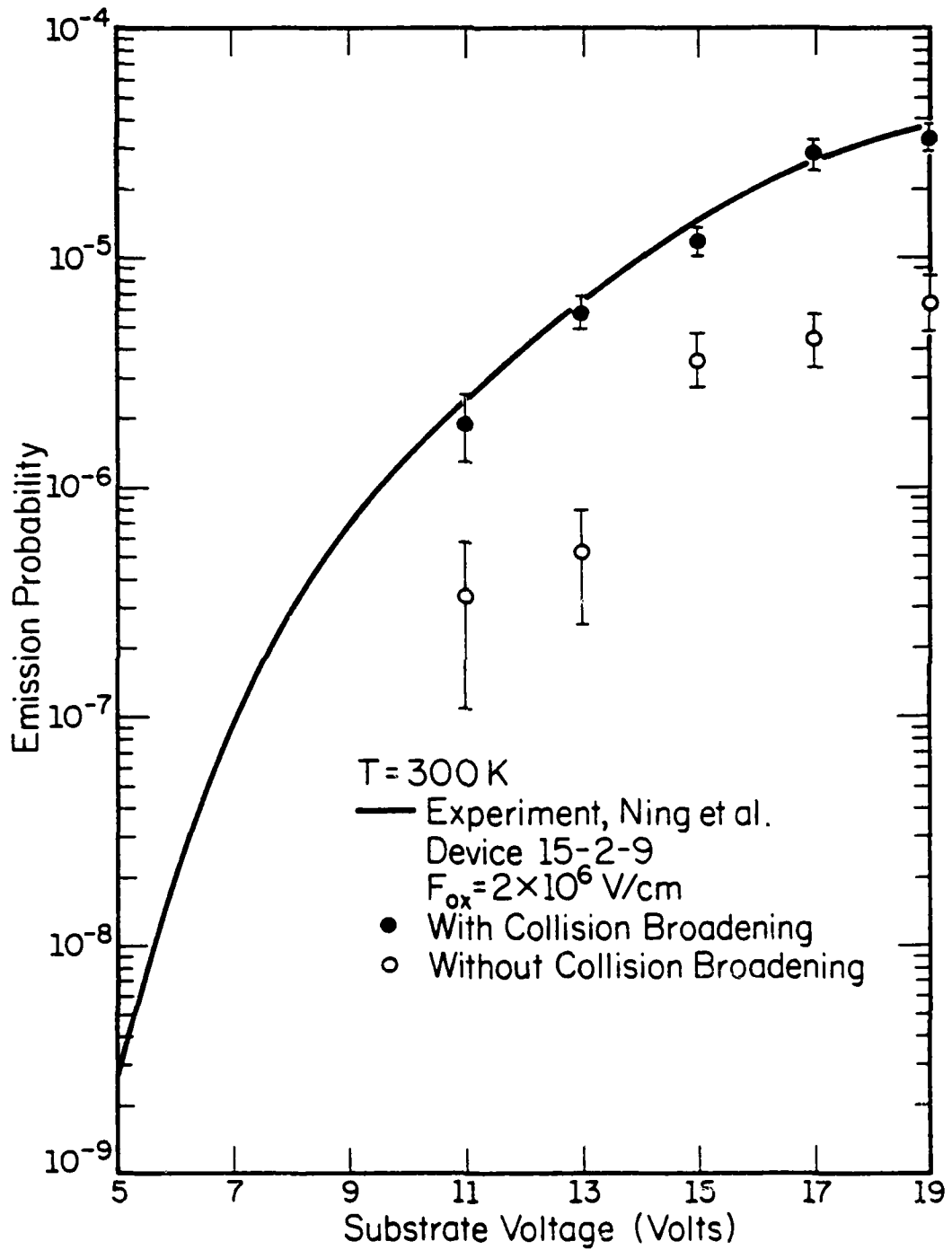
Figure 5.8: The calculated emission probability as a
function of the substrate voltage.

smears out the sharp edge of a barrier and introduces an effective

barrier lowering. If we allow an extra .07 eV lowering due to the

reasons above, we have the emission probability represented by the closed

circles in Figure 5.8. The error bars attached to the results are cal-

culated by using Equation 5.10. As discussed at the end of the last

chapter, the computing time is so costly that we cannot afford to cal-

culate emission probabilities for substrate voltages below 11 volts. But

if we extrapolate our calculated data, we see that they agree with the

experimental results.

Figure 5.9 shows the energy distributions of electrons at three

positions for the first simulation for a substrate voltage of 15 volts.

The high energy tail of the distribution extends farther up as we move

closer to the interface. In Figure 5.10, the energy distributions for

the second simulation are shown for three positions. Since electrons are

started with a high energy as illustrated in Figure 5.5, the transient

relaxation effect of the electron energy is clearly demonstrated in this

figure. As the electrons move closer to the interface, the electron

energy distribution relaxes and peaks at a lower value. In addition, the

high energy tails broaden due to the acceleration of high fields close to

the interface. About half of the electrons in the high energy tail are

in the second conduction band.

To look at the effect of impact ionization, we plot in Figure 5.11

the average ionization coefficient as a function of the surface electric

fields. The dashed line represents the steady state experimental re-

sults from Lee et al. [58] and the triangles are the calculated results
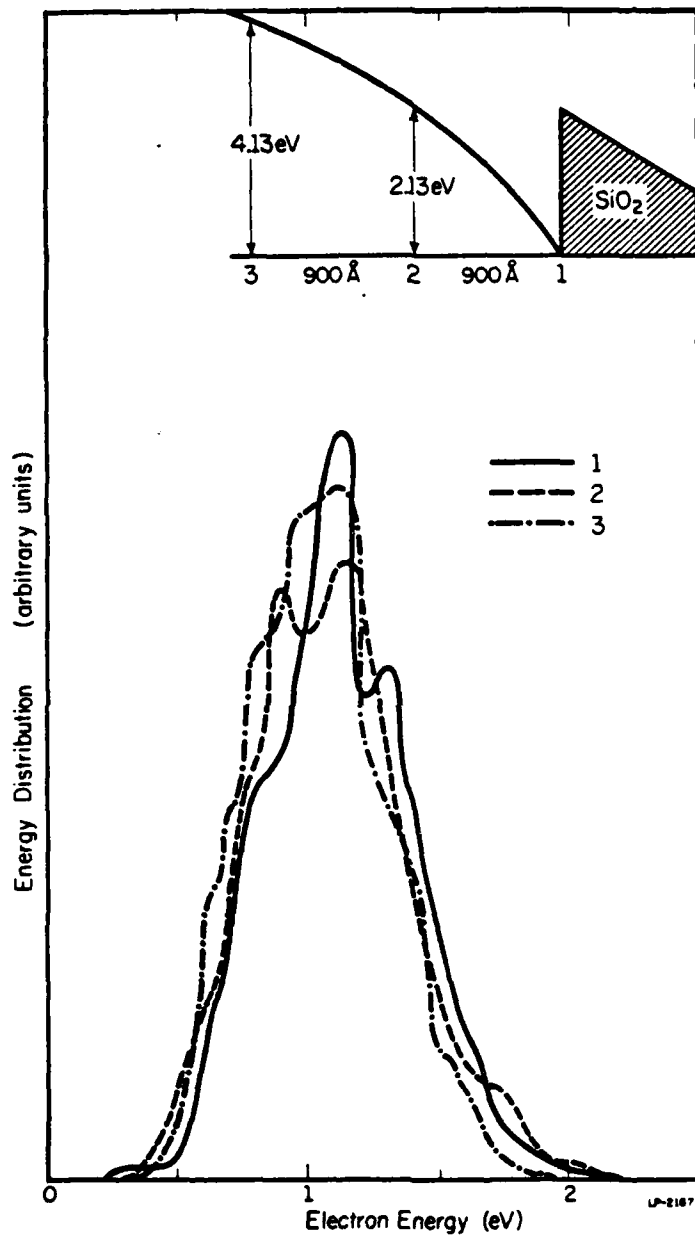
Figure 5.9: The energy distribution of electrons at three positions for the first simulation.
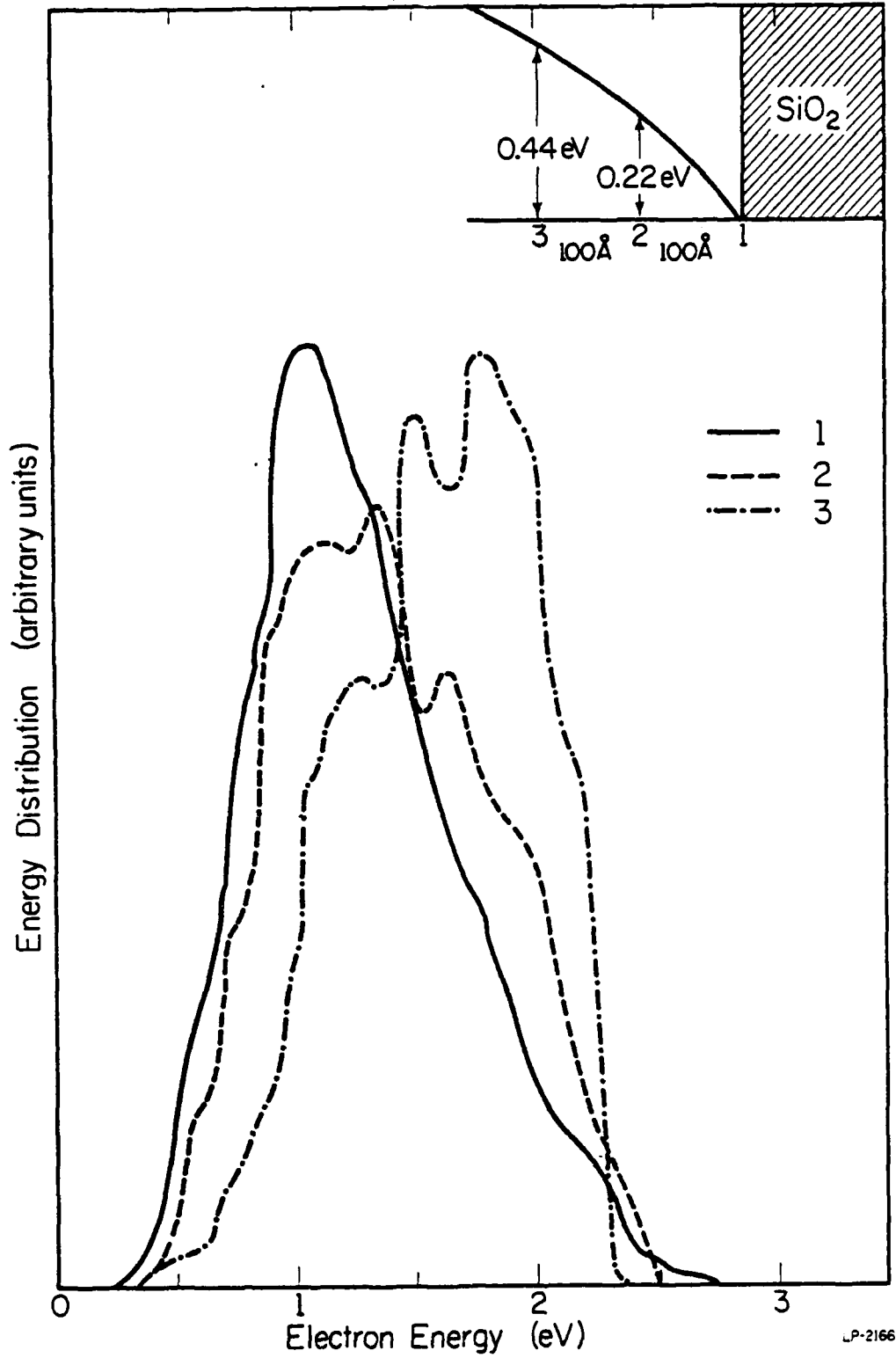
Figure 5.10: The energy distribution of electrons at three positions for the second simulation.
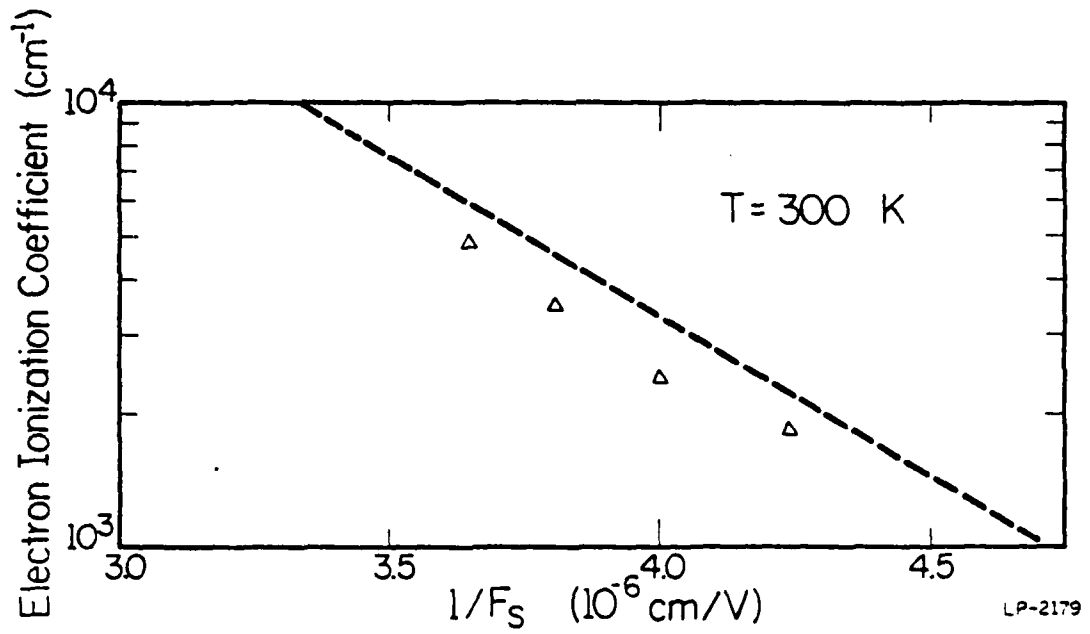
Figure 5.11: The electron ionization coefficient plotted
against the surface field.

corresponding, from left to right, to substrate voltages of 19, 17, 15, and 13 volts. The electric field is highest at the interface and decreases, rapidly moving toward the substrate. The average electric field the electrons undergo is much smaller than the maximum surface field. With the triangles lying only slightly lower than the steady state curve, it seems to suggest that the transient ionization process under an increasing field condition is enhanced. In Figure 5.12, the scattering mean free path in the field direction is plotted against the substrate voltages. We see that the scattering mean free path is not a constant but a strong function of the substrate voltage (or the electric field). They are much shorter than the constant mean free path of 91 Å used by Ning et al.

To understand this discrepancy, let us reexamine the idea of the lucky electron theory. If momentum space is considered, then the idea of the lucky electron theory is to find the probability of an electron starting from a state $\vec{k}_0$, not encountering any scattering in a time interval t, and ending up in a state $\vec{k}$ given as

$$\vec{k} = \frac{e \vec{F} t}{\hbar} + \vec{k}_0 .$$
(5.12)

The idea is conceptually simple and mathematically easily manageable. But the most important and difficult part, which is always neglected, is the initial distribution of $\vec{k}_0$. In the electron emission model, what has been neglected is the initial distribution at the starting position where the potential energy equals the emission barrier as shown in Figure 5.3. There the electrons should have an energy distribution like
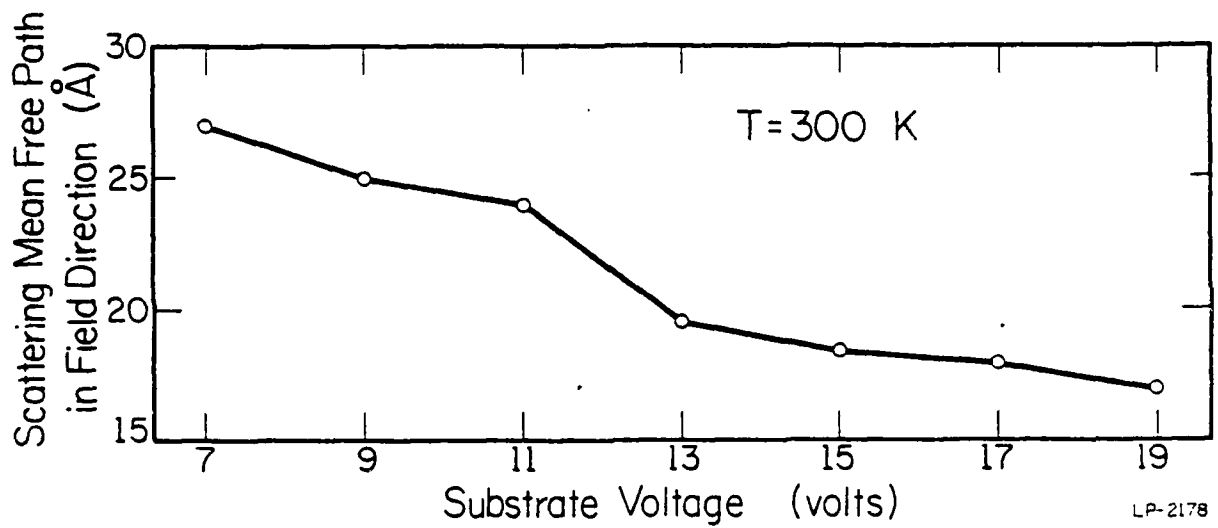
Figure 5.12: The scattering mean free path in the field direction plotted as a function of substrate voltage for device 15-2-9.

those shown in Figure 5.9 with an average energy of about 1 eV. If an average phonon energy of 0.05 eV is considered, then the electrons can, on the average, suffer 20 phonon emissions and still make it to the silicon dioxide layer. Although Ning's lucky electron model agrees with the experimental data, we doubt that one can relate direct physical meanings to the essentially adjustable parameters. Mathematically, however, his model is simple and appealing and can be directly applied to the modeling of devices.

5.5 Conclusion

We have shown that a transient Monte Carlo simulation can be used to correctly describe the emission process of electrons into the silicon dioxide layer. This Monte Carlo method takes into account the non-uniform spatial electric field which is the most important characteristic of the system. In this study, the inclusion of a realistic band structure is essential because this transport process involves very high energy electrons not describable by an effective mass approximation. Also, the second conduction band plays an important role since about half of the emissions are from this band. We are able to determine the right set of high field transport parameters from this study. This should be considered as a major success which improves the understanding of high field transport processes, like impact ionization phenomenon, and enables us to penetrate farther up into bands. Previous theories for impact ionization using Keldysh's formalism with $P \gg 1$ have shown to be incorrect in that the high energy tail of the distribution function is overly suppressed. The subtle balance between the high energy phonon scattering rate and impact ionization scattering rate as described in Chapter 4 is by no means

optimized because of the costly computing time which limits our freedom
to "play around" with the parameters. Unlike previous models for the
electron emission, impact ionization is naturally included in our cal-
culation.

We have also shown that the physics behind the emission process
can not be explained by the simple lucky electron model. Although the
lucky electron model consistently fits the experimental results, one
could, at best, look at it as a curve fitting scheme. For device modeling
purposes, this simple model is certainly the best one to use mathematically.
In Chapter 6, we discuss a better way to calculate the high energy phonon
scattering rate, including the quasi-particle self-energy effect.

CHAPTER 6

QUANTUM TRANSPORT IN SEMICONDUCTORS

6.1 Introduction

The theoretical basis for the transport study has been the semi-
classical Boltzmann equation. This equation is conceptually simple and
mathematically manageable. On a large time and length scale, classical
descriptions of the motion of the particles are usually acceptable.
But as the length scale of devices shrinks to the submicron range, where
extremely high electric fields are unavoidable, one has to question the
validity of the semiclassical Boltzmann equation.

The formalism of the quantum transport theory was basically de-
veloped in the pioneering work of Kohn and Luttinger (1957, 1958)[78,79],
Kubo (1957)[80], Dresden (1961)[81], Chester (1963)[82], Kubo (1966)[83],
and Luttinger (1968)[84]. The formalism is quantum mechanically rigorous,
but unfortunately, it is neither conceptually simple nor mathematically
manageable. The interesting work of Scott and Moore in 1972 [85] showed
that the quantum transport equation can be reduced to a quasi-particle
Boltzmann transport equation. This is encouraging in that one needs only
to include in the Boltzmann transport theory the quasi-particle character
which amounts essentially to a self-energy renormalization effect. In
1973, Barker rederived the quantum transport theory for high field
transport using a superoperator technique for semiconductors, and dis-
cussed in his work the possible first order quantum corrections to amend

the breakdown of the Boltzmann equation [86]. The results of his work also provide criteria for using the Boltzmann equation.

This chapter is devoted to the discussion of the classical and quantum transport equations and setting up confidence limits for the application of the Boltzmann equation. In Section 6.2, the assumptions of the Boltzmann equations are discussed and the usual approximations made in solving the equation are examined. In Section 6.3, the basis of the quantum transport equation is introduced and various quantum effects due to the high electric field and the strong coupling of the electron-phonon system are discussed. The quasi-particle concept is introduced and its self-energy due to the interaction with phonons is calculated. We also show how the scattering rate is obtained from the self-energy. A quantum Monte Carlo scheme is proposed. In Section 6.4, we show the transport results with the quantum corrections and assess the importance of the various quantum effects.

6.2 Assumptions of the Boltzmann Equation

The semiclassical Boltzmann equation is of the form

$$\frac{\partial f}{\partial t} + \frac{\partial f}{\partial t}\bigg|_{diff} + \frac{\partial f}{\partial t}\bigg|_{drift} + \frac{\partial f}{\partial t}\bigg|_{scatt} = 0 \ , \tag{6.1}$$

where

$$\frac{\partial f}{\partial t}\bigg|_{diff} = - \vec{v}_k \cdot \frac{\partial f}{\partial \vec{r}} \ , \tag{6.2}$$

$$\frac{\partial f}{\partial t}\bigg|_{drift} = - \frac{e}{\hbar} \vec{F} \cdot \frac{\partial f}{\partial \vec{k}} \tag{6.3}$$

and

$$\left.\frac{\partial f}{\partial t}\right|_{scatt} = \sum_{\vec{k}'} \left[f(\vec{k}')(1-f(\vec{k}))S(\vec{k}',\vec{k}) - f(\vec{k})(1-f(\vec{k}'))S(\vec{k},\vec{k}') \right] . \tag{6.4}$$

For nondegenerate semiconductors, we can ignore the Pauli principle since $f(k) \ll 1$, and replace $1-f$ by 1. Also, for elastic scatterings, $S(k',k)$ equals $S(k,k')$ because of microscopic reversibility (principle of detail balance). Thus,

$$\left.\frac{\partial f}{\partial t}\right|_{scatt} = \sum_{\vec{k}'} \left[f(\vec{k}') - f(\vec{k}) \right] S(\vec{k},\vec{k}') . \tag{6.5}$$

After the equation for f is solved, the macroscopic transport parameters, such as the electric current density, are obtained from

$$\vec{j} = - \sum_{\vec{k}} e \vec{v}_k f(\vec{k}) . \tag{6.6}$$

The assumptions involved in deriving the Boltzmann transport equation are

(1) Electrons are independent classical particles so that a distribution function $f(\vec{r},\vec{k};t)$ can be defined in classical phase space $(\vec{r},\vec{k})$.

(2) The electronic states are stationary (long life time) with a well-defined momentum $\vec{k}$.

(3) The effects of impurities and lattice vibrations (phonons) can be considered as perturbations causing weak scattering among the Bloch states.

(4) The external field solely accelerates the electrons between collisions and has no effects on the electronic states and the scattering events.

(5) The scattering events are considered to be local both in time and space. The duration of a collision is negligible. Thus, the transport processes are viewed on a coarse-grained time scale $\tau \gg \tau_c$, where τ_c is the collision duration.

From the assumptions, we see that the basic objection in the use of the Boltzmann equation is the exclusion of the uncertainty principle in the formalism. This raises the question whether the distribution function $f(\vec{r},\vec{k};t)$ can always be meaningfully defined in the classical phase space. If a steady state solution is of interest, then $f(\vec{k})$ can be properly defined without violating the position-momentum uncertainty principle. But there is always the energy-time uncertainty. Care has to be exercised in using the latter uncertainty relation, since time is not an operator [87]. Let us follow the qualitative discussion of Dresden [81] to explain how the uncertainty principle affects the concept of the distribution function.

For a given distribution function $f(E)$ and a state density function $\rho(E)$, the number density of electrons is given as

$$n(E) \ dE = f(E) \ \rho(E) \ dE \ . \tag{6.7}$$

$n(E)$ is interpreted as the number of electrons in an interval dE around energy E. The number density changes rapidly in a region kT around the average energy of electrons in a semiconductor. (In metals, it is the

Fermi energy.) In order to meaningfully define the distribution func-
tion, one should be able to define the number of electrons in energy
ranges small compared to kT. The basic uncertainty in the energy of the
electrons is of the order of $\hbar/\tau$, where $1/\tau$ is the total transition rate.
Thus, one must demand that

$$\frac{\hbar}{\tau} \ll kT \ . \tag{6.8}$$

Peierls has derived this relation quantitatively from time dependent
perturbation theory [88] but he has also shown that this relation can be
relaxed. In Equation 6.8, the relevant energy should be E, the electron
energy, instead of the thermal energy, kT. Thus, it is only required
that

$$\frac{\hbar}{\tau} \ll E \ . \tag{6.9}$$

Landau has also shown that for elastic scatterings only, the Boltzmann
equation can be derived without the assumption of Equation 6.7. Qualita-
tively, Equation 6.8 reads that the uncertainty in energy should be
negligible compared to the total kinetic energy of the electrons. This
actually holds true for most of the semiconductors.

Much of the incorrect nature of the classical Boltzmann equation can
be removed by introducing the notion of a quasi particle, which will be
discussed in the following sections. The more serious problems actually
lie in the usual approximations for solving the Boltzmann equation. For
transport problems in semiconductors, these are the effective mass approx-
imation (good for low field but not acceptable for high field transport),

the neglect of electron-electron interactions (good for low electron density only), the use of the Golden Rule and the Born approximation to calculate the scattering rate (good for low scattering rate only), and the neglect of the effect of electric fields on scatterings.

As will be discussed in the following sections, it turns out that the self-energy effect of a quasi particle plays the most important role in modifying the classical Boltzmann transport equation.

6.3 Quantum Transport and Quasi Particles

6.3.1 Introduction

The basis of the quantum transport theory is the quantum Liouville equation:

$$i\hbar \cdot \frac{d\Omega}{dt} = [H,\Omega] , \qquad (6.10)$$

where Ω is the density matrix of the system including both the carrier part and the phonon part, and H is the full Hamiltonian including the external force. For small external forces, the linear response theory developed by Kubo [83] can be applied to solve Equation 6.10. In the non-linear response regime caused by large external forces, Equation 6.10 becomes a mathematical nightmare in that the linearization of the equation can not be made and the phonon part and the carrier part of the density matrix can not be easily separated. The superoperator technique developed by Zwanzig [89] serves as a neat mathematical tool for finding the formal solution of Equation 6.10. But in order to get from the formal solution a mathematically manageable transport equation, some assumptions, not immediately justifiable, are made in the derivation. The only true justification of the assumptions made lies in the fact that the Boltzmann

equation can be reconstructed from the quantum transport equation in the classical limit.

Aside from the purely theoretical interest in developing the quantum transport theory, the purpose has been to look at possible first order correction terms to amend the classical Boltzmann equation. Scott and Moore [85] did an interesting study on the quantum electron-impurity transport problem. They used a Green's function technique and formally derived a quasi-particle Boltzmann equation. Their result suggests that the most important quantum correction in the transport problem is to bring in the notion of a quasi-particle for the Boltzmann equation.

6.3.2 Summary of Barker's Results [86]

Barker has adopted the superoperator technique and rederived the quantum transport theory for high field transport in semiconductors. He has investigated the effect of a high electric field on the scattering of the carrier. Here, we summarize his results and discuss qualitatively their physical implications.

(i) Self-Energy Effect

As discussed in Section 6.2, the scattering processes are treated as real transitions between sharp, unperturbed momentum states in the classical Boltzmann transport picture. The very existence of scattering and the presence of many scatterers make the assumption of an isolated scattering unrealistic. In fact, the carrier propagates in a perturbed state which is controlled by virtual scattering processes. The net effect is that the energy of a state is shifted by an amount which is the real part of the

self-energy, and the life time of a state is finite and is proportional
to the imaginary part of the self-energy. The state is collision
broadened. Because of the self-energy effect, the energy conserving
delta function becomes a smeared-out Lorentzian

$$\delta(E(\vec{k}) - E(\vec{k-q}) - \hbar\omega_{\vec{q}}) \rightarrow \frac{1}{\pi} \frac{\bar{\Gamma}(\vec{k},\vec{q})}{(E(\vec{k}) - E(\vec{k-q}) - \hbar\omega_{\vec{q}} - \bar{\Delta}(\vec{k},\vec{q}))^2 + \bar{\Gamma}^2(\vec{k},\vec{q})},$$

(6.11)

where

$$\bar{\Delta}(\vec{k},\vec{q}) = \Delta(\vec{k},E(\vec{k-q})) - \Delta(\vec{k-q},E(\vec{k})),$$ (6.12)

and

$$\bar{\Gamma}(\vec{k},\vec{q}) = \Gamma(\vec{k},E(\vec{k-q})) + \Gamma(\vec{k-q},E(\vec{k})).$$ (6.13)

The quantity Δ is the real part of the self-energy and Γ is the imaginary
part of the self-energy. Notice that when Δ and Γ approach zero, which
is the case for weak coupling, the Lorentzian structure goes back to the
form of a delta function. The physical implication of the self-energy ef-
fect is that the particle is scattered to a range of quasi particle states
according to the Lorentzian distribution.

What has been described is essentially the characteristics of a quasi-
particle. We will come back to more detail when we introduce the quasi-
particle concept.

(ii) Intra-Collisional Field Effect

In an actual scattering event, the interaction between the particles
takes a finite time. In the presence of an electric field, the carrier

gains (or looses) energy during the finite collision duration. If the energy gained (or lost) during the collision duration is much greater than the collision broadening of the state of the carrier, then modifications need be made to the scattering rate. The energy gained (or lost) during the collision is expressed as

$$E_{cd} = \left| e\vec{F} \cdot \vec{v} \right| \cdot \tau_c , \tag{6.14}$$

where $\vec{F}$ is the electric field, $\vec{v}$ is the velocity of the carrier, and τ_c is the collision duration. For a rough estimate, the collision duration can be written as

$$\tau_c = \frac{\lambda_D}{v} , \tag{6.15}$$

where v is again the velocity of the carrier, and λ_D, the deBroglie wave length of the carrier, is given as

$$\lambda_D = \frac{2\pi}{k} , \tag{6.16}$$

where k is the crystal momentum of the carrier. In other words, the collision duration τ_c is just one period of the particle wave. Quantum mechanically, one can think of the collision duration as the time it takes for a particle to fully manifest its wave characteristics. Mathematically, the collision broadened scattering rate, calculated by using Equation 6.11, is essentially unmodified by the presence of an electric field if the following criterion is met:

$$\frac{E_{cd}}{\bar{\Gamma}} \leq 1 , \tag{6.17}$$

where E_{cd} is given by Equation 6.14 and $\bar{\Gamma}$ is given by Equation 6.13.

In the weak coupling regime (low carrier energy, low scattering rate) where Γ is small, the criterion given by Equation 6.17 might be violated. But the carrier distribution is heated up significantly under high electric fields so that most of the carriers reside at high energies, and hence in the strong scattering regime, where Γ is very large. It is unlikely that Equation 6.17 is violated for carriers in the high energy range. In Section 6.4, we present the Monte Carlo result to assess quantitatively the intra-collisional field effect.

6.3.3 Quasi Particle

For a noninteracting system, the wave function of a particle in a momentum state $\vec{k}$ evolves as

$$\psi(t) \sim e^{-i\frac{E(\vec{k})}{\hbar}t} , \tag{6.18}$$

where $E(\vec{k})$ is the energy of the free-particle state $\vec{k}$. The propagation of this particle is undamped and the frequency of oscillation is just the free-particle energy $E(\vec{k})$. If we take the Fourier transform of Equation 6.18, we obtain the spectral density function as

$$A(\omega,E) \sim \delta(\omega - \frac{E(\vec{k})}{\hbar}) . \tag{6.19}$$

For an interacting system, the energy of the particle in a momentum state $\vec{k}$ is modified. The interaction introduces an extra energy to the particle and hence the evolution of the wave function of the particle is determined by

$$\psi(t) \sim e^{-i \frac{(E(\vec{k}) + \Sigma(\vec{k}))}{\hbar} t} , \tag{6.20}$$

where $\Sigma(\vec{k})$ is called the self-energy of the particle and is in complex form expressed as

$$\Sigma(\vec{k}) = \Delta(\vec{k}) - i\Gamma(\vec{k}) . \tag{6.21}$$

Thus, the wave function evolves as

$$\psi(t) \sim e^{-i \frac{E(\vec{k}) + \Delta(\vec{k})}{\hbar} t} e^{- \frac{\Gamma(\vec{k})}{\hbar} t} . \tag{6.22}$$

The real part of the self-energy introduces a level shift of the eigen-states, and the imaginary part, which is related to the level broadening, damps the magnitude of the wave function. The magnitude square of the wave function, which represents the probability of a particle in a state, follows

$$|\psi(t)|^2 \sim e^{- \frac{t}{\tau_k}} , \tag{6.23}$$

where

$$\tau_k = \frac{\hbar}{2\Gamma(\vec{k})} \tag{6.24}$$

is the life time of a particle in the momentum state $\vec{k}$. In first order approximation, $1/\tau_k$ corresponds to the scattering rate of the particle in the state $\vec{k}$. This will be justified when we formally derive the self-energy. If we take the Fourier tra. ior of Equation 6.22 and change sign in the second exponent for $t < 0$, we have

$$A(\omega,E) \sim \frac{1}{\left[\omega - \frac{E(\vec{k}) + \Delta(\vec{k})}{\hbar}\right]^2 + \left[\frac{\Gamma(\vec{k})}{\hbar}\right]^2} \quad . \tag{6.25}$$

One sees that the spectral density function takes the Lorentzian form and peaks at the energy $E(\vec{k}) + \Delta$. The state is broadened.

We see that in an interacting system, the state has a natural life time and the particle decays out of its initial state. In order to still use the concept of a particle, one defines the concept of a quasi particle. A quasi particle in a momentum state $\vec{k}$ is defined as a particle with momentum $\vec{k}$, energy $E(\vec{k}) + \Delta$ and a broadened spectral density function given by Equation 6.25. The concept is justified for times t which satisfy

$$\frac{\hbar}{E} \lesssim t \lesssim \frac{\hbar}{\Gamma} \quad . \tag{6.26}$$

What has been described are simple, qualitative concepts of a quasi particle. For a rigorous discussion, the reader is referred to Pine's book, The Many Body Problem [90]. The important task remaining is to find the self-energy which characterizes the properties of a quasi particle.

We start with an approximation to the self-energy Σ which neglects the vertex correction [91]. It is represented by the diagram shown in Figure 6.1. The double line represents the full propagator which is the dressed Green's function of the electron. It emits phonons and reabsorbs them back by virtual processes. The self-energy of the electron due to

$$\Sigma(\vec{k}) = $$

with labels $D(\vec{q}, \hbar\omega)$ above and $G(\vec{k}-\vec{q}, E-\hbar\omega)$ below.

LP-2221

Figure 6.1: The diagram for the self-energy of the electron-phonon interaction.

all of these virtual processes, is immediately written down by applying

the diagrammatic rule [92] as

$$\Sigma(\vec{k},E) = i \int \frac{d^3q\,d\omega}{(2\pi)^4} V^2(\vec{q}) D(\vec{q},\hbar\omega) G(\vec{k}-\vec{q},E-h\omega) \ , \tag{6.27}$$

where G is the Green's function of the electron, D is the Green's function of the phonon, and $V(\vec{q})$ is the coupling between the electron and phonon. The electron Green's function [93] is expressed as

$$G(k,E) = \frac{1}{E - E(\vec{k}) - \Sigma(\vec{k},E) + i\delta} \tag{6.28}$$

and the phonon Green's function [94] is expressed as

$$D(\vec{q},\hbar\omega) = \alpha_{\vec{q}}^2 \left[\frac{1}{\hbar\omega - \hbar\omega_{\vec{q}}^o + i\delta} - \frac{1}{\hbar\omega + \hbar\omega_{\vec{q}}^o - i\delta} \right] \ , \tag{6.29}$$

where $\omega_{\vec{q}}^o$ is the free phonon frequency of the mode $\vec{q}$ and δ is a positive

infinitesimal quantity. These are the ground state Green's functions

(zero temperature) which are good in the high energy range where the zero-

point-lattice is a good approximation [24]. Inserting Equations 6.28 and

6.29 into Equation 6.27, one gets the ω-dependent integral

$$I = \int \frac{d\omega}{2\pi} \left(\frac{1}{E - \hbar\omega - E(\vec{k}-\vec{q}) - \Sigma(\vec{k}-\vec{q},E-\hbar\omega) + i\delta} \right) \tag{6.30}$$

$$\cdot \left(\frac{1}{\hbar\omega - \hbar\omega_{\vec{q}}^o + i\delta} - \frac{1}{\hbar\omega + \hbar\omega_{\vec{q}}^o - i\delta} \right)$$

which can be evaluated by contour integration. The integrand has three

poles in the complex plane. The two poles $\hbar\omega = -\hbar\omega_{\vec{q}}^{o} + i\delta$ and

$\hbar\omega = E - E(\vec{k}-\vec{q}) - Re\Sigma + i(\delta - Im\Sigma)$ are on the upper half plane ($\Gamma = -Im\Sigma$,

which is proportional to the life time, is always positive), and the

pole $\hbar\omega = \hbar\omega_q - i\delta$ is on the lower half plane. One can either close the

contour in the upper or lower half planes, depending on which is more con-

venient. By closing the contour in the lower half plane, one finds

$$I = \frac{-i/\hbar}{E - \hbar\omega_{\vec{q}}^{o} - E(\vec{k}-\vec{q}) - \Sigma(\vec{k}-\vec{q}, E-\hbar\omega_{\vec{q}}^{o}) + i\delta} \tag{6.31}$$

by applying the residue theorem [95]. The self-energy expression is

thus simplified to

$$\Sigma(k,E) = \int \frac{d^3q'}{(2\pi)^3} \frac{g^2(\vec{k}+\vec{q}')}{E-\hbar\omega_{\vec{q}}^{o} - E(\vec{q}') - \Sigma(\vec{q}', E-\hbar\omega_{\vec{k}+\vec{q}'}^{o}) + i\sigma} , \tag{6.32}$$

where $\vec{q}' = \vec{k}-\vec{q}$ and $g^2(\vec{q})$ lumps all the factors together. Let us consider

the case of the optical phonon scattering with $\omega_{\vec{q}}^{o} = \omega_{op}$ and assume that

$g(\vec{q})$ is a constant instead of a function of $\vec{q}$, i.e., the usual approxi-

mation of a constant deformation potential. One sees that $\Sigma(\vec{k},E)$ be-

comes a function of the energy only after the integration of $\vec{q}'$.

Utilizing the relation

$$\int \frac{d^3q}{(2\pi)^3} F(E(\vec{q})) = \int dE \, \rho(E) \, F(E) , \tag{6.33}$$

where F is any function, $\rho(E)$ is the density of states and the crystal volume is taken as one, Equation 6.32 then takes the form

$$\Sigma(E) = g^2 \int \frac{dE'\rho(E')}{E-\hbar\omega_{op} - E' - \Sigma(E - \hbar\omega_{op}) + i\delta} \quad . \tag{6.34}$$

Equation 6.34 can be solved numerically using the density of states calculated from the pseudopotential band structure [37].

Let us now consider the weak coupling limit ($g \ll 1$) where Σ in the denominator can be neglected, i.e., an equation for the lowest order self-energy. By use of Dirac's formula [95]

$$\frac{1}{x'-x \pm i\delta} = P \frac{1}{x'-x} \pm i\pi\delta(x'-x) \quad , \tag{6.35}$$

Equation 6.34 becomes

$$\Sigma(E) = P \int \frac{dE' g^2 \rho(E')}{E-\hbar\omega_{op}-E'} - i\pi g^2 \rho(E-h\omega_{op}) \quad . \tag{6.36}$$

For $\Sigma(E) = \Delta(E) - i\Gamma(E)$,

$$\Delta(E) = P \int \frac{dE' g^2 \rho(E')}{E-\hbar\omega_{op} - E'} \tag{6.37}$$

and

$$\Gamma(E) = \tau g^2 \rho(E-\hbar\omega_{op}) \quad . \tag{6.38}$$

Note that the real part $\Delta(E)$ is just the energy correction of the second order perturbation theory [96] and the imaginary part $\Gamma(E)$ is similar to the form of the Golden rule in the Born approximation. As discussed earlier in the text, $2h/\Gamma(E)$ is the life time of the state. The self-energy $\Sigma(E(\vec{k}))$, which is due to all possible virtual scatterings of the same initial and final state, represents the forward scattering amplitude. In the approximation that the vertex part of the diagram can be neglected [97], $\Sigma(E(\vec{k}))$ is simply $<\vec{k}|T|\vec{k}>$, where T is the transition matrix [98]. If we assume the scattering is elastic, then the scattering probability is conserved and the optical theorem [98]

$$\sigma_{tot} = - \frac{2}{hv_k} \text{ Im } <\vec{k}|T|\vec{k}>$$

$$= - \frac{2}{hv_k} \text{ Im } \Sigma(E(\vec{k})) \tag{6.39}$$

can be applied to give the total scattering rate as

$$\frac{1}{\tau} = \sigma_{tot} v_k = \frac{2\Gamma(E(\vec{k}))}{h} . \tag{6.40}$$

One sees that the scattering rate is just the inverse life time of the state. Thus, the total scattering rate is given as

$$\frac{1}{\tau_B(E)} = \frac{2\pi}{h} g^2 \rho(E-h\omega_{op}) , \tag{6.41}$$

which is exactly the Golden rule in the Born approximation for phonon emission with $|H'|^2 = g^2$, the squared matrix element as given in Appendix 2.

Since we start out with the ground state Green's function, only phonon

emission can occur in the scattering process.

What has been derived is valid for high energy scattering processes

where the zero-point-lattice serves as a good approximation. By solving

Equation 6.34, the total scattering cross section can be calculated from

Equation 6.39 in the elastic limit. For impurity scatterings, Equation

6.39 is exact. In a real solid, there is more than one scattering

mechanism, for example, the scatterings of different phonon types, the

impact ionization scattering, etc. The self-energy formalism discussed

above is only true for one type of scattering. One can treat separately

the different scattering mechanisms and sum algebraically the self-

energies, assuming that the cross diagrams for different scattering types

can be neglected. The justification for the assumption is an open ques-

tion which needs to be further pursued. We propose in the next section

a quantum Monte Carlo procedure in the spirit of a quasi-particle picture.

6.3.4 Quantum Monte Carlo

Up to now, we have discussed that the most important quantum cor-

rection to the transport problem is to bring in the notion of a quasi-

particle. As mentioned in Chapter 2, it has been proven that a Monte

Carlo simulation solves the Boltzmann equation [16,20]. With the quasi-

particle Boltzmann equation being formally the same as the classical

Boltzmann equation, it is also solved by the Monte Carlo simulation pro-

vided the quasi particle characteristics are properly included in the

simulation. The self-energy, which is the main characteristic of a quasi-

particle, has two effects on a momentum state: it shifts the energy of the state by an amount equal to its real part, and it collision-broadens the state with a Lorentzian structure whose half width equals its imaginary part. For our Monte Carlo method, including a realistic band structure, the contribution from the real part can be neglected, since it is partly accounted for in the empirical pseudopotential band structure. As for the imaginary part, the broadened spectral density function (Equation 6.25) results in a smeared-out Lorentzian structure (Equation 6.11). This takes the place of the energy conserving delta function in the scattering process as derived by Barker [86]. This factor can be taken care of by scattering the electron into a range of quasi-particle final states according to the Lorentzian structure. Assuming a constant coupling as discussed in the last section, the self-energy is a function of the energy only. Thus, the joint real and imaginary parts are rewritten as

$$\bar{\Delta} = \Delta(E(\vec{k}-\vec{q})) - \Delta(E(\vec{k})) \qquad (6.42)$$

and

$$\bar{\Gamma} = \Gamma(E(\vec{k}-\vec{q})) + \Gamma(E(\vec{k})) . \qquad (6.43)$$

We see that the joint broadening depends both on the energy of the initial and the final states. It is very difficult to realize this distribution in the Monte Carlo simulation effectively and efficiently. Our simplifying procedure is that we consider the initial state broadening only, and scatter the electron into an energy range of $2\Gamma_i$, the full width, according

to the distribution. The partial justification for scattering only into an energy range of the full width is because the Lorentzian tail extends both far up and down in energy where scattering mechanisms other than the one responsible for this broadening might be important, and this formula, derived for a single scattering mechanism, might not be valid. The equation of motion for the particle stays the same, as has been shown in [85]. So the free flight time can be found the same way by solving Equation 2.1, except that one uses the scattering rate calculated from the self-energy in the high energy, strong coupling regime.

The above proposed scheme is by no means complete. It attempts to serve as a first step toward the further understanding of the quantum transport problem.

6.4   Results and Discussion

We discuss first the results of numerical solutions to Equation 6.34 for the self-energy, using an empirical pseudopotential band structure [37,99].

In Figure 6.2, we show the result of the self-energy due to the intervalley electron-phonon interaction in GaAs. In this calculation, the intervalley phonon energy is assumed to be 28 meV, an average of the different intervalley phonon energies, and the coupling constant $g^2 = 0.06$ is selected such that the low energy scattering rate agrees with what describes the Gunn effect [25,36]. The solid line represents the shifted density of states $\rho(E-\hbar\omega_{op})$ multiplied by πg^2, which is the imaginary part of the lowest order self-energy as described by Equation 6.38. The dashed line represents the imaginary part of the full order self-energy as
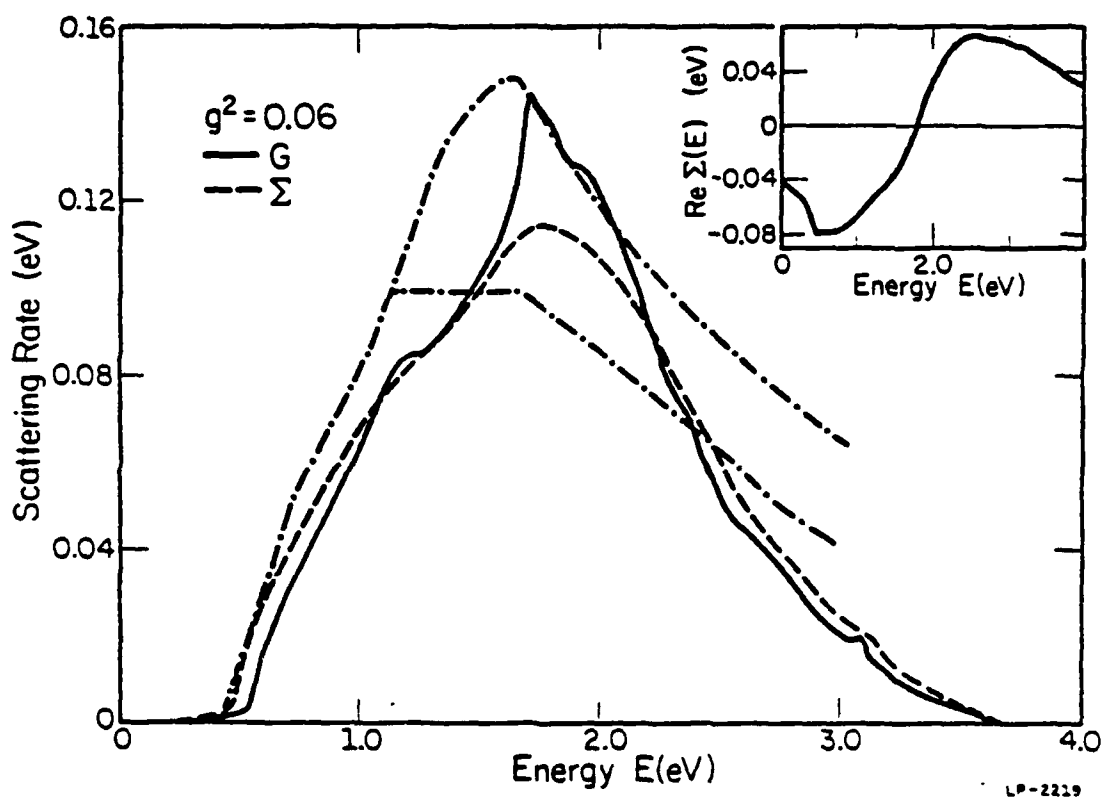
Figure 6.2: The scattering rates (the imaginary part of the self-energy) plotted as a function of the electron energy. The solid curve corresponds to the first order self-energy and the dashed curve corresponds to the full order self-energy. The dash-dotted curves are that used in the calculations. The inset shows the real part of the self-energy.

described by Equation 6.34. We see that the full order self-energy correction is negligible for energies below ˜0.6 eV. It is broadened and suppressed by about 20% around the peak of the density of states. The real part of the full order self-energy, which is partly taken care of in the empirical pseudopotential calculation, is shown in the inset of the figure. Also included in the figure are the scattering rates used in the previous Monte Carlo simulation by Shichijo et al. (high dash-dotted curve) and the present Monte Carlo simulation (low dash-dotted curve) which will be discussed later. To illustrate the coupling-constant dependence of the scattering rate, we plot in Figure 6.3 the imaginary part of the self-energy Γ for five coupling constants. We find that the scattering rate at the density-of-states peak grows almost linearly with g^2 within the selected range.

There are many different phonon types for the intervalley scattering in silicon [18]. As discussed in Section 6.3.3, it is not clear how one includes the contribution of the mixed interaction with different phonon types to the self-energy. Therefore, we pick a phonon energy of 65 meV and a coupling constant of g^2 = .07 to look qualitatively at the self-energy effect. Figure 6.4 shows the imaginary part of the self-energy for two conduction bands in Si. The solid and the dashed curves in this figure correspond to that described for Figure 6.2. The scattering rate from the full self-energy is again broadened and suppressed around the two peaks. Note that it is suppressed by over 50% at the second peak. The real part of the self-energy is shown in the inset of the figure. Qualitatively, our empirical scattering rate shown in Figure 4.9 agrees with the self-energy scattering rate for energies below 3 eV.
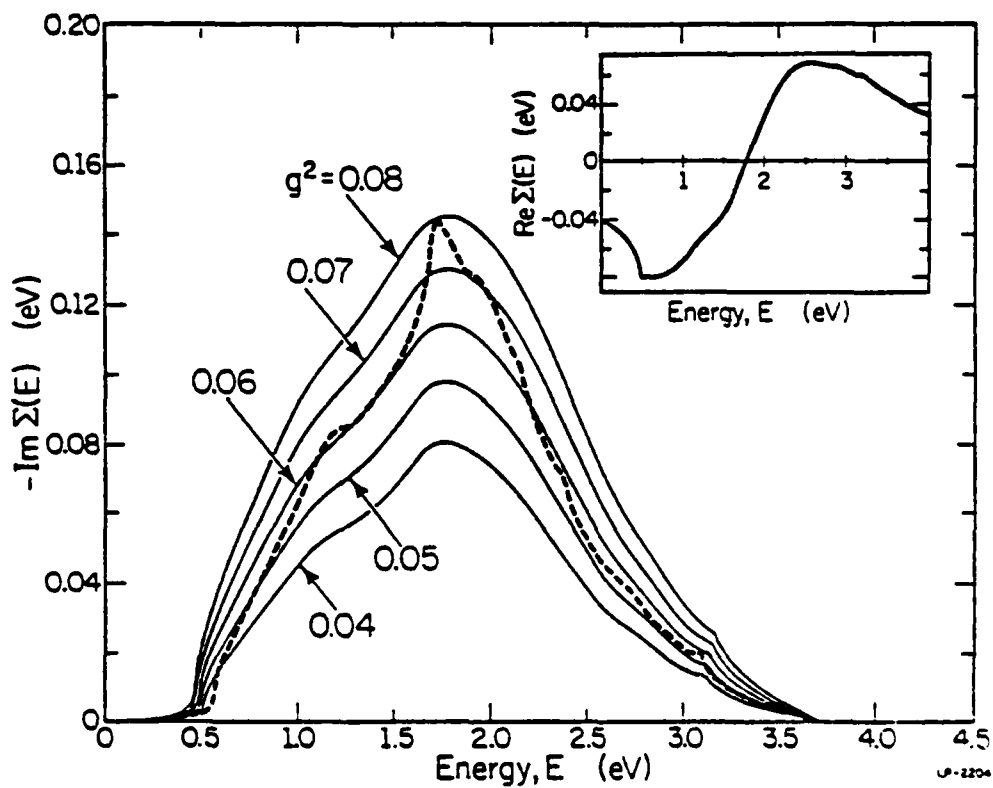
Figure 6.3: The imaginary part of the self-energy plotted for different coupling constants. The dashed curve is the first order self-energy with $g^2 = 0.06$. The real part of the self-energy for $g^2 = 0.06$ is shown in the inset of the figure.
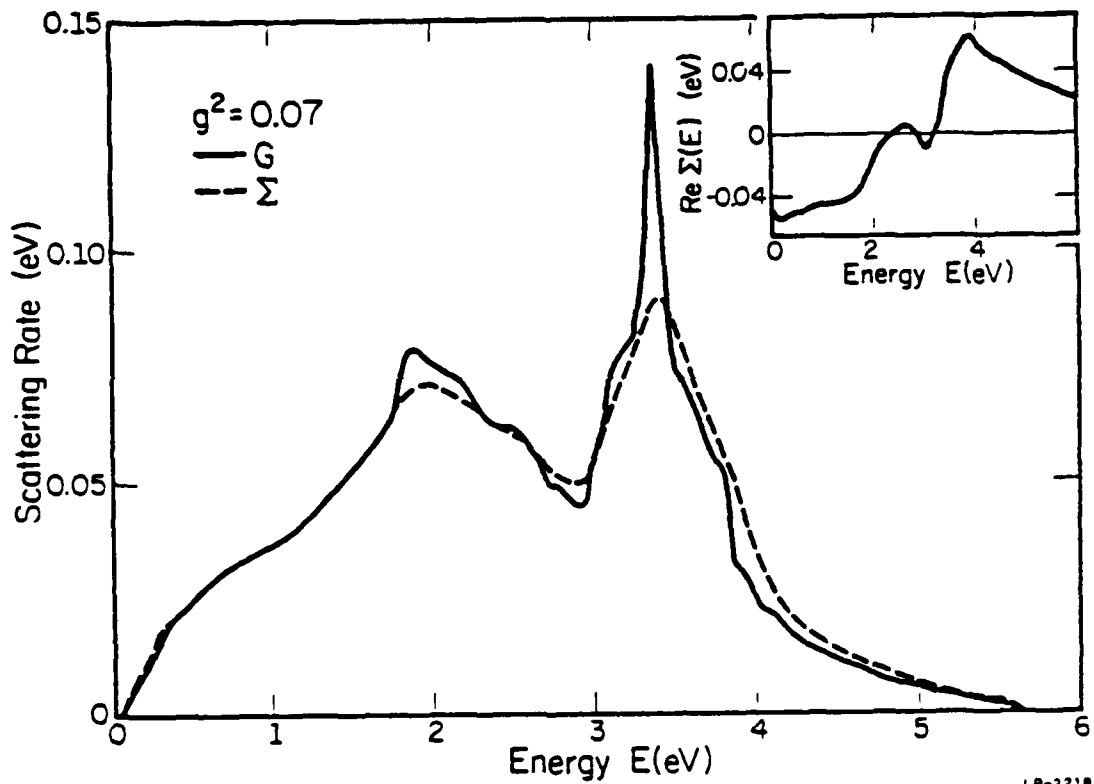
Figure 6.4: The scattering rate (the imaginary part of the self-energy) plotted as a function of energy. The solid line is the first order self-energy (the Golden rule in the Born approximation) and the dashed line is the full order self-energy. The inset shows the real part of the self-energy.

The coupling-constant dependence of the scattering is shown in Figure 6.5. The qualitative behavior is the same as that of Figure 6.3 for GaAs.

In our quantum Monte Carlo simulation, we still adopt the empirical scattering rate as discussed in Chapters 4 and 5 for Si and the lower dash-dotted curve shown in Figure 6.2 which *fits the experimental results for GaAs better*. In Figure 6.6, the impact ionization coefficient α for GaAs is shown for both the quantum and the classical Monte Carlo simulations. All results fall into the cross-hatched region which indicates the range of the available experimental data [100-103]. We see that the collision broadening effect enhances consistently the impact ionization, although the differences are almost within the error of the simulation. Figure 6.7 shows the analogous results for Si. Again, the collision broadening effect enhances the impact ionization. This can be understood because the collision broadened spectral density allows some finite probability for an electron in a momentum state $\vec{k}$ to have an energy greater than $E(\vec{k})$. Consider the following "thought" experiment:

Suppose we put an electron in a state $E(\vec{k})$ in a solid where interaction between the electron and the lattice can be turned off. When there is no interaction, the electron stays in the same state as time evolves. We then open "window" such that electrons with energy $E(\vec{k})$ escape out of the solid with the following probability:

$$P_{esc} = \begin{cases} 1 & \text{for } E(k) \geq E_o \\ 0 & \text{for } E(k) < E_o \end{cases} \tag{6.44}$$
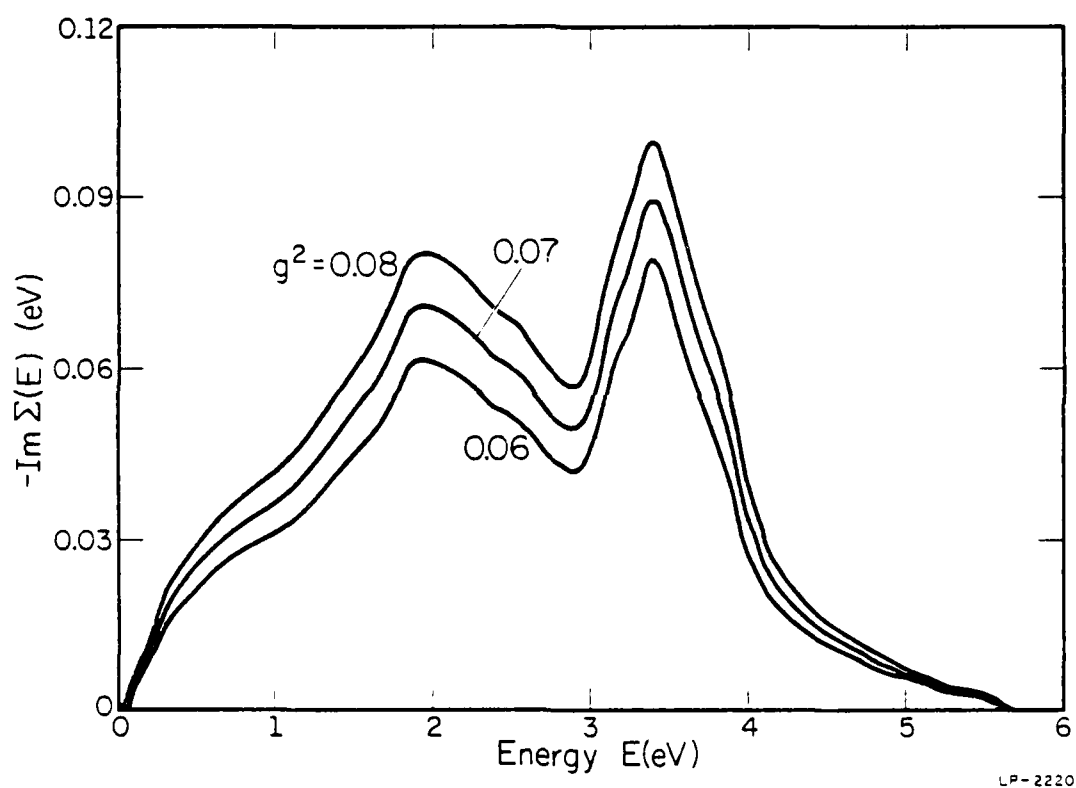
Figure 6.5: The imaginary part of the self-energy for
different coupling constants.
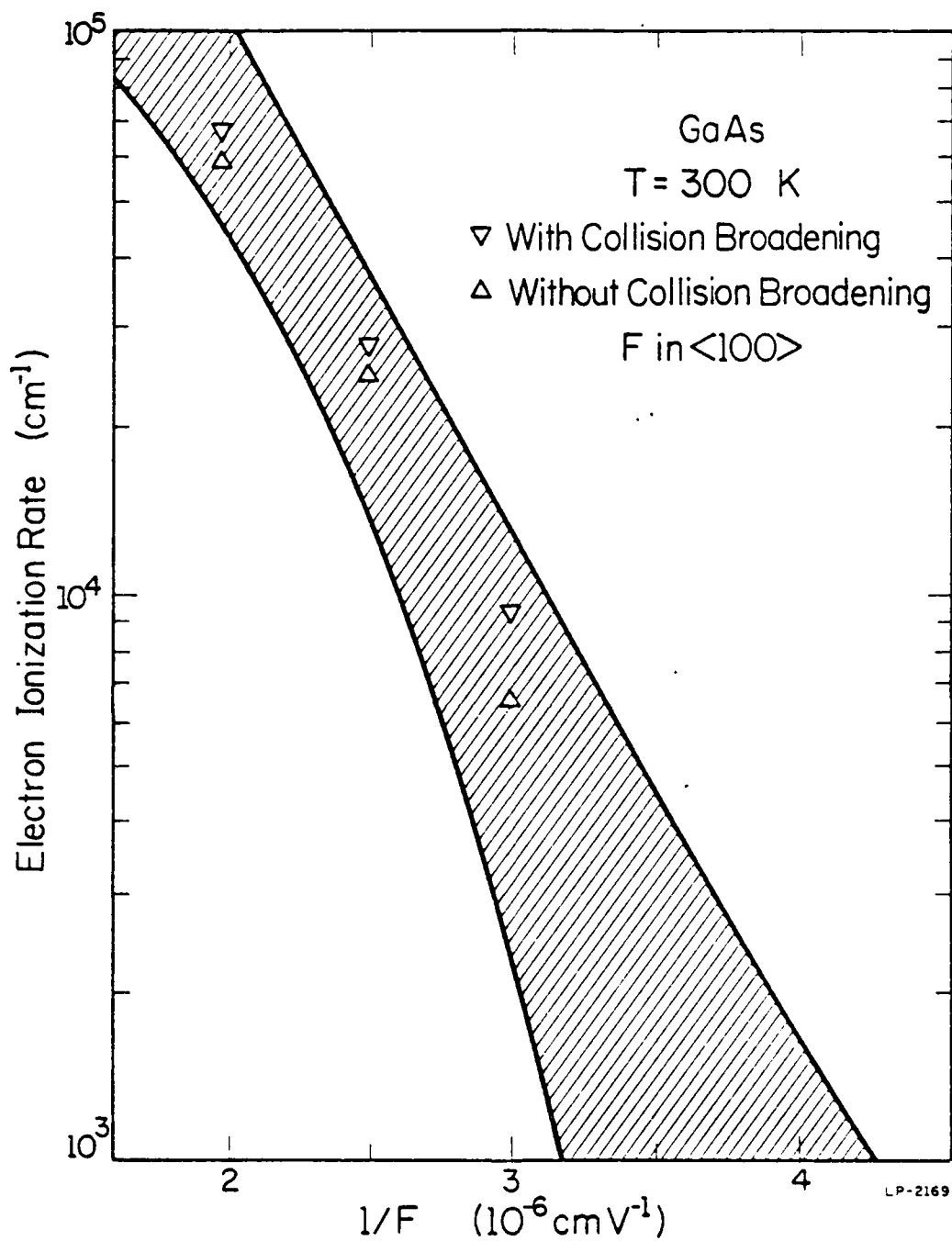
Figure 6.6: Calculated ionization coefficients as a function
of the inverse field strength. The shaded region
represents the available experimental results.
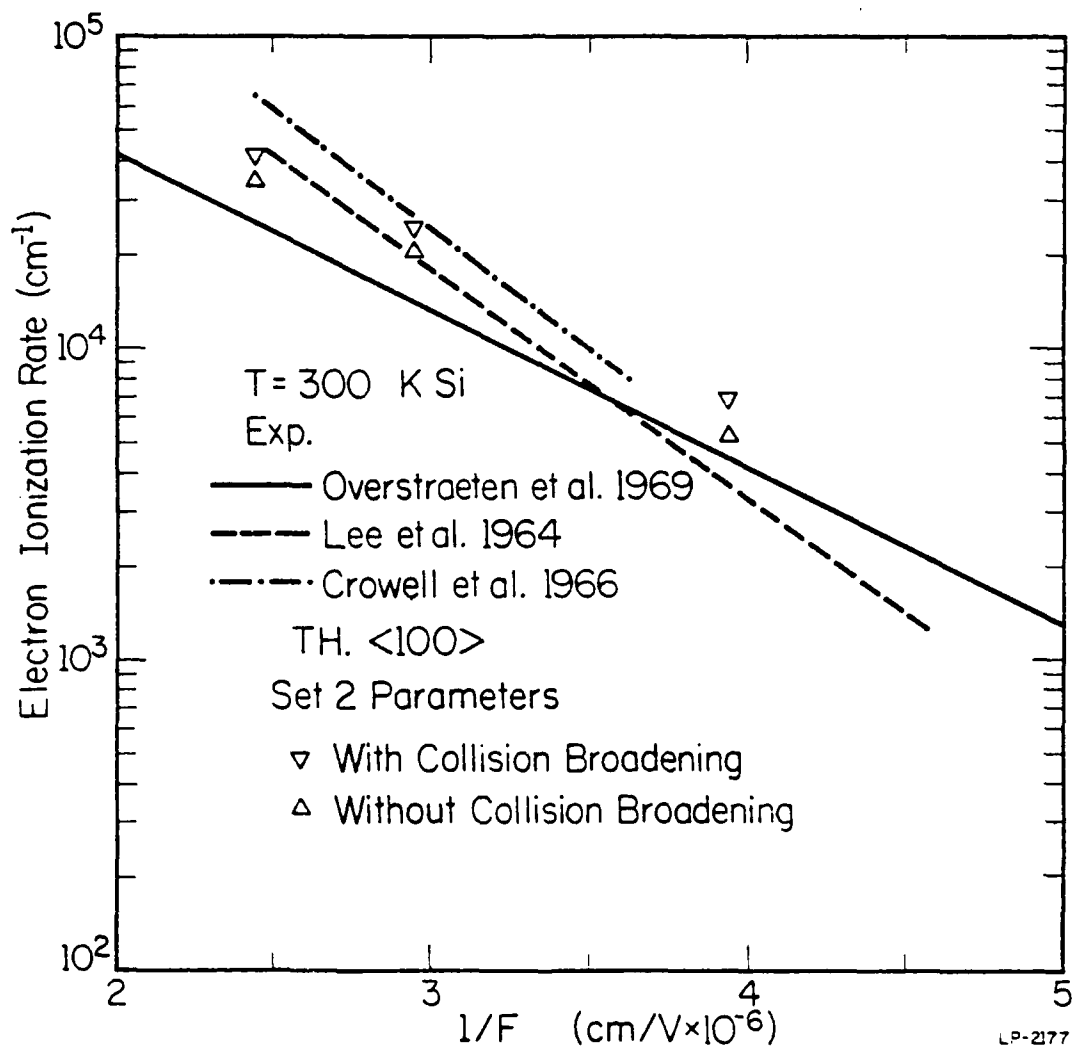
Figure 6.7: Calculated ionization coefficients as a function of the inverse field strength.

Now we turn the interaction on and the electron starts to behave like a quasi particle with a broadened energy spectrum as time evolves. If we assume the same collision broadening Γ for all the states and neglect the shifts in energy caused by the real part of the self-energy, the escaping probability for an electron in a state $E(\vec{k})$ becomes a folded integral

$$P_{esc}^{c}(E) = \int_{-\infty}^{\infty} A(E',E) \, P_{esc}(E') \, dE' \quad , \tag{6.45}$$

where $A(E',E)$, the normalized spectral density function from Equation 6.25, is expressed as

$$A(E',E) = \frac{1}{\pi} \frac{\Gamma}{(E'-E)^2 + \Gamma^2} \quad . \tag{6.46}$$

Equation 6.44 can be analytically integrated to give

$$P_{esc}^{c}(E) = \frac{1}{2} - \frac{1}{\pi} \tan^{-1} \frac{E_0 - E}{\Gamma} \quad . \tag{6.47}$$

The collision broadened probability is plotted in Figure 6.8. We see that the probability is smeared-out around E_0, then the effect of the collision broadening is to smear the sharp edge of the barrier. In a sense, the barrier height is effectively reduced for the electrons residing in the energy range below the barrier height. This justifies the argument in Chapter 5 that the emission barrier at the Si-SiO$_2$ interface should be further reduced due to the collision broadening effect.
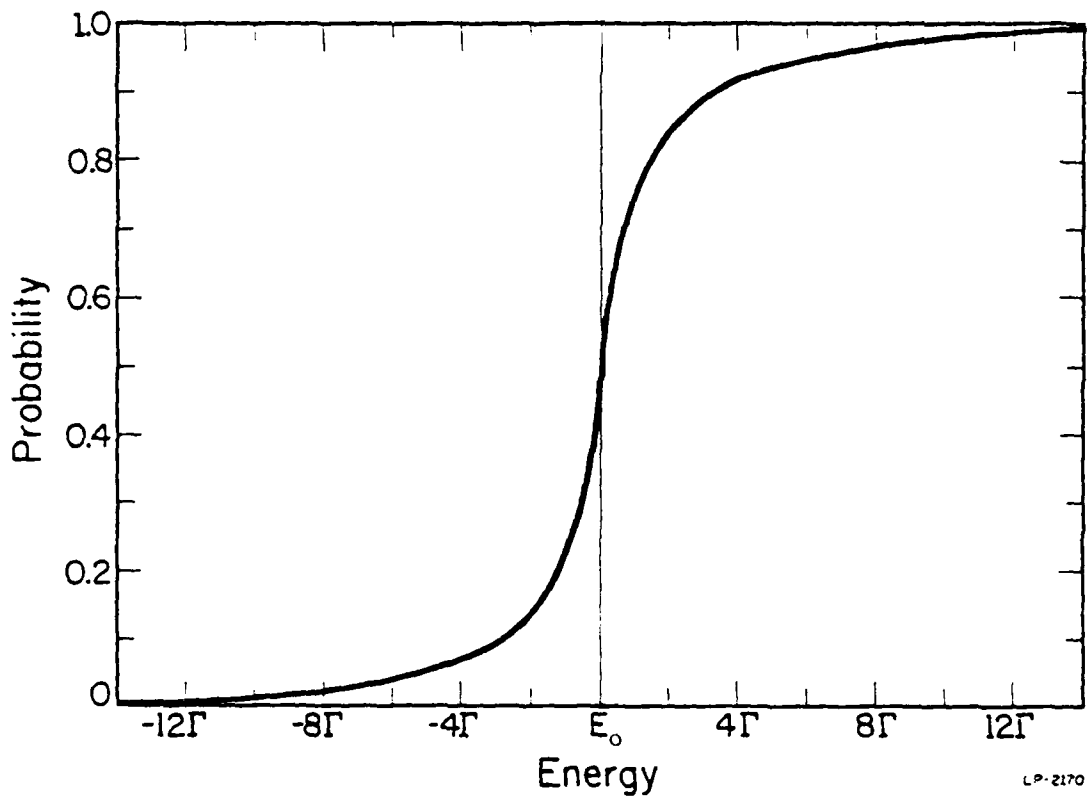
Figure 6.8: The escaping probability as described in the text.

The "experiment" described above is by no means rigorous. It describes, at most, the qualitative nature of the collision broadening. A better understanding of the whole problem would require a full-blown many body quantum mechanical treatment which should be a full research project in its own right.

Finally, we show in Figure 6.9 the intra-collisional field effect (ICFE) for the steady state high field transport in Si and GaAs. ICFE is defined here to be the average ratio of the energy gained in the collision duration to the collision broadening half width as given in Equation 6.17. We see that the percentage effect is very small. As discussed in Section 6.3.2(ii), it is simply because the distribution is so heated up by the high electric field that the electrons are mostly residing in the high energy range where the ICFE is negligible. This effect might be important in the initial high field transient regime as discussed by Barker [86]. Notice, however, that the formula for the ICFE was derived by an effective mass approximation. The validity of the formula in high energies needs further justification.

6.5 Summary

The quantum transport theory has been in existence for many years [78-86]. Despite the many efforts of trying to construct a quantum transport equation, which describes transport physics better, they always end up facing an insolvable transport equation. This seriously limits the progress in the quantitative understanding of the transport problem. In this work, we have discussed the assumptions of the classical Boltzmann equation to the quantum self-energy effect and proposed a quantum Monte
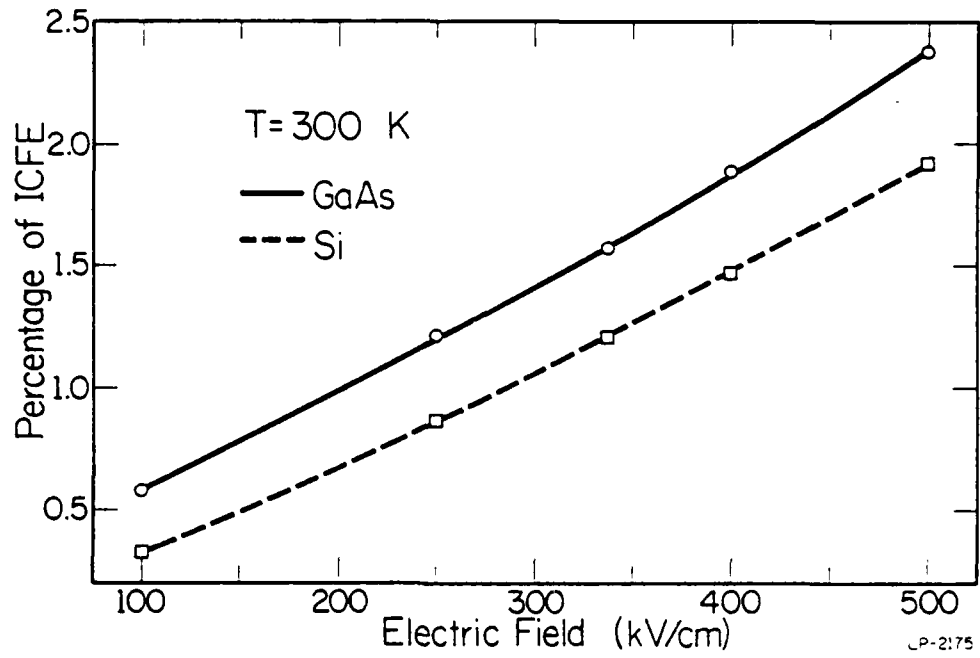
Figure 6.9: The intra-collisional field effect (ICFE) as a
function of electric field for GaAs and Si.

Carlo method. Our quantum Monte Carlo method differs from the classical one in that the quasi-particle characteristics have been taken care of in the simulation. A rigorous justification of the method proposed will require further investigation. It is hoped that the quantum Monte Carlo method developed in this work will serve as a starting basis for future research.

As for the transport parameters, the deformation potentials which crucially determine the scattering rates have been treated essentially as adjustable parameters. A first principal theory for calculating the deformation potential is of utmost importance.

It has been demonstrated in this thesis work that the Monte Carlo simulation can be used to treat a large variety of transport problems inaccessible by any other means. Future challenges in improving the Monte Carlo method will be to include the electron-electron scattering; to refine the band structure interpolation scheme; to calculate the scattering rates, including the quantum effects; etc. The Monte Carlo method is powerful, flexible, and not limited by itself. The only limitations to this method are the capacity and speed of the computer and the lack of the fundamental understanding of the basic transport parameters.

APPENDIX 1

DETERMINATION OF THE CARRIER FREE FLIGHT TIME
IN A MONTE CARLO SIMULATION

In a Monte Carlo simulation, the determination of the free flight time is one of the most important objectives. A better method improves the speed of the program and the accuracy of the simulation. The free flight time is the time that the electron drifts freely between successive collisions. The lengths of the free flight times follow a distribution directly related to the scattering rates in the semiconductor. In this appendix, we derive this distribution and discuss how this distribution can be properly implemented in the Monte Carlo simulation.

Suppose that $P(t_1)$ is the probability that an electron drifts freely from time $t = 0$ to time $t = t_1$. The probability for the electron not to be scattered in the time interval $t_1 < t < t_1 + \Delta t$ is proportional to the total scattering rate of the electron and the length of the interval as $\Delta t / \tau(t_1)$. So the probability of the electron not getting scattered in this interval is simply $1 - \Delta t / \tau(t_1)$. It follows immediately that the probability of the electron drifting freely from time $t = 0$ to time $t = t_1 + \Delta t$ can be written as

$$P(t_1 + \Delta t) \simeq P(t_1)(1 - \frac{\Delta t}{\tau(t_1)}) \ . \tag{A1.1}$$

If Δt is an infinitesimal increment of time, which then makes Equation A1.1 exact, $P(t)$ is solved as

$$P(t_1) = \exp \left[- \int_0^{t_1} \frac{1}{\tau(t')} \, dt' \right] , \qquad (A1.2)$$

where $P(0)$ is assumed to be one. If τ is a constant, then $P(t)$ is simply a Poisson distribution and the mean of which is just τ, a constant scattering mean free time. Unfortunately, τ is a complicated function of the crystal momenta and is usually simplified to be a function of the energy which implies the assumption of isotropic scattering.

What is required in a Monte Carlo simulation is a means to determine the time interval T in which the electron drifts freely, and is scattered at the end of the interval. From Equation A1.2, and knowing that the probability per unit time of having one scattering event at $t=t_1$ is just the scattering rate at $t=t_1$, the distribution for T can be expressed as

$$P_{sc}(T) = P(t) \frac{1}{\tau(T)} = \frac{1}{\tau(T)} \exp \left[- \int_0^T \frac{dt'}{\tau(t')} \right] . \qquad (A1.3)$$

By generating a random number r uniformly distributed between 0 and 1, T can be obtained by solving

$$r = \int_0^T P_{sc}(t) \, dt$$

$$P(t_1) = \exp\left[-\int_0^{t_1} \frac{1}{\tau(t')}\, dt'\right], \qquad\qquad (A1.2)$$

where $P(0)$ is assumed to be one. If τ is a constant, then $P(t)$ is simply a Poisson distribution and the mean of which is just τ, a constant scattering mean free time. Unfortunately, τ is a complicated function of the crystal momenta and is usually simplified to be a function of the energy which implies the assumption of isotropic scattering.

What is required in a Monte Carlo simulation is a means to determine the time interval T in which the electron drifts freely, and is scattered at the end of the interval. From Equation A1.2, and knowing that the probability per unit time of having one scattering event at $t=t_1$ is just the scattering rate at $t=t_1$, the distribution for T can be expressed as

$$P_{sc}(T) = P(t)\, \frac{1}{\tau(T)} = \frac{1}{\tau(T)}\, \exp\left[-\int_0^T \frac{dt'}{\tau(t')}\right]. \qquad\qquad (A1.3)$$

By generating a random number r uniformly distributed between 0 and 1, T can be obtained by solving

$$r = \int_0^T P_{sc}(t)\, dt$$

$$= \int_0^T \frac{1}{\tau(t)} \exp\left[-\int_0^t \frac{dt'}{\tau(t')} \right] dt$$

$$= -\int_0^T d\left\{ \exp\left[-\int_0^t \frac{dt'}{\tau(t')} \right] \right\}$$

$$= 1 - \exp\left[-\int_0^T \frac{dt}{\tau(t)} \right] . \tag{A1.4}$$

Since there is no difference in probability for r or (1-r) to occur, Equation (A1.4) is sometimes written as

$$r = \exp\left[-\int_0^T \frac{dt}{\tau(t)} \right] . \tag{A1.5}$$

As mentioned earlier, $\tau(E(\vec{k}(t)))$ is a complicated function, and its dependence on time is through the wave vector, the equation of motion, and hence the band structure. There is no simple way of solving Equation A1.5. One has to invent some mathematical device to solve the equation or to find a way to get around it. We describe two methods which have been commonly used to solve this problem.

As discussed in Reference 16, one can adopt a pseudo scattering mechanism to simplify Equation A1.5. This is commonly called a self-scattering method. It is a mathematical device without physical sig-nificance and the idea of which is summarized as follows.

One includes in the simulation an extra scattering mechanism of the form

$$S_{ps}(\vec{k},\vec{k}') = \frac{1}{\tau_{ps}(E(\vec{k}))} \, S(\vec{k} - \vec{k}') \, ,\qquad (A1.6)$$

where $S_{ps}(\vec{k},\vec{k}')$ is the transition probability from state $\vec{k}$ to $\vec{k}'$, and $1/\tau_{ps}(E(\vec{k}))$ is the scattering rate for the mechanism. Because the δ-function conserves the wave vector of the carrier, i.e., the carrier is exchanged by itself, one sees that this mechanism is physically insignificant. If the scattering strength is chosen as

$$\frac{1}{\tau_T} = \frac{1}{\tau(E)} + \frac{1}{\tau_{ps}(E)} \, ,\qquad (A1.7)$$

where $1/\tau_T$ is a constant and is now the total scattering rate, one sees that Equation A1.5 can be easily solved as

$$r = \exp\left[-\int_0^T \left(\frac{1}{\tau_{ps}(t)} + \frac{1}{\tau(t)}\right) dt\right]$$

$$= \exp\left[-\int_0^T \frac{1}{\tau_T} dt\right]$$

$$= \exp\left[-\frac{T}{\tau_T}\right] \, .\qquad (A1.8)$$

Thus, the free flight time is simply expressed as

$$T = \tau_T \ln \frac{1}{r} \ . \tag{A1.9}$$

In an actual simulation, when self-scattering occurs, one simply lets the carrier continue in its present momentum state. The only draw-back with the self-scattering scheme is that the total constant scattering rate has to be greater than the maximum true scattering rate in order to make the self-scattering rate always positive. Thus, the self-scattering rate, which is complementary to the true total scattering rate, is ex-tremely high at low energies. This makes the simulation inefficient be-cause most of the CPU time is spent on counting self-scattering events which have no physical significance. In order to improve the efficiency of the simulation, one can divide the energy space into regions and assign different values of τ_T to different regions to optimize the simulation. But when carriers propagate from one region to the other, one again deals with complicated mathematics which is simply not practical if a realistic band structure is considered. If one considers a simple parabolic band, this may be a way to go. The details for the discussion can be found in [17] and are omitted here.

The second method described below was what has been used in our Monte Carlo simulation. The central idea is to bypass completely the complicated integral form of Equation A1.4 and go back to its differential form.

As discussed at the beginning of the appendix, the probability of a carrier being scattered in the short interval $t_1 < t < t_1 + \Delta t$ can be written as

$$P_{sc}(t_1; \Delta t) \simeq \frac{\Delta t}{\tau(t_1)} \ . \tag{A1.10}$$

This holds true as long as Δt is short enough that $\tau(t)$ remains almost a constant in the interval. In the simulation, if we let the carrier drift during a small increment of time such that Equation A1.10 holds true, then random numbers can be generated to determine whether the carrier is to be scattered in the next time increment.

The actual Monte Carlo procedure is described as follows. We first find the total scattering rate corresponding to the present state of the carrier. We then let it drift freely for one tenth of the mean free scattering time, which is the reciprocal of the total scattering rate. A random number r, uniformly distributed between 0 and 1, is generated to represent the probability of scattering occurring in the next time increment Δt. If the generated random number r satisfies the relation

$$r \leq \frac{\Delta t}{\tau(t)} , \tag{A1.11}$$

the carrier is scattered. This process is conceptually simple and is exact if Δt is an infinitesimal increment. In a practical simulation, one can not afford to use too small a time increment because it makes the program extremely slow. As long as Δt is chosen to be about one tenth the mean free scattering time, one finds that both the speed of the program and the accuracy of the calculation are acceptable. So, in our simulation, Δt is always chosen to be about one tenth of the mean free scattering time corresponding to the present state of the carrier.

APPENDIX 2

SUMMARY OF SCATTERING MECHANISMS IN SILICON

In this appendix, we summarize the different scattering mechanisms that have been included in our Monte Carlo model for silicon. As discussed in Section 2.2, the low energy scattering rates are calculated by the conventional method: the Golden rule, the Born approximation and the effective mass density-of-states.

The analytic band structure for low energy near the band edge of an electron in the state $\vec{k}$ in the ith valley is given by

$$\gamma(E^{(i)}(\vec{k})) = \frac{\hbar^2}{2} \left[\frac{(\vec{k}-\vec{k}_0^{(i)})^2_l}{m_l} + \frac{(\vec{k}-\vec{k}_0^{(i)})^2_t}{m_t} \right] \tag{A2.1}$$

and

$$\gamma(E) = E(1+\alpha E) \tag{A2.2}$$

where α is the nonparabolicity factor; $\vec{k}_0^{(i)}$ is the wave vector of the minimum of the ith valley; the subscripts l and t stand for longitudinal and transverse components with respect to the symmetry axis of the valley; m_l and m_t are the longitudinal and transverse effective masses of the electrons. The density-of-states effective mass corresponding to the elliptic energy surface is given by

$$m_D = (m_l m_t^2)^{1/3} .$$
(A2.3)

In all calculations, the overlap integrals are assumed to be one and the squared matrix elements are always expressed in terms of the assumed constant deformation potentials. The values of the deformation potential constants are determined mainly through fits to experimental transport data, for example, drift velocities, impact ionization coefficients, etc. We follow closely the work of Canali et al. [18] and the material parameters are listed in Appendix 3.

2.1   Intravalley acoustic scattering

As discussed in [18], the angular dependence of the matrix element for acoustic phonon scattering can be averaged into the squared matrix element given by [24]

$$|H'|^2 = \frac{E_1^2 \hbar q}{2 V \rho v_s} \left\{ \begin{array}{c} N_q \\ \\ N_q + 1 \end{array} \right\} ,$$
(A2.4)

where E_1 is the deformation-potential constant, V and ρ are the volume and the density of the semiconductor, v_s is the velocity of sound, and N_q is the phonon distribution; N_q or N_q+1 must be taken for absorption or emission, respectively. By application of the Golden rule, the matrix element in Equation A2.4 yields the scattering rate

$$P_{ac}(q)d^3q = -\frac{E_1^2 q}{8\pi^2 \rho v_s} \left\{ \begin{array}{c} N_q \\ \\ N_q + 1 \end{array} \right\} \cdot \delta(E(\vec{k+q}) - E(\vec{k}) \mp \hbar q v_s)d^3q \ , \qquad (A2.5)$$

where the upper or lower sign must be taken for absorption or emission, respectively. In order to simplify the mathematics, the nonparabolicity factor α is put to zero for acoustic scattering. So by performing the Herring and Vogt [104] transformation with $\alpha=0$, Equation A2.1 becomes

$$E^{(i)} = \frac{\hbar^2 k^{*2(i)}}{2m_0} \qquad (A2.6)$$

where $\vec{k}^{*(i)}$ is the transformed wave vector of $\vec{k}-\vec{k}_0^{(i)}$ in the ith valley, and m_0 is the free mass of the electrons. Transforming to the starred space, one again approximates

$$q = q^* \left[\frac{m_1}{m_0} \cos^2\theta^* + \frac{m_t}{m_0} \sin^2\theta^* \right]^{1/2} \cong q^* \left[\frac{m_D}{m_0} \right]^{1/2} \ , \qquad (A2.7)$$

where θ^* is the angle between $\vec{q}^*$ and the principal axis of the valley, and m_D the density of states effective mass. The argument of the energy conservation δ-function then becomes

$$\frac{\hbar^2 q^{*2}}{2m_0} \pm \frac{\hbar^2}{m_0} k^* q^* \cos\gamma \mp \hbar q^* \left(\frac{m_D}{m_0} \right)^{1/2} v_s \ , \qquad (A2.8)$$

where γ is the angle between $\vec{q}^{\,*}$ and $\vec{k}^{\,*}$. As in the standard procedure [24], Equation A2.7 is put to zero and the condition $|\cos\gamma| < 1$ yields the limits for $\vec{q}^{\,*}$. It is more convenient to express these limits by a dimensionless variable

$$x = \frac{\hbar q v_s}{kT} = \left(\frac{\hbar q^* v_s}{kT}\right) \left(\frac{m_D}{m_0}\right)^{1/2} . \tag{A2.9}$$

These limits are given in Table A2.1 for different cases, where $E^* = \frac{1}{2} m_D v_s^2$. The transition rate is given by

$$P_{ac}(x)d^3x = \frac{A_a}{E^{1/2}} \left\{ \begin{array}{c} N_q(x) \\ \\ N_q(x) + 1 \end{array} \right\} x^2 dx = f(x)dx , \tag{A2.10}$$

where

$$A_a = \left(\frac{E_1 m_D}{4\hbar^2}\right)^2 \left(\frac{1}{\pi \rho v_s}\right) \left(\frac{kT}{E_s^{*1/2}}\right)^3 . \tag{A2.11}$$

At this point, one must introduce an expression for $N_q(x)$. A suitable approximation is given by the following truncated Laurent expansion [18]:

$$N_q(x) = \frac{1}{e^x - 1} \cong \left\{ \begin{array}{ll} \frac{1}{x} - \frac{1}{2} + \frac{1}{12} x - \frac{1}{720} x^3, & x < 3.5 \\ \\ 0 & , \quad x \geq 3.5 . \end{array} \right. \tag{A2.12}$$

Table A2.1 [18]:

Integration limits for Equation A2.9

with $x = \hbar q V_s / kT$.

$E \leqslant E_s^{*}$	Absorption	$\begin{cases} x_1 = \dfrac{4E_s^{*1/2}}{kT} \, (E_s^{*1/2} - E^{1/2}) \\[3ex] x_2 = \dfrac{4E_s^{*1/2}}{kT} \, (E_s^{*1/2} + E^{1/2}) \end{cases}$
	No emission	
$E > E_s^{*}$	Absorption	$\begin{cases} x_1 = 0 \\[3ex] x_2 = \dfrac{4E_s^{*1/2}}{kT} \, (E^{1/2} + E_s^{*1/2}) \end{cases}$
	Emission	$\begin{cases} x_1 = 0 \\[3ex] x_2 = \dfrac{4E_s^{*1/2}}{kT} \, (E^{1/2} - E_s^{*1/2}) \end{cases}$

The integration of the scattering rate in Equation A2.9 can then be performed very easily as

$$\frac{1}{\tau_{ac}} = \int_{x_1}^{x_2} f(x)dx \; , \tag{A2.13}$$

where x_1 and x_2 are listed in Table A2.1. The resulting scattering rates are given in Table A2.2 and plotted in Figure A2.1.

For room temperature, $E_s^* = 7.46 \times 10^{-5}$ eV and $\bar{x}$ corresponds to an energy of about 7 eV. The cases for $x_2 > \bar{x}$ and $E < E_s^*$ are never really used in actual calculations. For lower temperatures, all cases have to be considered.

The energy exchanged in the acoustic scattering depends on the momentum exchanged during the process. To keep track of both energy and momentum exchanged in the process requires an analytic form of the band structure. To simplify the situation, we consider an average phonon energy as the energy exchanged during the acoustic scattering processes. The average phonon energy, which is a function of the electron energy, is obtained from the distribution $f(x)$ of the phonon momentum $x = \hbar q v_s / kT$ given in Equation A2.9. For a given electron energy $x_2(E)$ (see Table A2.1), the corresponding average phonon energy can be obtained as

$$\langle x \rangle = \frac{\int_{x_1}^{x_2} xf(x)dx}{\int_{x_1}^{x_2} f(x)dx} \tag{A2.14}$$

Table A2.2 [18]:

Acoustic scattering rates.

$\bar{x}$ is taken as 3.5 according to Equation A2.11.

$E \leqslant E_s^*$

Absorption
No emission

$$\frac{1}{\tau_{ac}} = (A_a/E^{1/2})[\frac{1}{2}(x_2^2-x_1^2) - \frac{1}{6}(x_2^3-x_1^3) + \frac{1}{48}(x_2^4-x_1^4) - \frac{1}{4320}(x_2^6-x_1^6)]$$

Absorption

$$\frac{1}{\tau_{ac}} = \frac{A_a}{E^{1/2}}(\frac{1}{2}x_2^2 - \frac{1}{6}x_2^3 + \frac{1}{48}x_2^4 - \frac{1}{4320}x_2^6), \quad x_2 < \bar{x}$$

$$\frac{1}{\tau_{ac}} = \frac{A_a}{E^{1/2}}(\frac{1}{2}\bar{x}^2 - \frac{1}{6}\bar{x}^3 + \frac{1}{48}\bar{x}^4 - \frac{1}{4320}\bar{x}^6), \quad x_2 \geqslant \bar{x}$$

$E > E_s^*$

Emission

$$\frac{1}{\tau_{ac}} = \frac{A_a}{E^{1/2}}(\frac{1}{2}x_2^2 + \frac{1}{6}x_2^3 + \frac{1}{48}x_2^4 - \frac{1}{4320}x_2^6), \quad x_2 < \bar{x}$$

$$\frac{1}{\tau_{ac}} = \frac{A_a}{E^{1/2}}(\frac{1}{2}\bar{x}^2 - \frac{1}{6}\bar{x}^3 + \frac{1}{48}\bar{x}^4 - \frac{1}{4320}\bar{x}^6 + \frac{1}{3}x_2^3), \quad x_2 \geqslant \bar{x}$$

Figure A2.1: Acoustic phonon scattering rate as a function of the electron energy.

or

$$\langle h\omega_q \rangle = kT\langle x \rangle \; . \qquad\qquad (A2.15)$$

We plot in Figure A2.2 the average phonon energies for both emission and absorption at room temperature. Notice that at high electron energies, the energies exchanged in the scattering process are not negligible which makes the usual assumption of equipartition questionable.

2.2 Intervalley scattering

The scattering mechanism is treated here in the traditional way [24]. For equivalent intervalley scattering, the total scattering rate is given by

$$\frac{1}{\tau_{iv}} = A_{iv}\, \gamma^{1/2}\; (E')(1+2\alpha E') \begin{cases} N_i & (\text{absorption}) \\ \\ N_i+1 & (\text{emission}) \end{cases} \qquad (A2.16)$$

where

$$A_{iv} = D_i^2 m_D^{3/2} Z_i \Big/ \sqrt{2}\pi\, \rho\, \hbar\, \omega_i \; ;$$

$$E' = \begin{cases} E(\vec{k}) + \hbar\omega_i & (\text{absorption}) \\ \\ E(\vec{k}) - \hbar\omega_i & (\text{emission}) \end{cases} \; ;$$
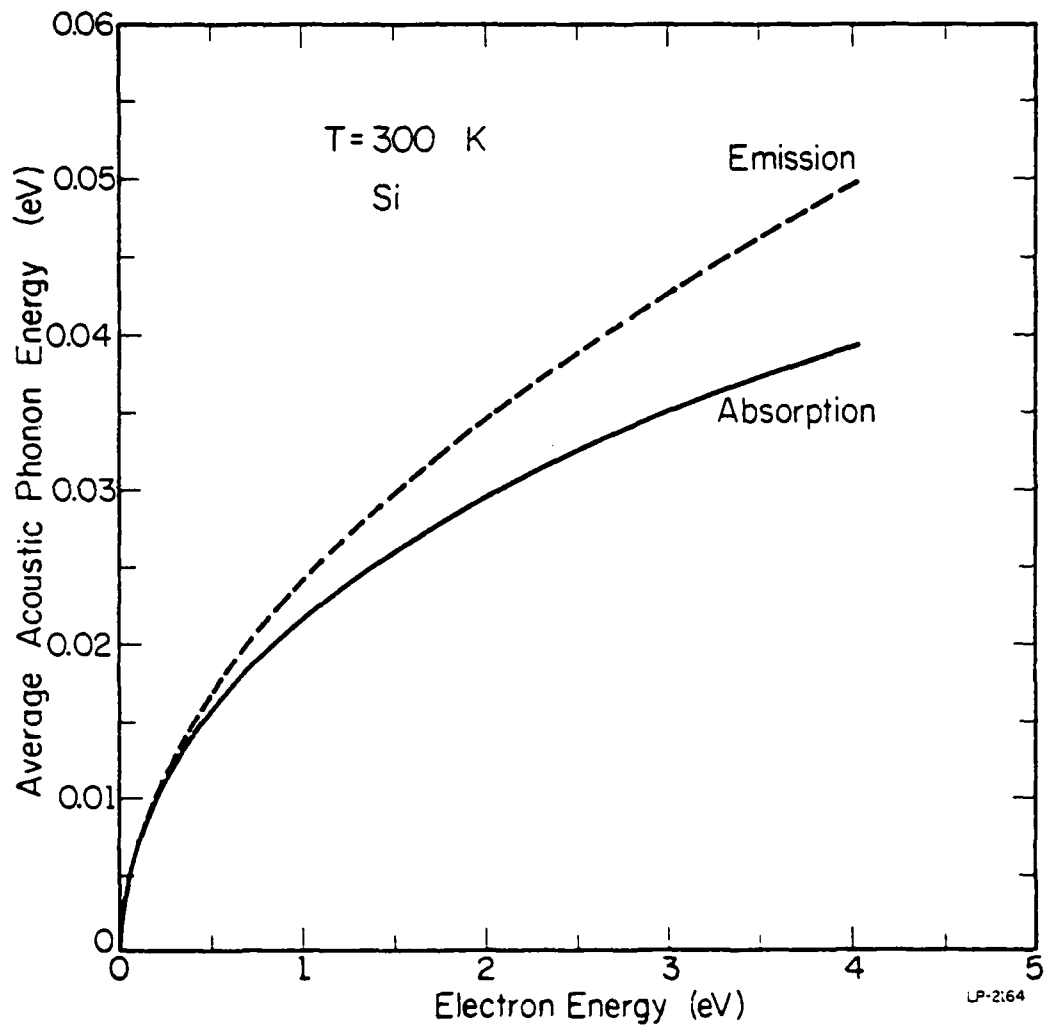
Figure A2.2:   The average acoustic phonon energy as a function
              of the electron energy for both emission and
              absorption.

D_i and ω_i are the coupling constant and the phonon energy (assumed constant) of the considered ith mechanism; Z_i is the number of possible final valleys. For nonequivalent intervalley scattering, it is essentially given by the same formula except that E' is referred to the proper valley minima. Details of the formula can be found in appendix of Reference 25 and is hence omitted here.

The scattering rates for f and g scatterings are plotted in Figure A2.3 respectively.
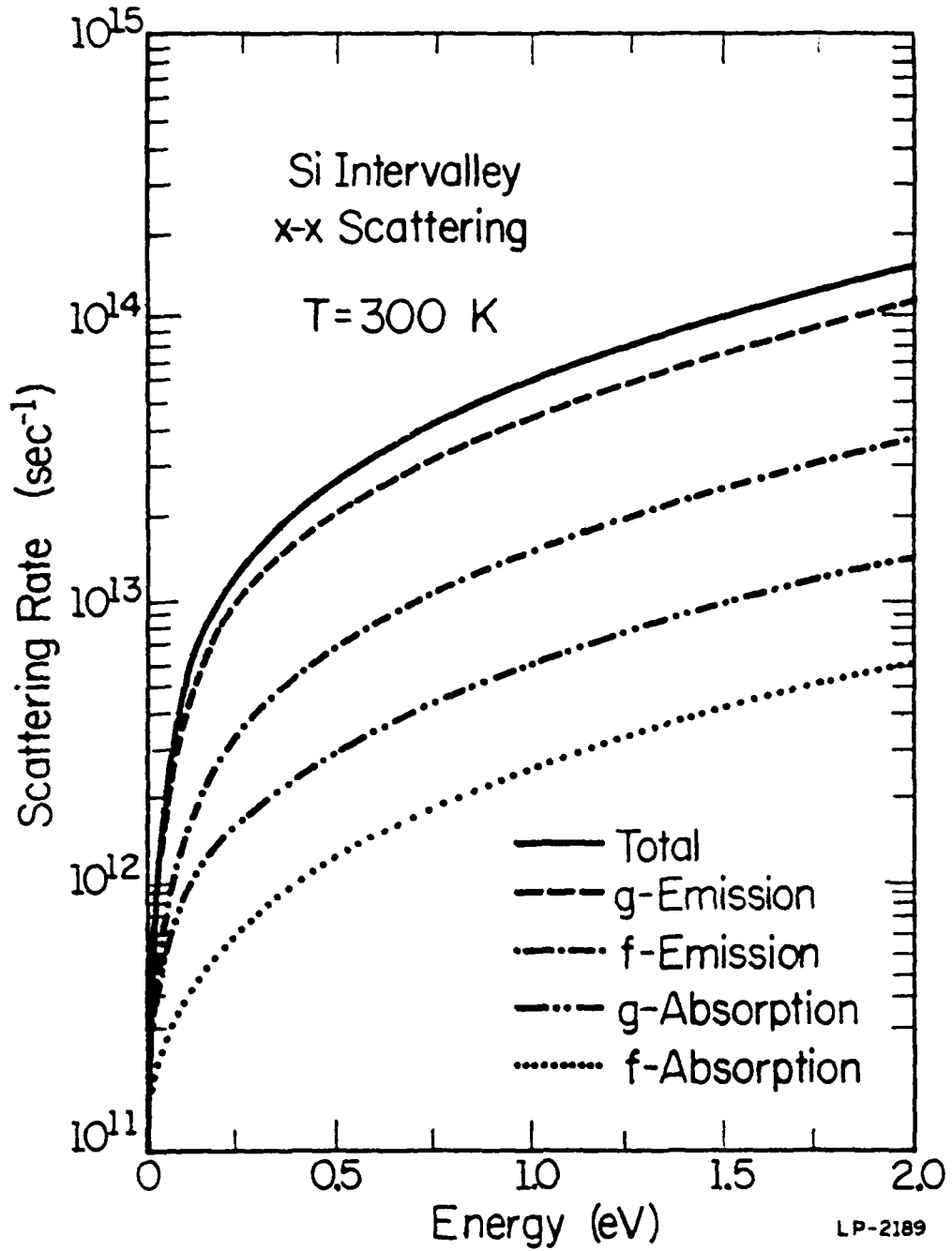
Figure A2.3: Intervalley scattering rates in silicon.

APPENDIX 3

MATERIAL PARAMETERS FOR SILICON

Bulk Material Parameters

Lattice constant	5.43	$\overset{\circ}{A}$
Density	2.329	g/cm^3
Dielectric constant	11.7	
Sound velocity	9.04×10^5	cm/s

X-Valley

Effective masses

transverse	0.19	m_0
longitudinal	0.916	m_0
Nonparabolicity	0.5	eV^{-1}
Acoustic deformation potential	9.5	eV

L-Valley

Effective masses

transverse	0.12	m_0
longitudinal	1.59	m_0

X-X Intervalley Scattering

Phonon temperature(K)	Deformation potential(eV/cm)	Scattering type
220	3×10^7	f
550	2×10^8	f
685	2×10^8	f
140	5×10^7	g
215	8×10^7	g
720	1.1×10^9	g

X-L Intervalley Scattering

Phonon temperature(K)	Deformation potential(eV/cm)
672	2×10^8
634	2×10^8
480	2×10^8
197	2×10^8

REFERENCES

[1] K. Hess, H. Morkoc, H. Shichijo and B. G. Streetman, "Negative differential resistance through real-space electron transfer," Appl. Phys. Lett., vol. 35, pp. 467-471, 1979.

[2] H. Shichijo, K. Hess and B. G. Streetman, "Real space electron transfer by thermionic emission in GaAs-Al$_x$Ga$_{1-x}$As heterostructures," Solid-State Electron., vol. 23, pp. 817-822, 1980.

[3] K. Hess, "Phenomenological physics of hot carriers in semiconductors," Physics of Nonlinear Transport in Semiconductors, edited by D. K. Ferry, J. R. Barker, and C. Jacoboni, 1979.

[4] R. Chin, N. Holonyak, Jr., G. E. Stillman, J. Y. Tang, and K. Hess, "Impact ionization in multilayered heterojunction structures," Electron. Lett., vol. 16, pp. 467-469, 1980.

[5] J. Y. Tang and K. Hess, "Real space transfer noise in buried-channel devices," IEEE Trans. Electron. Devices, vol. ED-28, no. 3, pp. 285-289, 1981.

[6] T. H. Ning, "Hot-electron emission from silicon into silicon dioxide," Solid-State Electron., vol. 21, pp. 273-282, 1978.

[7] R. J. McIntyre, "Mutiplication noise in uniform avalanche diodes," IEEE Trans. Electron. Dev., vol. ED-13, pp. 164-167, 1966.

[8] G. E. Stillman and C. M. Wolfe, "Avalanche photodiodes," Semiconductors and Semimetals, Academic Press, N.Y., pp. 291-393, 1977.

[9] F. Capasso, W. T. Tsang, A. L. Hutchinson, and G. F. Williams, "Enhancement of electron impact ionization in a superlattice: a new avalanche photodiode with a large ionization rate ratio," IEDM Technical Digest, New York, IEEE, 1981.

[10] D. K. Ferry, "Modeling of carrier transport in the finite collision duration regime: Effects in submicron semiconductor devices," Physics of Nonlinear Transport in Semiconductors, edited by D. K. Ferry, J. R. Barker and C. Jacoboni, Pergamon Press, 1979.

[11] J. R. Barker, "Quantum transport theory," Physics of Nonlinear Transport in Semiconductors, edited by D. K. Ferry, J. R. Barker, and C. Jacoboni, 1979.

[12] H. Shichijo and K. Hess, "Band-structure dependent transport and impact ionization in GaAs," Phys. Rev. B, vol. 23, pp. 4197-4207, 1981.

[13] J. Y. Tang, H. Shichijo, K. Hess, and G. J. Iafrate, "Band-structure dependent impact ionization in silicon and gallium arsenide," Proceedings of the 3rd International Conferences on Hot Carriers in Semiconductors, Montpellier, France, 1981.

[14] K. Binder, Monte Carlo Methods in Statistical Physics, Springer-Verlag, Berlin, 1979.

[15] T. Kurosawa, Proc. Internat. Conf. Phys. Semicond., Kyoto; J. Phys. Soc. Japan., Suppl. 21, p. 424, 1966.

[16] W. Fawcett, A. D. Boardman, and S. Swain, "Monte Carlo determination of electron transport properties in GaAs," J. Phys. Chem. Solids, vol. 31, pp. 1963-1990, 1970.

[17] V. Borsari and C. Jacoboni, "Monte Carlo calculations on electron transport in CdTe," Phys. Stat. Sol. (b), vol. 54, pp. 649-661, 1972.

[18] C. Canali, C. Jacoboni, F. Nava, G. Ottaviani, and A. Alberigi-Quaranta, "Electron drift velocity in silicon," Phys. Rev. B., vol. 12, pp. 2265-2284, 1975.

[19] G. Ottaviani, L. Reggiani, C. Canali, F. Nava, and A. Alberigi-Quaranta, "Hole drift velocity in Silicon," Phys. Rev. B, vol. 12, pp. 3318-3329, 1975.

[20] G. Baccarani, C. Jacoboni, and A. M. Mazzone, "Current transport in narrow-base transistors," Solid-State Electron., vol. 20, pp. 5-10, 1977.

[21] J. Zimmermann, Y. Leroy, and E. Constant, "Monte Carlo calculation of microwave and far-infrared hot-carrier mobility in n-Si: Efficiency of millimeter transit-time oscillators," J. Appl. Phys., vol. 49, pp. 3378-3383, 1978.

[22] J. Zimmermann and E. Constant, "Application of Monte Carlo technique to hot carrier diffusion noise calculation in unipolar semiconducting components," Solid-State Electron., vol. 23, pp. 915-925, 1980.

[23] P. Nougier, J. C. Vaissiere, D. Gasquet, J. Zimmermann and E. Constant; "Determination of transient regime of hot carriers in semiconductors using the relaxation time approximations," J. Appl. Phys., vol. 52, pp. 825-832, 1981.

[24] E. M. Conwell, "High field transport in semiconductors," Solid State Physics, Suppl. 9, 1967.

[25] H. Shichijo, "Theoretical studies of high field transport in III-V semiconductors," Thesis, Univ. of Ill., 1980.

[26] P. J. Price, "Monte Carlo calculation of electron transport in solids," Semiconductor and Semimetals, vol. 14, Chapter 4, 1979.

[27] A. D. Boardman, "Computer simulations of hot electron behaviors in semiconductors using Monte Carlo Method," Physics Program, Chapter 11, John Wiley and Sons, Ltd., 1980.

[28] P. Chatterjee, "Physics and modeling of active and passive devices associated with current VLSI structures," Proceedings of the 3rd workshop on the physics of submicron structures, edited by D. K. Ferry, H. Grubin, K. Hess, and G. J. Iafrate, Plenum press, 1982.

[29] J. G. Ruch, "Electron dynamics in short channel field-effect transistors," IEEE Trans. Electron. Dev., vol. Ed-19, pp. 652-654, 1972.

[30] T. J. Maloney and J. Frey, "Transient and steady-state electron transport properties of GaAs and InP," J. Appl. Phys., vol. 48, pp. 781, 1977.

[31] M. S. Shur, "Ballistic transport in a semiconductor with collisions," IEEE Trans. Electron Devices, vol. Ed-28, pp. 1120-1130, 1981.

[32] M. S. Shur and L. F. Eastman, "Near ballistic electron transport in GaAs devices at 77°K," Solid-State Electron., vol. 24, pp. 11-18, 1981.

[33] L. F. Eastman, "Experimental studies of ballistic transport in semiconductors," Proceedings of the 3rd International Conference on Hot Carriers in Semiconductors, Montpellier, France, 1981.

[34] K. Hess, "Ballistic electron transport in semiconductors," IEEE Trans. Electron Devices, vol. Ed-28, pp. 937-940, 1981.

[35] J. R. Barker, "High field collision rates in polar semiconductors," Solid-State Electronics, vol. 21, pp. 267-271, 1978.

[36] M. A. Littlejohn, J. R. Hauser, and T. H. Glisson, "Velocity-field characteristics of GaAs with $\Gamma_6^c-L_6^c-X_6^c$ conduction band ordering," J. Appl. Phys., vol. 48, pp. 4587-4590, 1977.

[37] M. L. Cohen and T. K. Bergstresser, "Band structures and pseudopotential form factors for fourteen semiconductors of the diamond and zinc-blende structures," Phys. Rev., vol. 141, pp. 789-796, 1966.

[38] T. J. Maloney, "Polar mode scattering in ballistic transport GaAs devices," IEEE Electron Device Letters, vol. EDL-1, p. 54.

[39] J. P. Nougier, "Noise and diffusion of hot carriers," in Physics Nonlinear Transport, edited by D. K. Ferry, J. R. Barker, and C. Jacoboni, Plenum Press, p. 425, 1979.

[40] C. Y. Duh and J. L. Moll, "Temperature dependence of hot electron drift velocity in silicon at high electric field," Solid-State Electronics, vol. 11, pp. 917-932, 1968.

[41] K. Hess and C. T. Sah, "Warm and hot carriers in silicon surface-inversion layers," Phys. Rev. B, vol. 10, pp. 3375-3386, 1974.

[42] C. Jacoboni, C. Canali, G. Ottaviani, and A. Alberigi Quaranta, "A review of some charge transport properties of silicon," Solid-State Electron., vol. 20, pp. 77-89, 1976.

[43] K. Hess, "Review of experimental aspects of hot electron transport in MOS structures," Solid-State Electron., vol. 21, pp. 123-132, 1978.

[44] M. H. Jorgensen, "Electron-phonon scattering and high-field transport in n-type Si," Phys. Rev. B, vol. 18, pp. 5657-5666, 1978.

[45] M. Asche and O. G. Sarbei, "Electron-phonon interaction in n-Si," Phys. Stat. Sol. (6), vol. 103, pp. 11-50, 1981.

[46] B. N. Brockhouse and P. K. Iyengar, "Normal modes of Ge by neutron spectrometry," Phys. Rev., vol. 111, pp. 747-754, 1958.

[47] B. N. Brockhouse, "Lattice vibrations in silicon and germanium," Phys. Rev. Lett., vol. 2, pp. 256-258, 1959.

[48] D. Long, "Scattering of Conduction electrons by lattice vibrations in silicon," Phys. Rev., vol. 120, pp. 2024-2032, 1960.

[49] P. A. Wolff, "Theory of electron multiplication in silicon and germanium," Phys. Rev., vol. 95, pp. 1415-1420, 1954.

[50] W. Shockley, "Problems related to p-n junctions in silicon," Solid-State Electron., vol. 2, pp. 35-67, 1961.

[51] G. A. Baraff, "Distribution functions and ionization rates for hot electrons in semiconductors," Phys. Rev., vol. 128, pp. 2507-2517, 1962.

[52] L. V. Keldysh, "Concerning the theory of impact ionization in semiconductors," Sov. Phys. JETP, vol. 21, pp. 1135-1144, 1965.

[53] W. P. Dumke, "Theory of avalanche breakdown in InSb and InAs," Phys. Rev., vol. 167, pp. 783-789, 1968.

[54] R. Chwang, C. W. Kao and C. R. Crowell, "Normalized theory of impact ionization and velocity saturation in nonpolar semiconductors via a Markov chain approach," Solid-State Electron., vol. 22, pp. 599-620, 1979.

[55] E. O. Kane, "Electron scattering by pair production in silicon," Phys. Rev., vol. 159, pp. 624-631, 1967.

[56] S. M. Sze, Physics of Semiconductor Devices, John Wiley and Sons, New York, 1969.

[57] P. M. Smith, M. Inoue, and J. Frey, "Electron velocity in Si and GaAs at very high electric fields," Appl. Phys. Lett., vol. 37, pp. 797-798, 1980.

[58] C. A. Lee, R. A. Logan, R. L. Batdorf, J. J. Kleimack, and W. Wiegmann, "Ionization rates of holes and elec-rons in silicon," Phys. Rev., vol. 134, pp. A761-773, 1964.

[59] C. R. Crowell, and S. M. Sze, "Temperature dependence of avalanche multiplication in semiconductors," Appl. Phys. Lett., vol. 9, pp. 242-244, 1966.

[60] R. Van Overstraeten and H. De Man, "Measurement of the ionization rates in diffused silicon p-n junctions," Solid-State Electron., vol. 13, pp. 583-608, 1970.

[61] K. Hess, J. Y. Tang, K. Brennan, H. Shichijo, and G. Stillman, "Reply to Comment on 'Simulation of high-field transport in GaAs using a Monte Carlo and pseudopotential band structures' and on 'Band-structure dependent transport and impact ionization in GaAs'," J. Appl. Phys., vol. 53, pp. 3327-3329, 1981.

[62] C. Jacoboni, R. Minder, and G. Majni, "Effects of band non-parabolicity on electron drift velocity in silicon above room temperature," J. Phys. Chem. Solids, vol. 39, pp. 1129-1133, 1975.

[63] J. F. Schneck, in Sixth Annual Reliability Symposium Proceedings, p. 31, IEEE, New York, 1968.

[64] B. A. McDonald, "Avalanche degradation of h_{FE}," IEEE Trans. Electron Devices, ED-17, pp. 871-878, 1970.

[65] J. F. Verwey, "The introduction of charge in SiO_2 and the increase of emitter-base junction of gated transistors," Appl. Phys. Lett., vol. 15, pp. 270-272, 1969.

[66] J. J. Chang, "Nonvolatile semiconductor memory devices," Proceedings of the IEEE, vol. 64, pp. 1039-1059, 1976.

[67] E. H. Nicollian and C. N. Berglund, "Avalanche injection of electrons into insulating SiO_2 using MOS structures," J. Appl. Phys., vol. 41, pp. 3052-3057, 1970.

[68] J. F. Verwey, "Nonavalanche injection of hot carriers into SiO_2," J. Appl. Phys., vol. 44, pp. 2681-2687, 1973.

[69] T. H. Ning and H. N. Yu, "Optically induced injection of hot electrons into SiO_2," J. Appl. Phys., vol. 45, pp. 5373-5378, 1974.

[70] C. Bulucea, "Avalanche injection into the oxide in silicon gate-controlled devices-I. Theory," Solid-State Electron., vol. 18, pp. 363-374, 1975.

[71] C. Bulucea, "Avalanche injection into the oxide in silicon gate-controlled devices-II. Experimental results," Solid-State Electron., vol. 18, pp. 381-391, 1975.

[72] D. R. Young, "Electron current injected into SiO_2 from p-type Si depletion regions," J. Appl. Phys., vol. 47, pp. 2098-2102, 1976.

[73] T. H. Ning, C. M. Osburn, and H. N. Yu, "Emission probability of hot electrons from silicon into silicon dioxide," J. Appl. Phys., vol. 48, pp. 286-293, 1976.

[74] T. H. Ning, "Hot-electron emission from silicon into silicon dioxide," Solid-State Electron., vol. 21, pp. 273-282, 1978.

[75] R. R. Troutman, "Silicon surface emission of hot electrons," Solid-State Electron., vol. 21, pp. 283-289, 1978.

[76] B. E. Deal, E. H. Snow, and C. A. Mead, "Barrier energies in metal-silicon dioxide-silicon structures," J. Phys. Chem. Solids, vol. 27, pp. 1873-1879, 1966.

[77] Reference 56, p. 163.

[78] W. Kohn and J. M. Luttinger, "Quantum theory of electrical transport phenomena. I." Phys. Rev., vol. 108, pp. 590-611, 1957.

[79] W. Kohn and J. M. Luttinger, "Quantum theory of electrical transport phenomena. II," Phys. Rev., vol. 109, pp. 1892-1909, 1958.

[80] R. Kubo, "Statistical-mechanical theory of irreversible processes. I. General theory and simple applications to magnetic and conduction problems," J. Phys. Soc. Jpn., vol. 12, pp. 570-586, 1957.

[81] M. Dresden, "Recent developments in the quantum theory of transport and galvanomagnetic phenomena," Rev. Mod. Phys., vol. 33, pp. 265-342, 1961.

[82] G. V. Chester, "The theory of irreversible processes," Rept. Prog. Phys., vol. 26, pp. 411-472, 1963.

[83] R. Kubo, "The fluctuation-dissipation theorem," Rept. Prog. Phys., vol. 29, pp. 255-284, 1966.

[84] J. M. Luttinger, "Mathematical methods in solid state and superfluid physics," Oliver and Boyd, New York, 1968.

[85] C. H. Scott and E. J. Moore, "Quasiparticles for the quantum electron-impurity transport problem," Physica, vol. 62, pp. 312-320, 1972.

[86] J. R. Barker, "Quantum transport theory of high-field conduction in semiconductor," J. Phys. C, vol. 6, pp. 2663-2684, 1973.

[87] K. Hess, "Comment on 'Effect of collisional broadening on Monte Carlo simulation of high-field transport in semiconductor devices'," IEEE, vol. EDL-2, pp. 297-298, 1981.

[88] R. Peierls, "Some simple remarks on the basis of transport theory," Lecture Notes in Physics, No. 31, Transport Phenomena, 1974.

[89] R. W. Zwanzig, "Statistical mechanics of irreversibility," Lect. Theor. Phys., vol. 3, pp. 106-141, 1960.

[90] D. Pines, The Many-Body Problem, Frontiers in Physics, Lecture note series, Benjamin Cummings, 1962.

[91] A. B. Migdal, "Interaction between electrons and lattice vibrations in a normal metal," Sov. Phys. JETP, vol. 34, pp. 996-1001, 1958.

[92] W. Jones and N. H. March, Theoretical Solid-State Physics, p. 567, John Wiley and Sons, New York, 1973.

[93] Reference 92, p. 161.

[94] Reference 90, p. 41.

[95] H. W. Wyld, Mathematical Method for Physicist, The Benjamin Cumming Publishing company, New York, 1976.

[96] J. M. Ziman, Elements of Advanced Quantum Theory, p. 83, Cambridge Press, Cambridge, 1969.

[97] Reference 90, p. 89.

[98] A. Messiah, Quantum Mechanics, John Wiley and Sons, New York, 1958.

[99] Y. C. Chang, D. Z.-Y. Ting, J. Y. Tang, and K. Hess, "Monte Carlo simulation of impact ionization in GaAs including quantum effects," to be published.

[100] S. N. Shadbe and C. Yeh, "Ionization rate in $(Al_xGa_{1-x})As$," J. Appl. Phys., vol. 41, pp. 4743-4744, 1970.

[101] G. E. Stillman, C. M. Wolfe, J. A. Rossi, and A. G. Foyt, "Unequal electron and hole impact ionization coefficients in GaAs," Appl. Phys. Lett., vol. 24, pp. 471-474, 1974.

[102] H. D. Law and C. A. Lee, "Interband scattering effects on secondary ionization coefficients in GaAs," Solid-State Electron., vol. 21, pp. 331-340, 1978.

[103] T. P. Pearsall, F. Capasso, R. E. Nahory, M. A. Pollack, and J. R. Chelikowsky, "The band structure dependence of impact ionization by hot carriers in semiconductors: GaAs," Solid-State Electron., vol. 21, pp. 297-302, 1978.

[104] C. Herring and E. Vogt, "Transport and deformation-potential theory for many-valley semiconductors with anisotropic scattering," Phys. Rev., vol. 101, pp. 944-961, 1956.

VITA

Jeffrey Yuh-Fong Tang was born on May 26, 1955 in Taipei, Taiwan. He attended National Taiwan University where he graduated with a Bachelor of Science degree in Electrical Engineering in June, 1977. Since 1979 he has been attending the University of Illinois at Urbana-Champaign. He received a Master of Science degree in Electrical Engineering in 1980. Mr. Tang is a member of Phi Kappa Phi, the American Physical Society and the Institute of Electrical and Electronics Engineers.